



**HAL**  
open science

# Modeling and Stability Control of Power-Electronic-Dominated Power Systems

Ke Guo

► **To cite this version:**

Ke Guo. Modeling and Stability Control of Power-Electronic-Dominated Power Systems. Electric power. Université Grenoble Alpes [2020-..]; Nanyang Technological University (Singapour), 2022. English. NNT : 2022GRALT034 . tel-03772785

**HAL Id: tel-03772785**

**<https://theses.hal.science/tel-03772785v1>**

Submitted on 8 Sep 2022

**HAL** is a multi-disciplinary open access archive for the deposit and dissemination of scientific research documents, whether they are published or not. The documents may come from teaching and research institutions in France or abroad, or from public or private research centers.

L'archive ouverte pluridisciplinaire **HAL**, est destinée au dépôt et à la diffusion de documents scientifiques de niveau recherche, publiés ou non, émanant des établissements d'enseignement et de recherche français ou étrangers, des laboratoires publics ou privés.

## THÈSE

Pour obtenir le grade de

**DOCTEUR DE L'UNIVERSITE GRENOBLE ALPES**

**préparée dans le cadre d'une cotutelle entre  
l'Université Grenoble Alpes et Nanyang  
Technological University**

Spécialité : **GENIE ELECTRIQUE**

Arrêté ministériel : le 25 mai 2016

Présentée par

**Ke GUO**

Thèse dirigée par **David FREY**  
codirigée par **Yi TANG**

préparée au sein des **Laboratoire de Génie Electrique**

dans les **Écoles Doctorales Electronique, Electrotechnique,  
Automatique, Traitement du Signal (EEATS)**

# **Modélisation et Contrôle de la Stabilité des Réseaux Electriques Dominés par L'électronique de Puissance**

Thèse soutenue publiquement le **5 mai 2022**,  
devant le jury composé de :

**Professeur, Hua LI**

Singapour, Président

**Professeur, Johan DRIESEN**

Belgique, Rapporteur

**Professeur, Xin ZHANG**

Chine, Rapporteur

**Professeur Associe, Dinh Nguyen HUNG**

Singapour, Examineur

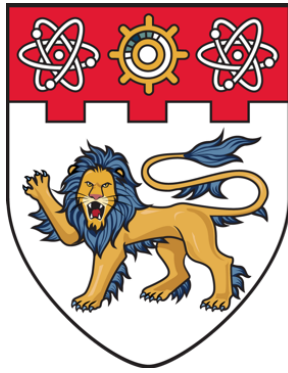
**Professeur Associe, Vincent DEBUSSCHERE**

France, Examineur

**Professeur, Bertrand RAISON**

France, Examineur





**NANYANG  
TECHNOLOGICAL  
UNIVERSITY**  

---

**SINGAPORE**

**MODELING AND STABILITY CONTROL OF POWER-  
ELECTRONIC-DOMINATED POWER SYSTEMS**

**GUO KE**

**Interdisciplinary Graduate School  
Energy Research Institute @ NTU**

**2022**





**MODELING AND STABILITY CONTROL OF POWER-  
ELECTRONIC-DOMINATED POWER SYSTEMS**

**GUO KE**

INTERDISCIPLINARY GRADUATE SCHOOL

A thesis submitted to the Nanyang Technological University  
in partial fulfilment of the requirement for the degree of  
Doctor of Philosophy

**2022**



## Statement of Originality

I hereby certify that the work embodied in this thesis is the result of original research, is free of plagiarised materials, and has not been submitted for a higher degree to any other University or Institution.

4 May 2022

.....

Date

*guoke.*

.....

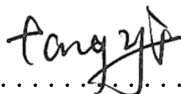
Guo Ke



## Supervisor Declaration Statement

I have reviewed the content and presentation style of this thesis and declare it is free of plagiarism and of sufficient grammatical clarity to be examined. To the best of my knowledge, the research and writing are those of the candidate except as acknowledged in the Author Attribution Statement. I confirm that the investigations were conducted in accord with the ethics policies and integrity standards of Nanyang Technological University and that the research data are presented honestly and without prejudice.

4 May 2022 .....  
Date

  
.....  
Tang Yi



## Authorship Attribution Statement

This thesis contains material from 2 papers published in the following peer-reviewed conference and journal where I was the first author.

Chapter 2 is published as K. Guo, J. Fang and Y. Tang, “Autonomous DC-Link Voltage Restoration for Grid-Connected Power Converters Providing Virtual Inertia”, IEEE Energy Conversion Congress and Exposition (ECCE), 2018, pp. 6387-6391.

The contributions of the co-authors are as follows:

I prepared and wrote the manuscript draft, derived the expressions, and explored the relationships between the cut-off frequency of the high-pass filter with the DC-link voltage restoration time and the inertia supportability.

Dr. J. Fang provided the initial idea, assisted me in establishing the hardware prototype and the experiment tests.

Prof. Y. Tang was responsible for revising and proofreading the manuscript.

Chapter 3 is published as K. Guo, Y. Qi, J. Yu, D. Frey, Y. Tang, “A Converter-Based Power System Stabilizer for Stability Enhancement of Droop-Controlled Islanded Microgrids”, *IEEE Transactions on Smart Grid* (DOI: 10.1109/TSG.2021.3096638).

The contributions of the co-authors are as follows:

I developed the control schemes of the converter-based power system stabilizer, performed modal analysis and case studies, prepared, and wrote the manuscript draft.

Dr. Y. Qi assisted me in establishing the hardware prototype, revising the original manuscript, and writing the response letter.

Mr. J. Yu assisted me in performing the hardware experimental test.

Prof. D. Frey and Prof. Y. Tang were responsible for revising and proofreading the manuscript.

4 May 2022

.....  
Date

*guoke.*

.....  
Guo Ke



---

## Abstract

Inspired by the target of carbon neutrality, an increasing number of renewable energies has been integrated into modern power systems. Due to the fluctuation and randomness of such renewable energies, power electronic converters are widely employed to interface power grids with renewable generators, such as solar photovoltaics (PV) panels and wind turbines, to produce stable and grid-compatible power outputs. Consequently, the traditional synchronous-generator-dominated power systems are evolving towards the power-electronic-dominated paradigms with a more complicated structure, thus giving rise to new instability problems. In light of this background, several critical stability issues are highlighted in this thesis, including the frequency stability associated with the lack of inertia, the power interaction stability of islanded microgrids, and the stability regarding constant power loads (CPLs) in power-electronic-dominated power systems. For power converters with a commonly used cascaded control architecture, the stability issues mentioned above are dominated by different control stages of power converters, with typical response times varying from seconds to dozens of milliseconds.

First, the frequency instability in power-electronic-dominated power systems is focused on. Opposite to conventional synchronous generators, which have rotating components with mechanical inertia to support frequency stability naturally, power electronic converters are strictly static with no rotating masses, leading to the lack of inertia in power-electronic-dominated power systems. To deal with the lack of inertia problem, a virtual inertia control scheme based on grid-connected converters (GCCs) has been presented in previous studies by utilizing the energy stored in DC-link capacitors to provide inertial support for power grids. However, due to the coupled relationship between grid frequency and DC-link voltage, the DC-link voltage cannot be restored automatically even after providing inertial support, thus deteriorating DC-link capacitors' lifetime and losing the capability to offer multiple inertial support during cascading frequency events. A high-pass filter is applied in this thesis to settle this issue, which extracts out only high-frequency components from the grid frequency for inertial emulation during frequency events. As a result, the DC-link

---

voltages of grid-connected converters can be restored autonomously after releasing inertial power during each frequency event and thus avoid the abnormal working conditions of power converters.

Second, the stability issue in droop-controlled islanded microgrids is highlighted. For islanded microgrids employing droop control to achieve power-sharing among multiple power generating units, a large droop gain benefits the accurate power-sharing at the expense of sacrificed power interaction dynamic stability. In light of this problem, a converter-based power system stabilizer (CBPSS) is proposed. By generating an additional damping torque with the developed CBPSS, the stability and dynamic performance of the islanded microgrid can be improved in the face of disturbance. In addition, an eigenvalue-mobility-based approach is also presented to guide the selection of the optimal installation location for the proposed CBPSS in islanded microgrids, and thus the design work of the proposed CBPSS could be further simplified.

Then, the instability caused by CPLs for power-electronic-dominated power systems is studied. In addition to the application on the power generating side, power converters are also widely employed to interface loads with power grids. The tightly regulated power converters on the load side behave as CPLs, featuring negative incremental impedance and introducing adverse impacts on the stability of power-electronic-dominated power systems. Moreover, with the increase of the power level of CPLs, such adverse effects also grow, and finally, it may trigger instability, threatening the security and reliability of the whole system. In light of the instability problem resulting from CPLs, two control schemes, e.g., a damper-based scheme and a stabilizer-based scheme, are proposed to handle the instability issue.

In summary, the overall research objective of the thesis is the analysis and control of several critical stability issues in the emerging power-electronic-dominated power systems. The stability issues focused on in the thesis include the frequency stability associated with the lack of inertia, the power interaction stability of islanded microgrids, and the stability issues regarding CPLs in power-electronic-dominated power systems. Different control stages of

---

power converters dominate these stability problems mentioned above, with their typical response times varying from seconds to dozens of milliseconds. Causes for these stability issues are analyzed in-depth, and corresponding stability control schemes are also developed in this thesis. With such effort, the stability and security of the emerging power-electronic-dominated power systems can be enhanced.



---

## Acknowledgements

Upon completing this thesis, I am grateful to those who have offered me encouragement and support during my Ph.D. study.

First, I would like to express my heartiest gratitude to my respectable supervisor, Prof. Tang Yi, for his invaluable advice, continuous support, and patience during my Ph.D. study. He treats scientific research as a work of art and strives for excellence, and I still remember the first time I wrote a journal paper, the draft of more than twenty pages was densely covered with all the marks of Prof. Tang's corrections, from wording to the punctuation. This spirit influenced the way I do research and deeply reinvented the way I live my life. In addition, his immense knowledge and ample experience have encouraged me all the time of my study, and he never gave me up even during the toughest time during my Ph.D. journey. It is him who opens the door to a wide and wonderful world for me, and it is my most incredible luck to have him as my supervisor.

Then, I also would like to extend my most profound appreciation to my co-supervisor, Prof. David Frey, from G2E Lab, University Grenoble Alpes CNRS. During my days in Grenoble, he gave me every care and attention to help me integrate into the local life in France. Moreover, His extensive engineering experience provided me with much practical insight into my scientific research, making me think more holistically, and his positive and upbeat attitude also encouraged me to keep on moving forward. Even when I was called back to Singapore due to the pandemic, he offered me continuous care and guidance across time and geographical distances between Singapore and France.

Also, I would like to acknowledge the other members of my Thesis Advisory Committee, including Prof. Duan Fei and Prof. Wang Peng, from Nanyang Technological University, and Prof. Seddik Bacha and Prof. Yves Lembeye, from University Grenoble Alpes. They provided helpful suggestions on improving the quality of the thesis.

---

Special thanks go to my seniors and colleagues for lending me their expertise and intuition to my scientific and technical problems: Dr. Fang Jingyang, Dr. Qi Yang, Dr. Zhang Li, Dr. Chen Shuxin, Dr. Qiu Huan, Mr. Yu Jiale, and Ms. Deng Han. I also would like to thank the support provided by the administrator Ms. Huang Minying and Dr. Bahulayan at Energy Research Institute @ NTU (ERI@N).

Last but not least, I wish to express my endless gratitude to my beloved parents, my grandmother, and my sister. Thank them for always believing in me, supporting me, and being by my side with unwavering determination all through these years. Moreover, during the pandemic of COVID-19, we discovered heroes in our lives: doctors, nurses, porters, truck drivers, cleaners, delivery people, and supermarket crews. Upon completing this thesis, I would like to offer my sincere and utmost respect to these unsung heroes in everyday life, whom we used to take for granted.

---

## Table of Contents

<b>Abstract</b> .....	<b>i</b>
<b>Acknowledgements</b> .....	<b>v</b>
<b>Table of Contents</b> .....	<b>vii</b>
<b>Table Captions</b> .....	<b>xi</b>
<b>Figure Captions</b> .....	<b>xiii</b>
<b>Abbreviations</b> .....	<b>xix</b>
<b>Chapter 1 Introduction</b> .....	<b>1</b>
1.1. Background .....	2
1.1.1. Carbon Neutrality and Renewable Energy .....	2
1.1.2. Power Electronic Converters .....	5
1.1.3. Microgrids .....	9
1.1.4. Power-Electronic-Dominated Power Systems .....	12
1.2. Motivation and Objectives .....	14
1.2.1. Motivation .....	14
1.2.2. Objectives .....	15
1.3. Major Contributions .....	17
1.4. Thesis Organization .....	18

---

<b>Chapter 2 Frequency Stability of Power-Electronic-Dominated Power Systems.....</b>	<b>23</b>
2.1. Introduction .....	24
2.2. Frequency Instability with the Reduction of Inertia.....	26
2.2.1. Frequency Instability Caused by the Lack of Inertia .....	26
2.2.2. Virtual Inertia Provided by GCCs.....	28
2.3. Autonomous DC-Link Voltage Restoration for GCCs Providing Virtual Inertia.	32
2.3.1. Effect of the HPF on the Inertial Supportability of GCCs .....	33
2.3.2. Impact of Cut-Off Frequency on DC Voltage Restoration Time.....	40
2.3.3. Design Procedure of the HPF.....	46
2.4. Case Study.....	48
2.4.1. Simulation Results.....	48
2.4.2. Experimental Results.....	51
2.5. Summary .....	55
<b>Chapter 3 Stability Issue Regarding Droop Control in Islanded Microgrids .....</b>	<b>57</b>
3.1. Introduction .....	58
3.2. Stability Problem with Droop Control .....	61
3.2.1. Model of VSC Subsystem.....	62
3.2.2. Model of the Microgrid with the CBPSS.....	66
3.3. Converter-Based Power System Stabilizer for Stability Enhancement of Droop- Controlled Islanded Microgrids .....	68
3.3.1. Optimal Installation Location of the Proposed CBPSS .....	68
3.3.2. Design of the Proposed CBPSS .....	70
3.4. Case Study.....	74
3.4.1. Modal Analysis .....	74
3.4.2. Time-Domain Simulations .....	83



---

3.4.3.	Experimental Verification.....	86
3.5.	Summary .....	89
 <b>Chapter 4 Stability Issue Associated with Constant Power Loads for Power-Electronic-Dominated Power Systems .....</b>		<b>91</b>
4.1.	Introduction .....	92
4.2.	Instability Problem Induced by CPLs .....	94
4.2.1.	System under Study.....	94
4.2.2.	CPL Induced Instability .....	103
4.3.	Stability Enhancement Approaches for CPLs.....	110
4.3.1.	Equivalence between Integral Control and Motion Equation .....	110
4.3.2.	Approach 1: A Damper-Based Scheme to Improve the System Stability in the Face of CPL.....	112
4.3.3.	Approach 2: A Stabilizer-Based Scheme to Enhance the System Stability in the Face of CPL .....	115
4.4.	Case Study.....	120
4.4.1.	Damper-Based Stability Improvement Scheme .....	120
4.4.2.	Stabilizer-Based Stability Enhancement Scheme .....	126
4.5.	Summary .....	132
 <b>Chapter 5 Conclusions and Future Work.....</b>		<b>135</b>
5.1.	Conclusions .....	136
5.2.	Future Work .....	137
 <b>Author's Publications .....</b>		<b>141</b>
 <b>Reference.....</b>		<b>143</b>



---

## Table Captions

**Table 2.1:** System parameter values.

**Table 3.1:** The Microgrid specification under study.

**Table 3.2:** Eigenvalue mobility of VSCs to the critical mode  $\lambda_1$ .

**Table 3.3:** CBPSS parameters when installed at VSC 2.

**Table 3.4:** Eigenvalues with CBPSSs installed at different VSCs.

**Table 3.5:** Participation factors of the critical mode  $\lambda_1$ .

**Table 3.6:** Hardware experiment parameters.

**Table 3.7:** CBPSS parameters in hardware experiments.

**Table 4.1:** Circuit parameters of the MEA electrical system.

**Table 4.2:** Control parameters of the MEA electrical system.

**Table 4.3:** Oscillation modes of the MEA electrical system.

**Table 4.4:** Oscillation modes of the MEA electrical system with the damper.

**Table 4.5:** Parameters of the proposed stabilizer.

**Table 4.6:** Oscillation modes of the example system with the stabilizer.



---

## Figure Captions

**Figure 1.1:** Carbon emission in 2020 breaking up in sectors.

**Figure 1.2:** Worldwide annual additions of renewable power capacity from 2014 to 2020, by technology and total [4].

**Figure 1.3:** Circuit configuration of a two-level three-phase voltage source converter.

**Figure 1.4:** Circuit and control architecture of a grid-feeding converter.

**Figure 1.5:** Circuit and control architecture of a grid-forming converter.

**Figure 1.6:** Hierarchical control architecture of microgrids.

**Figure 1.7:** An example of the power-electronic-dominated power systems.

**Figure 1.8:** Illustration of the overall organizational structure for the thesis.

**Figure 2.1:** Effect of inertia in a low-frequency event.

**Figure 2.2:** Simplified structure of a typical power system with power-electronic-coupled components.

**Figure 2.3:** Schematic of the GCC equipped with the virtual inertia control.

**Figure 2.4:** Block diagram of the frequency regulation architecture including the proposed DC-link voltage restoration block.

---

**Figure 2.5:** Comparisons between  $G_{PL\Box f}(s)$  and its simplified second-order form. (a) Pole-zero map. (b) Frequency response under 4% step-up load change.

**Figure 2.6:** Relationships between the dynamic performance indices and the value of the cut-off frequency  $f_{cut}$ . (a) RoCoF  $|df/dt|_{t=0s}$ . (b) Overshoot  $\sigma$ . (c) Frequency nadir  $f_{nadir}$ . (d) Settling time  $t_s$ .

**Figure 2.7:** Relationship between  $f_{cut}$  and the index  $\mu$ .

**Figure 2.8:** DC-link voltage responses (under a 4% step-up load change).

**Figure 2.9:** Step responses of  $\Delta V_{dc}(t)$ ,  $\Delta V_{dc\_2-order}(t)$  and  $\Delta V_{dc\_1-order}(t)$  as a function of  $f_{cut}$ . (a)  $\Delta V_{dc}(t)$ . (b)  $\Delta V_{dc\_2-order}(t)$  and  $\Delta V_{dc\_1-order}(t)$ .

**Figure 2.10:** Relationship between the DC-link voltage restoration time  $t_{res}$  and the cut-off frequency  $f_{cut}$ .

**Figure 2.11:** Restoration times  $t_{res}$  of the 1-order subsystem  $\Delta V_{dc\_1-order}(t)$  and the DC-link voltage deviation  $\Delta V_{dc}(t)$ . (a) Restoration time estimated from  $\Delta V_{dc\_1-order}(t)$ . (b) Restoration time calculated from  $\Delta V_{dc}(t)$ .

**Figure 2.12:** Design flowchart of the cut-off frequency  $f_{cut}$ .

**Figure 2.13:** Simulation results of frequency and DC-link voltage responses to 4% step-up load changes. (a) Post-disturbance frequency responses. (b) Post-disturbance DC-link voltage responses.

**Figure 2.14:** Simulation results of DC-link voltage responses to grid frequency fluctuations in normal operating conditions. (a) Grid frequency. (b) DC-link voltage.

**Figure 2.15:** Schematic diagram of the experimental small-scale power system.

---

**Figure 2.16:** Photo of the experimental platform.

**Figure 2.17:** Steady-state experimental waveform.

**Figure 2.18:** Experimental results of the systems with and without the proposed DC-link voltage restoration method during 4% cascading step-up load changes.

**Figure 2.19:** Experimental results of the DC-link voltage responses under normal operating conditions.

**Figure 3.1:** Diagram of a typical islanded microgrid.

**Figure 3.2:** Active power droop control of the  $i$ th VSC.

**Figure 3.3:** Active power control in the motion equation form.

**Figure 3.4:** Reactive power droop control of the  $i$ th VSC.

**Figure 3.5:** Coordinate transformation.

**Figure 3.6:** Closed-loop model of the microgrid with the CBPSS.

**Figure 3.7:** Motion-equation form of the closed-loop system.

**Figure 3.8:** Structure of the CBPSS.

**Figure 3.9:** Pole map of the microgrid without CBPSS.

**Figure 3.10:** Critical mode eigenvalue distribution with the CBPSS equipped at VSC 1, VSC 2, and VSC 3.

---

**Figure 3.11:** Phase portrait of VSC output currents with the CBPSS equipped on different VSCs. (a)  $dq$ -axis output currents of VSC 1. (b)  $dq$ -axis output currents of VSC 2. (c)  $dq$ -axis output currents of VSC 3.

**Figure 3.12:** Pole map of the microgrid with CBPSS placed at VSC 2.

**Figure 3.13:** Root locus with the change of  $m_{p2}$ .

**Figure 3.14:** System phase portrait on the  $(\Delta i_{odi}, \Delta i_{oqi})$ -plane with the CBPSS installed on VSC 2. (a) output  $dq$ -axis currents of VSC 1. (b) output  $dq$ -axis currents of VSC 2. (c) output  $dq$ -axis currents of VSC 3.

**Figure 3.15:** Effect of the proposed CBPSS in suppressing microgrid oscillations. (a)  $d$ -axis output current of VSC 1. (b)  $d$ -axis output current of VSC 2. (c)  $d$ -axis output current of VSC 3.

**Figure 3.16:** Expanded microgrid stability margin with the proposed method.

**Figure 3.17:** Photo of the laboratory prototype setup.

**Figure 3.18:** Steady-state voltage and current waveforms.

**Figure 3.19:** Post-disturbance power and current waveforms.

**Figure 4.1:** A gear-less configuration for the power system on MEA.

**Figure 4.2:** Equivalent MEA electrical system.

**Figure 4.3:** Coordinate transformation.

**Figure 4.4:** Cascaded control architecture of the VSC.



---

**Figure 4.5:** Cascaded control structure of the AFE.

**Figure 4.6:** Eigenvalue distribution of the MEA electrical system in presence of CPL.

**Figure 4.7:** Root locus of the critical mode with the change of CPL power level.

**Figure 4.8:** Change of the critical mode damping ratio with the increase of CPL power level.

**Figure 4.9:** Participation factor analysis of the critical mode.

**Figure 4.10:** Damping ratio of the critical mode as impacted by the voltage control parameters of the VSC and the AFE.

**Figure 4.11:** The relationship between the damping ratio of the critical mode with the VSC control parameters and the AFE control parameters. (a) Damping ratio in relationship with  $K_C$ . (b) Damping ratio in relationship with  $K_L$ .

**Figure 4.12:** Voltage control of the VSC.

**Figure 4.13:** Motion equation of synchronous generators.

**Figure 4.14:** A damper-based scheme to mitigate the CPL instability issue.

**Figure 4.15:** Structure of the proposed damper.

**Figure 4.16:** Flowchart for designing the proposed damper.

**Figure 4.17:** A stabilizer-based scheme to mitigate the CPL instability issue.

**Figure 4.18:** Structure of the proposed stabilizer.

---

**Figure 4.19:** Signal-flow graph of the system with the proposed stabilizer.

**Figure 4.20:** Closed loop model of the MEA electrical system with the stabilizer.

**Figure 4.21:** Flowchart for designing the proposed stabilizer.

**Figure 4.22:** Eigenvalue distribution with the proposed damper.

**Figure 4.23:** Response to the DC-link voltage step up of the VSC three-phase output voltage  $u_{oC}$  with and without the damper.

**Figure 4.24:** Response to the DC-link voltage step up of the AFE DC side variables with and without the damper. (a) Input current of the CPL  $I_{CPL}$ . (b) DC-link voltage of the AFE  $U_{dc}$ .

**Figure 4.25:** Response to the CPL 100% power step up of the AFE DC side variables with and without the damper. (a) Input current of the CPL  $I_{CPL}$ . (b) DC-link voltage of the AFE  $U_{dc}$ .

**Figure 4.26:** Eigenvalue distribution with the proposed stabilizer.

**Figure 4.27:** Response to the DC-link voltage step up of the VSC three-phase output voltage  $u_{oC}$  with and without the stabilizer.

**Figure 4.28:** Response to the DC-link voltage step up of the AFE DC side variables with and without the stabilizer. (a) Input current of the CPL  $I_{CPL}$ . (b) DC-link voltage of the AFE  $U_{dc}$ .

**Figure 4.29:** Response to the CPL 100% power step up of the AFE DC side variables with and without the stabilizer. (a) Input current of the CPL  $I_{CPL}$ . (b) DC-link voltage of the AFE  $U_{dc}$ .

---

## Abbreviations

AEMO	Australia Energy Market Operator
AFE	Active Front End
AVR	Automatic Voltage Regulator
CBPSS	Converter-Based Power System Stabilizer
CPL	Constant Power Load
CPS	Cyber Physical System
DFIG	Double-Fed Induction Generator
ESS	Energy Storage System
GCC	Grid-Connected Converter
HPF	High-Pass Filter
MEA	More Electric Aircraft
MPC	Model Predictive Control
MPPT	Maximum Power Point Tracking
NMG	Networked Microgrid
PI	Proportional and Integral
PLL	Phase-Locked Loop
PSS	Power System Stabilizer
PV	Photovoltaic
PWM	Pulse-Width Modulation
RoCoF	Rate of Change of Frequency
SG	Synchronous Generator
SMIB	Single-Machine-Infinite-Bus
UFLS	Under-Frequency Load Shedding
VSC	Voltage Source Converter
VSynC	Virtual Synchronous Control



---

# Chapter 1

## Introduction

*This chapter introduces the background regarding the research topic of this thesis, including the target of carbon neutrality, the evolution towards power-electronic-dominated power systems, and the fundamentals of power converters and microgrids. Besides, challenges of power-electronic-dominated power systems are also demonstrated, serving as the motivation of the thesis. Finally, the objective as well as organization of the thesis is illustrated.*

---

## 1.1. Background

### 1.1.1. Carbon Neutrality and Renewable Energy

With extreme weather conditions such as drought, heat waves, and heavy rains becoming the new normal, global warming and climate change have significantly affected the entire world, and the average temperature in the past decade hit its new highest record compared with historical data. To align with the objectives signed in Paris Agreement and limit global warming to 1.5 degrees Celsius, countries representing more than 65 percent of greenhouse gas production have committed to reducing carbon emissions extensively and achieving carbon neutrality by the middle of this century. Fig. 1.1 demonstrates the worldwide total CO<sub>2</sub> emission broken down into different sectors for 2020, among which the power sector is the single largest source of CO<sub>2</sub> emission, accounting for almost 40% [1]. Thus, starting from the energy supply side, promoting the complete decarbonization in the power sector and advocating the transformation from fossil-fuel-based generation to low-emission and renewable-energy-based generation is the key to achieving the carbon neutrality target.

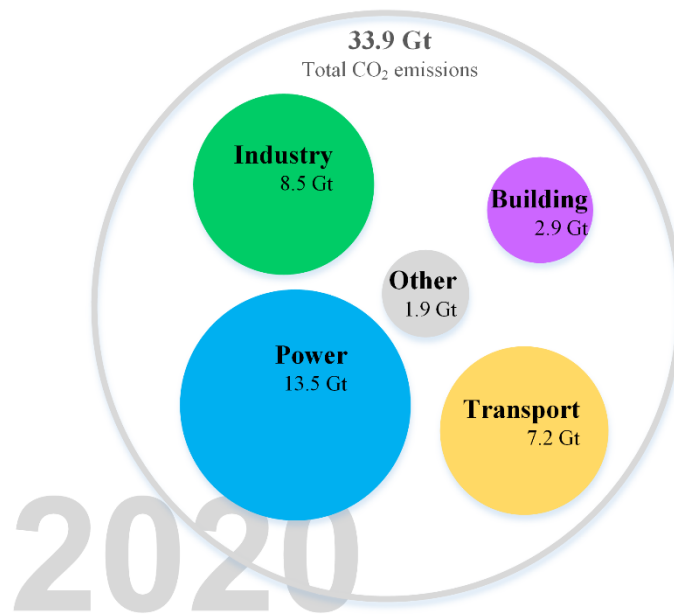


**Figure 1.1** : Carbon emission in 2020 breaking up in sectors.

---

Typical renewable energies include hydropower, solar power, and wind power. Hydropower plants have been maturely used for decades to produce renewable energy, which is relatively inexpensive and accessible [2]. However, the exploitation of hydropower is limited by geographic environments, and there are debates concerning the detrimental impacts of hydropower exploitation on aquatic ecosystems [3]. Besides, most of the favorable sites with abundant hydropower resources have already been developed. In recent years, with the accelerating array of technological advances and the massive reduction in manufacturing costs, a surge in the installed capacity for solar power and wind power has been witnessed worldwide. Fig. 1.2 illustrates the global annual additions of renewable power capacity from 2014 to 2020, in which the annual additions of the renewable power capacity maintain a sustained growth for six consecutive years despite the turbulence induced by the onset of the COVID-19 pandemic [4]. As a result, more than 256 GW of renewable power capacity has been brought online during 2020, raising the total global capacity for renewable power to an all-time high of 2,839 GW by the end of the year. By breaking down the annual addition of renewable power capacity in 2020 into different renewables, it is observed that the solar photovoltaic (PV) tops among all kinds of renewable energies with around 139 GW of global annual addition, then followed by the wind power, accounting for about 93 GW of worldwide annual addition.

Despite the positive effect of cutting down the carbon footprint, the ever-increasing capacity of renewable energies significantly influences power systems, and the characteristic of power grids is radically modified as the penetration of renewable energies keeps going high [5]. Unlike fossil-fuel-based energy sources, which are considered dispatchable with flexibly adjusted outputs to meet load-side demand, renewable energies, such as solar power and wind power, feature variable, and uncertain power outputs, and the power production heavily depends on local weather conditions [6]. For example, solar power demonstrates a remarkable characteristic of the diurnal, seasonal cycle since PV panels output no power during nights, and the solar radiation varies drastically across different seasons [7]. Besides, even during daytime hours, the frequently passing clouds have influential impacts on the output power of PV panels, leading to random and highly fluctuating power output profiles. Similar things happen to wind power, and there tends to

be more wind power production during nighttime hours than during daytime hours. Besides, the output power between individual renewable generators demonstrates a high correlation, with a large amount of power generation crowding in relatively narrow time windows, and this may further exacerbate the imbalance between power supply and load demand in power systems. Massive studies have validated that the renewable energies accompanied by significant fluctuation, strong randomness, and high correlation would pose crucial challenges to grid operators in terms of power dispatch and stability control [8, 9]. It may give rise to instability problems such as frequency deviation, unscheduled load shedding, voltage collapse, grid splitting, and even system-wide shutdown. Different solutions have been provided to clear up these issues, including geographic diversity for various renewable generation sites to smooth output power fluctuation and inter-regional power transmission to alleviate local supply-demand mismatch. Besides, the cooperation of energy storage with renewable generation is a promising approach [10-12]. It yields a more dispatchable portfolio, but the deployment of energy storage in power systems is still limited by the high expense so far.

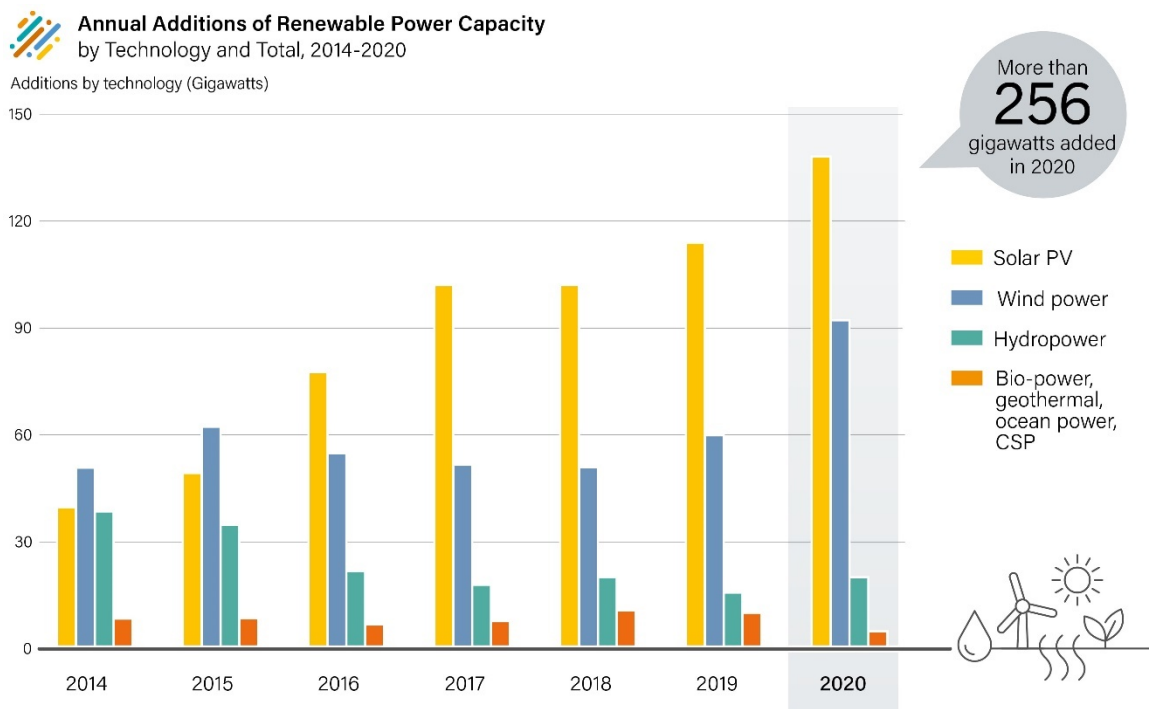


**Figure 1.2 :** Worldwide annual additions of renewable power capacity from 2014 to 2020, by technology and total [4].



---

In addition to the issues mentioned above, the high penetration of renewable energies calls for a broad application of fast-response power electronic converters to realize energy conversion and serve as the interface between grids and renewable generators, for instance, PV panels and wind turbines. Opposite to conventional synchronous generators, which have rotating components with mechanical inertia to support frequency stability in the face of disturbance naturally, power electronic converters are strictly static with no rotating masses [13]. Moreover, renewable generators are tightly regulated by these interface power converters to extract the maximum available power from primary energy sources. Thus the dynamics of renewable generators are fully decoupled from the grid side [14]. Consequently, the converter-interfaced renewable generation system cannot respond to grid-side frequency events in emergencies and is regarded as inertia less from the perspective of power systems [15, 16]. With the share of renewable energies in power grids increasing worldwide, the total inertia for power systems declines significantly, accompanied by an expanding risk of instability [17, 18]. In this regard, an upper limit for the penetration level of renewable energies in power grids has been commonly adopted in different countries, capped at 600 MW in Singapore, for example, far from enough compared to the peak load of 7,000 MW [19].

### **1.1.2. Power Electronic Converters**

As described above, renewable power generation is tightly associated with high fluctuation and strong randomness. Consequently, in power systems with high penetration of renewable energies, power electronic converters are widely adopted, serving as the interface between renewable generators and power grids to guarantee steady and grid-compatible power outputs. Fig. 1.3 demonstrates a typical configuration for a three-phase voltage source converter (VSC), in which the “on” and “off” states of power semiconductor switches are controlled by pulse-width modulation (PWM) waves at a fast timescale to realize the power conversion from DC form to AC form [20]. However, the direct outputs from power semiconductor switches are square waves, in which the desired voltage component at the fundamental frequency is accompanied by a large amount of unfavorable

high order switching harmonics. The presence of massive harmonics gives rise to severe power quality issues, which may further lead to increased heating of machines and transformers, malfunctioning of protective relays, and misoperation of electronic devices [21-23]. One simple but effective solution to prevent harmonics from spreading into power grids is installing passive filters at the output ports for power converters, as illustrated in Fig. 1.3. The common realization of passive filters varies from the simplest form, e.g., a single inductor  $L$ , to a more complicated third-order  $LCL$  form with better harmonic attenuation and smaller size, depending on the application scenarios [24, 25]. With power semiconductor switches and passive filters, the transformation of voltage waveforms from the initial DC form to the AC square-wave form and eventually to the grid-compatible AC sinusoidal form is demonstrated in Fig. 1.3.

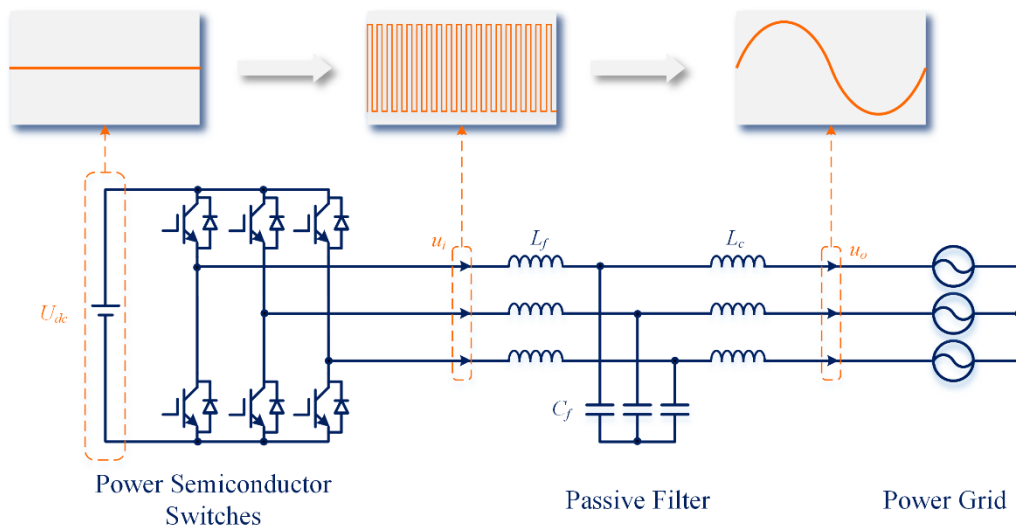


**Figure 1.3 :** Circuit configuration of a two-level three-phase voltage source converter.

In addition to the hardware circuits, as mentioned earlier, closed-loop control architectures are also required to regulate the power flow of power converters and generate the reference waveforms for PWM [26, 27]. Unlike conventional synchronous generators, of which the transient behavior is primarily determined by the physical properties of mechanical structures and inner circuit parameters, the dynamics of power converters are fundamentally dictated by their control architectures. Therefore, by choosing different control strategies, the performance of power converters varies significantly, providing a

higher degree of control flexibility compared with synchronous generators [28]. According to the control strategies applied, power converters can be classified into the grid-feeding and grid-forming types.

The grid-feeding type signifies the most dominant operating mode for power converters, and grid-feeding converters are widely employed in solar power and wind power generation scenarios to transmit energy to power systems [29, 30]. A grid-feeding converter can be regarded as an ideal current source. Its typical configuration and control architecture is depicted in Fig. 1.4, in which an outer power control is cascaded with an inner current control to track power references  $P_{ref}$  and  $Q_{ref}$ . A phase-locked loop (PLL) is utilized to synchronize the grid-feeding converter with the interconnected utility grid by tracking the voltage vector at its terminal [31]. In some cases, the power control is replaced by DC-link voltage control, and by maintaining a constant DC-link voltage of power converters, the power balance between the DC and AC sides is achieved indirectly [32].

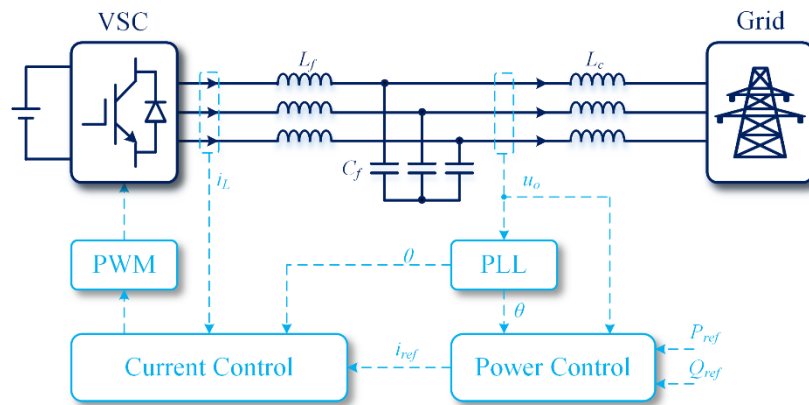


**Figure 1.4 :** Circuit and control architecture of a grid-feeding converter.

A grid-feeding converter is suitable to operate in parallel with other grid-feeding converters, and these converters can also be managed to contribute to voltage and frequency regulations, with an upper-level decision center coordinating power references  $P_{ref}$  and  $Q_{ref}$  between different individuals [33]. Nonetheless, the operation of grid-feeding converters necessitates a stiff voltage featuring minor amplitude and frequency deviations, with which the grid-feeding converters could work to track the stiff voltage and inject controlled

currents [34]. Due to this limitation, grid-feeding converters cannot operate alone without synchronous generators or utility networks producing the required stiff voltage.

In light of the limitations for grid-feeding converters, the development of grid-forming converters is highly welcomed in power systems with high penetration of renewable energies. In contrast to grid-feeding converters, which operate as current sources, grid-forming converters can be analogized to ideal voltage sources. Besides, with the ability to regulate their terminal voltages in terms of amplitude and frequency, grid-forming converters can operate autonomously in an islanded mode without relying on other power generation units to maintain the stiff voltage. As a result, the utilization of grid-forming converters promotes the transition of power systems from the synchronous-generator-based paradigm to the inverter-based paradigm.

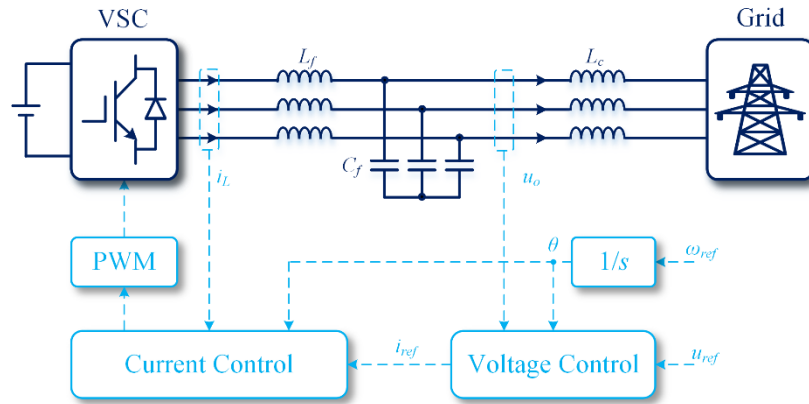


**Figure 1.5 :** Circuit and control architecture of a grid-forming converter.

A typical configuration for a grid-forming converter are demonstrated in Fig. 1.5, in which an outer voltage controller is cascaded with an inner current controller [35]. With inputs of the control architecture defined as the reference of the voltage, which is to be synthesized by the grid-forming converter, the outer loop regulates the voltage to reference values for the point of common coupling, and the inner loop controls the inductor current  $i_L$  to follow the current reference generated by the outer loop. Besides, either the inductor current or the capacitor current can be utilized as feedback to realize active damping. In addition, according to the manner of generating reference  $u_{ref}$  and  $\omega_{ref}$ , the control strategies of grid-

---

forming converters can be further classified into droop control [36, 37], virtual synchronous generator control [38, 39], and virtual oscillator control [40].

### **1.1.3. Microgrids**

Instead of the bulky power systems with centralized power generation, the utilization of renewable energies gives rise to the wide application of microgrids, and the global market for microgrids is forecast to hit a total amount of \$31.2 billion by 2022, with a compound annual growth rate of 19.6% [41]. Among renewables, solar and wind power generation, which are smaller in capacity and more scalable in configuration, are especially suitable for deployment in microgrids [42]. Furthermore, by integrating renewable generators with diesel or gas-fueled generators and energy storage systems, microgrids provide premium power supply solutions, featuring diversified energy source portfolios with enhanced reliability and reduced carbon emission. Besides, through advanced control, the operation of microgrids may switch flexibly between grid-connected modes and islanded modes. Such flexibility benefits local users with a higher degree of freedom in energy management and on-demand generation, and a lower cost is offered to microgrid customers by offsetting expensive peak loads with local generation [43]. In addition, without the need to construct long-distance transmission infrastructures required in conventional power systems, microgrids operating in islanded modes are cheaper and easier to roll out, providing remote users with accessible and inexpensive power supplies. Another vision is to strengthen grid resilience with networked microgrids (NMG) [44], which consists of a cluster of physically interconnected and functionally interoperable microgrids. In this manner, the system-wide outage would become a thing of the past.

Since various power generation units are interconnected in the same microgrid, a hierarchical control architecture is commonly applied to microgrids so that different generating units can be harmonized to maximize operating efficiency and guarantee reliability [43, 45]. A typical three-layer hierarchical control architecture is illustrated in Fig. 1.6, including primary control, secondary control, and tertiary control.

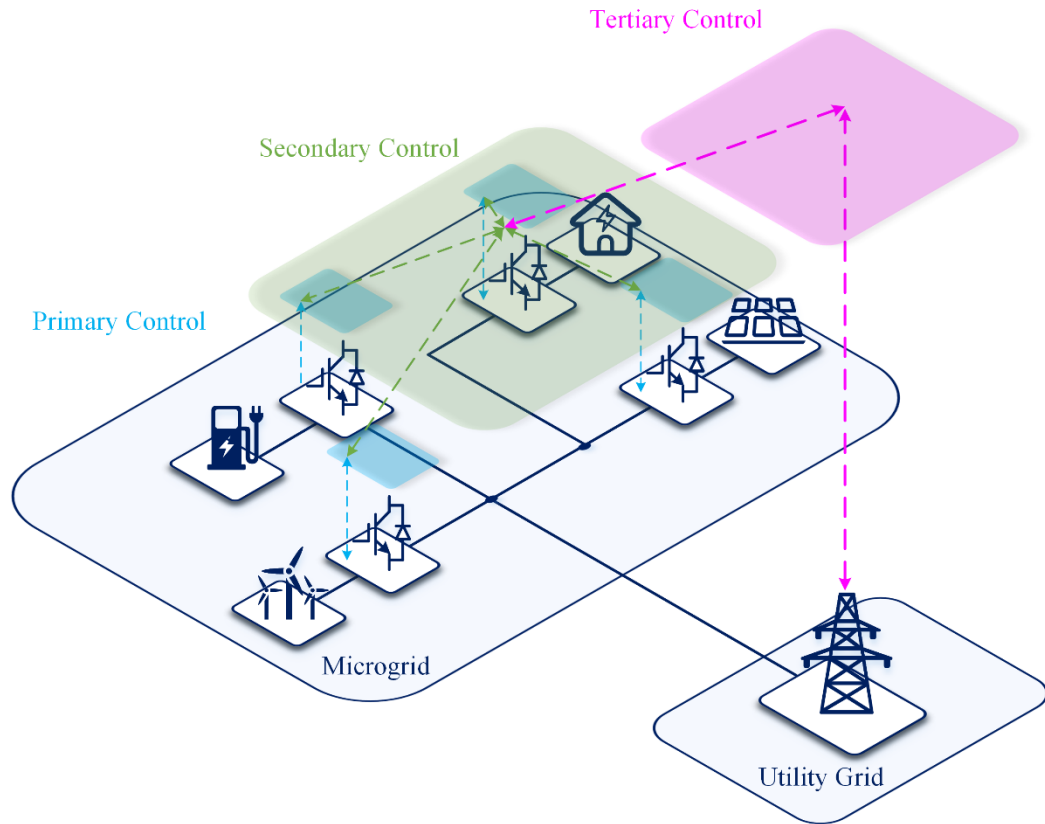


**Figure 1.6 :** Hierarchical control architecture of microgrids.

Primary control is implemented locally, directly interacting with individual generating units and regulating local variables, such as frequency, currents, and voltages [46]. One critical issue in primary control is the power-sharing among multiple generating units. Different strategies have been explored to settle this issue, such as centralized controllers with master-slave structures [47, 48] and decentralized controllers with information exchanged between neighbors [49-51]. However, both approaches require additional high-band communication channels for real-time information transmission, incurring additional capital outlay and leading to degraded reliability once communication failure occurs [52]. In addition, since power converters feature fast dynamic responses, time delays regarding communication channels may cause instability issues for microgrids [53, 54].

In light of these problems, droop control is broadly applied in microgrids to realize power-sharing between generating units [55, 56]. Moreover, the implementation of droop control only needs local frequency information, thus free from drawbacks and risks associated with

---

communication channels. Besides, with the compatibility with conventional synchronous generators, droop control also makes it possible for renewable generators to plug and play, coinciding with the flexibility of microgrids [57]. The basic idea of droop control lies in mimicking the self-regulation capability of synchronous generators. With droop control, the output power will be reduced naturally when grid frequency goes beyond the nominal value and vice versa. However, the approximate proportional relation between active power output and grid frequency only holds in inductive grids, and thus the application of droop control is limited by grid conditions. To overcome this limitation, a virtual output impedance could be incorporated in primary control by subtracting a virtual voltage drop from the output voltage reference [58-60]. As a consequence, the grid turns into inductive from the perspective of generating units, thereby the premise of utilizing droop control is satisfied.

In addition to primary control, the actions of all power generation units in a microgrid are coordinated by secondary control. With wide-area monitoring systems, secondary control serves as a centralized automatic generation controller, compensating steady-state errors and restoring frequency and voltage values to nominal ones [61, 62]. Apart from secondary control, tertiary control is in charge of optimizing microgrid operation based on economic criteria, considering supply-demand balance, marginal power generation costs, and price information from the electricity markets [43]. Furthermore, the management of interactions between microgrids and utility grids is also covered by tertiary control. Typical tasks inside tertiary control include generation forecast, estimation of short-term load variation, and communication with grid operators [63]. Besides, the reserve of secondary control is to be restored with the commands from tertiary control.

Since primary control interacts directly with individual generating units and regulates dynamics of power converters, while secondary control and tertiary control principally focus on steady-state management and economical operation, primary control is in closer relationship with the stability of power generating units, and thus the control architectures involved in the primary layer will be studied in depth in this thesis, and various stability enhancement measures will be developed accordingly.

### 1.1.4. Power-Electronic-Dominated Power Systems

As the total amount of renewable energies integrated in power grids keeps going high, an increasing number of power electronic devices are utilized in modern power systems on both the source sides and the load sides to interface renewable generators with power grids and to achieve satisfying control objectives as well as upgraded power quality. As a consequence, the existing energy paradigm is transforming from the conventional centralized ones relying on synchronous generators to the emerging ones with distributed power-electronic-based power generation, i.e., power-electronic-dominated power systems. A typical structure of the emerging power-electronic-dominated power systems with various energy sources including solar and wind farms and different kinds of loads as well as energy storage units are portrayed in Fig 1.7.

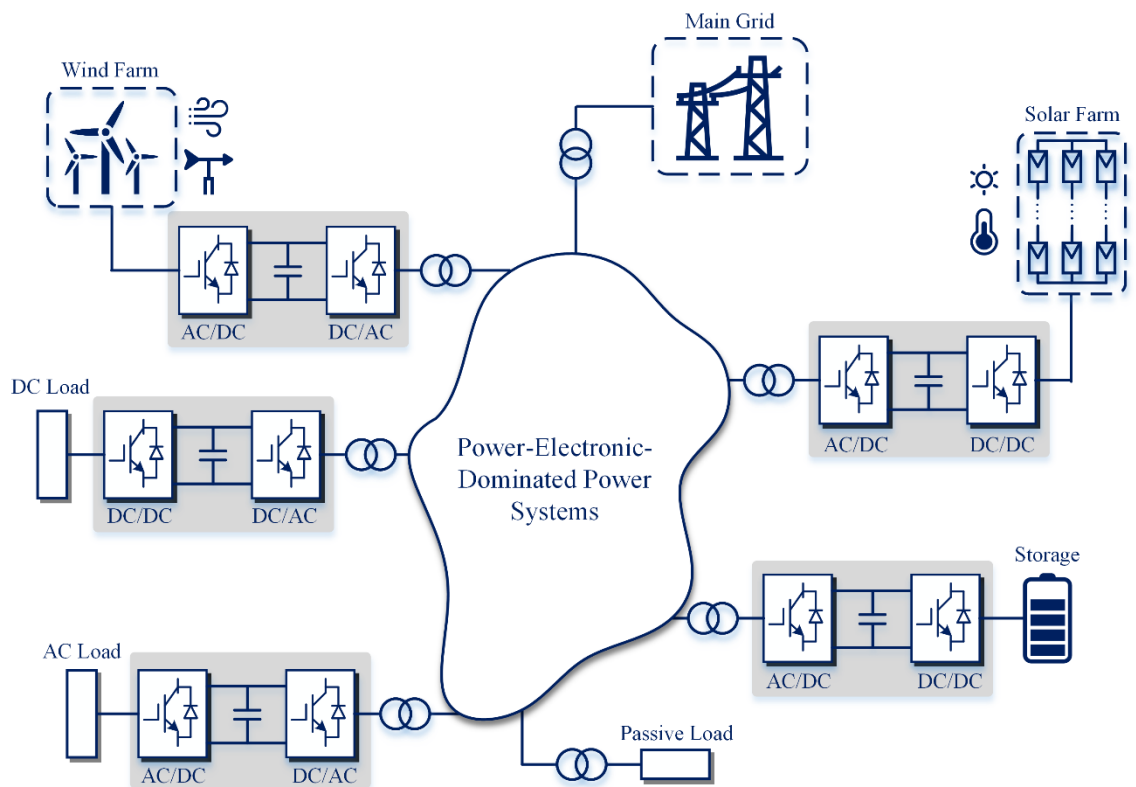


**Figure 1.7:** An example of the power-electronic-dominated power systems.



---

Compared to the conventional centralized synchronous-generator-dominated power grids, which produce electricity by extracting energy from fossil-fuel-based primary energy sources, power-electronic-dominated power systems merit with superior flexibility, and they can be integrated with a mix of clean energy profiles, such as solar power and wind power, contributing to the target of carbon neutrality. Besides, the wide application of microgrids in practice can further benefit power-electronic-dominated power systems with additional degrees of freedom in terms of system planning and grid operating. In addition, due to the ability of bi-directional power flow for power electronic devices, customers are also encouraged to contribute to power regulation and energy management in power-electronic-dominated power systems following the requirements of grid codes, realizing the objective of demand-side response.

However, the widespread use of power converters makes the dynamics of power-electronic-dominated power systems much more complicated compared to the traditional grids. As mentioned in previous sections, the behaviors of power converters are determined primarily by their control strategies, and with different control strategies applied, the responses of power converters change significantly in face of disturbances, consequently making the dynamics of the power-electronic-dominated power systems more varied and unpredictable. Besides, the commonly used cascaded control architecture may lead to multi-timescale coupling among different control loops in power-electronic-dominated power systems, making the grids prone to potential instability issues. Moreover, power electronics are less able to withstand overvoltage and overcurrent compared to synchronous generators, and as a result, the same fault may give rise to more serious damage in power-electronic-dominated power systems than in a conventional synchronous-generator-based power system.

Therefore, with the above-mentioned features, a higher requirement is posed for the emerging power-electronic-dominated power systems in terms of stability analysis and control, and the instability issues associated with power-electronic-dominated power systems need to be identified carefully and investigated in-depth to pursue solutions so that the safety of power-electronic-dominated power systems can be guaranteed.

---

## 1.2. Motivation and Objectives

### 1.2.1. Motivation

The target of carbon neutrality necessitates the massive integration of renewable energies, and due to the fluctuation and randomness regarding renewable energies, power electronic converters are widely deployed to interface renewable generators with power systems, so that grid-compatible power outputs are produced. Consequently, a swift evolution from the traditional synchronous-generator-dominated power systems towards the power-electronic-dominated paradigms can be foreseen.

The structures of power-electronic-dominated systems are becoming more and more complicated, giving rise to new stability problems, with one typical example of the blackout event reported in South Australia in September 2016, which was triggered by extreme weather conditions. The power shutdown lasted from hours to several days in different areas, finally affecting around 850,000 customers with nearly 445 million watts of power loss and \$367 million economic costs [64]. Moreover, in microgrids, which signify an excellent form to accommodate renewable energies, the stability issues associated with power-electronic-dominated systems are highlighted. Since a mix of multiple power electronic interfaced renewable generators, such as wind turbines and solar PV panels, cohabit in the same microgrid, the interactions between different generating units and power converters are more complicated in microgrids. In addition, the typical capacity of microgrids is much smaller compared with the conventional centralized bulky power systems, making microgrids more vulnerable to disturbances. Under this background, the modeling and stability control of power-electronic-dominated power systems has become more critical than ever before, attracting much attention from both industries and academia due to its high stakes and associated disastrous consequences. However, the stability analysis for power-electronic-dominated systems is sophisticated, with root causes and solutions not thoroughly clarified.

---

As a fact, power electronic converters feature fast dynamics, and unlike conventional electromechanical apparatus in synchronous-generator-dominated power systems, the power electronics devices primarily employ cascaded control architectures to guarantee satisfied transient performance. Nonetheless, the response time of different control stages inside such cascaded architecture varies from seconds to dozens of milliseconds, displaying the distinctive characteristic of multi-time scales. Moreover, the control architectures of power converters with different functions also vary significantly, as illustrated in the grid-feeding and grid-forming converters. As such, the multi-time scale characteristic and the variety of control architectures make the analysis and stability control ever more arduous for power-electronic-dominated power systems, and there is no universal solution to all stability issues associated with various time scales and different control architectures for power-electronic-dominated systems. Consequently, a concrete analysis approach should be adopted for specific problems of power-electronic-dominated systems.

### **1.2.2. Objectives**

To shed light on the emerging stability issues in power-electronic-dominated power systems, the objective of this thesis lies in the clarification of root causes for several critical stability problems and the development of control schemes to enhance the stability of power-electronic-dominated power systems. The stability problems under study in this thesis cross several different time scales, including the frequency stability with a time frame of seconds, the power interaction stability with a typical response time of hundreds of milliseconds, and the stability issue regarding constant power loads in the time frame of dozens of milliseconds.

#### **1) Frequency Stability Caused by Reduced Inertia**

As synchronous-generators-based power generation being continuously replaced by converter-interfaced renewable power generation, a significant reduction of inertia is witnessed for power-electronic-dominated power systems, giving rise to frequency

---

stability problems with a typical response time from seconds to tens of seconds. The decline of inertia is because renewable generators are typically operated at the maximum power point tracking (MPPT) mode. Thus, renewable generators do not respond to frequency events as synchronous generators do. Therefore, as the penetration of renewable energies grows, the inertia of the grid decreases remarkably. Furthermore, the ever-decreasing inertia translates into high RoCoF and large frequency deviations, which may cause under-frequency load shedding (UFLS), cascading failures, or even state-wide blackouts.

## **2) Power Interaction Stability for Droop Controlled Islanded Microgrids**

One main concern regarding the broad application of microgrids is the stability issue in the face of disturbances. For microgrids with droop control to realize power-sharing among multiple power generating units, a relatively large droop gain benefits the accurate power-sharing at the expense of sacrificed dynamic stability. Moreover, such a stability issue is associated with the power interactions between multiple power generating units in islanded microgrids, with a tight relationship with the power control stages of power converters, characterized by a typical response time of hundreds of milliseconds. Simply tuning control parameters could not balance the tradeoff between power-sharing and power interaction stability, calling for auxiliary stability controllers to deal with such conflict.

## **3) Instability Problems Regarding Constant Power Loads**

Tightly regulated power converters behave as constant power loads (CPLs), featuring negative incremental impedance. The negative impedance characteristic of CPLs can upset the stability of the interconnected energy conversion stages and even lead to system shutdown, threatening the security and reliability of power-electronic-dominated power systems. Studies indicate that the instability associated with CPLs is primarily related to voltage control loops of power converters, with dynamics signifying a typical response time of dozens of milliseconds. Thus, additional stability controllers need to be designed regarding the voltage control to enhance the stability of power-electronic-dominated power systems with the presence of CPLs.

---

### 1.3. Major Contributions

With the wide application of power electronic devices, the conventional synchronous-generator-denominated power systems are evolving towards the power-electronic-dominated power grids. In this thesis, several critical stability problems in the emerging power-electronic-dominated power systems are analyzed, and the corresponding solutions are developed to enhance the stability of the power-electronic-dominated power systems. The major contributions of the thesis are summarized as follows:

- Several critical stability problems associated with the emerging power-electronic-dominated systems are highlighted with their root causes identified, including the frequency stability with the reduction of inertia, the stability issue regarding droop control in islanded microgrids, and the stability problem associated with CPLs.
- For the frequency stability of power-electronic-dominated power systems caused by the reduction of inertia, a grid-connected converter (GCC) based virtual inertia control scheme is introduced with the utilization of the energy stored in DC-link capacitors. Moreover, an autonomous DC-link voltage restoration method is proposed to overcome the drawbacks of the conventional virtual inertia control scheme, making it possible for GCCs to provide multiple virtual inertia supports in face of cascaded frequency events.
- The stability issue of droop controlled islanded microgrids is analyzed, and a converter-based power system stabilizer (CBPSS) is developed to synthesis a damping torque to the islanded microgrid, with the method to identify the optimal installation location demonstrated. As a consequence, the stability and transient performance of the islanded microgrids during disturbance can be enhanced.
- The instability caused by CPLs in power-electronic-dominated power systems is analyzed, and it is shown that the CPL-induced instability is associated with the

---

voltage control loops of power converters. Furthermore, two schemes, e.g., a damper-based scheme and a stabilizer-based scheme, are proposed to deal with the CPL-induced instability.

#### **1.4. Thesis Organization**

This thesis consists of five chapters, and these chapters are organized according to the timescales of the stability issues under study, from slow to quick, including the frequency stability with a typical response time of seconds, the power interaction stability with a common timescale of hundreds of milliseconds, and the stability issue regarding CPLs in the time frame of dozens of milliseconds. The contents of these chapter are demonstrated in Fig. 1.8 and specified as below, respectively:

Chapter 1 begins with the background of carbon neutrality and highlights the evolution from the synchronous-generator-dominated grids towards the power-electronic-dominated power systems. After that, fundamental knowledge for principal components of power-electronic-dominated grids is introduced, including typical circuit topologies, and commonly used control architectures for power converters and microgrids. Then, several critical stability issues associated with the emerging power-electronic-dominated systems are discussed, serving as the motivation of the thesis. Eventually, the objective of the thesis is to clarify the cause and develop corresponding control schemes for these critical stability problems regarding power-electronic-dominated systems, including frequency stability, droop control stability, and CPL associated stability.

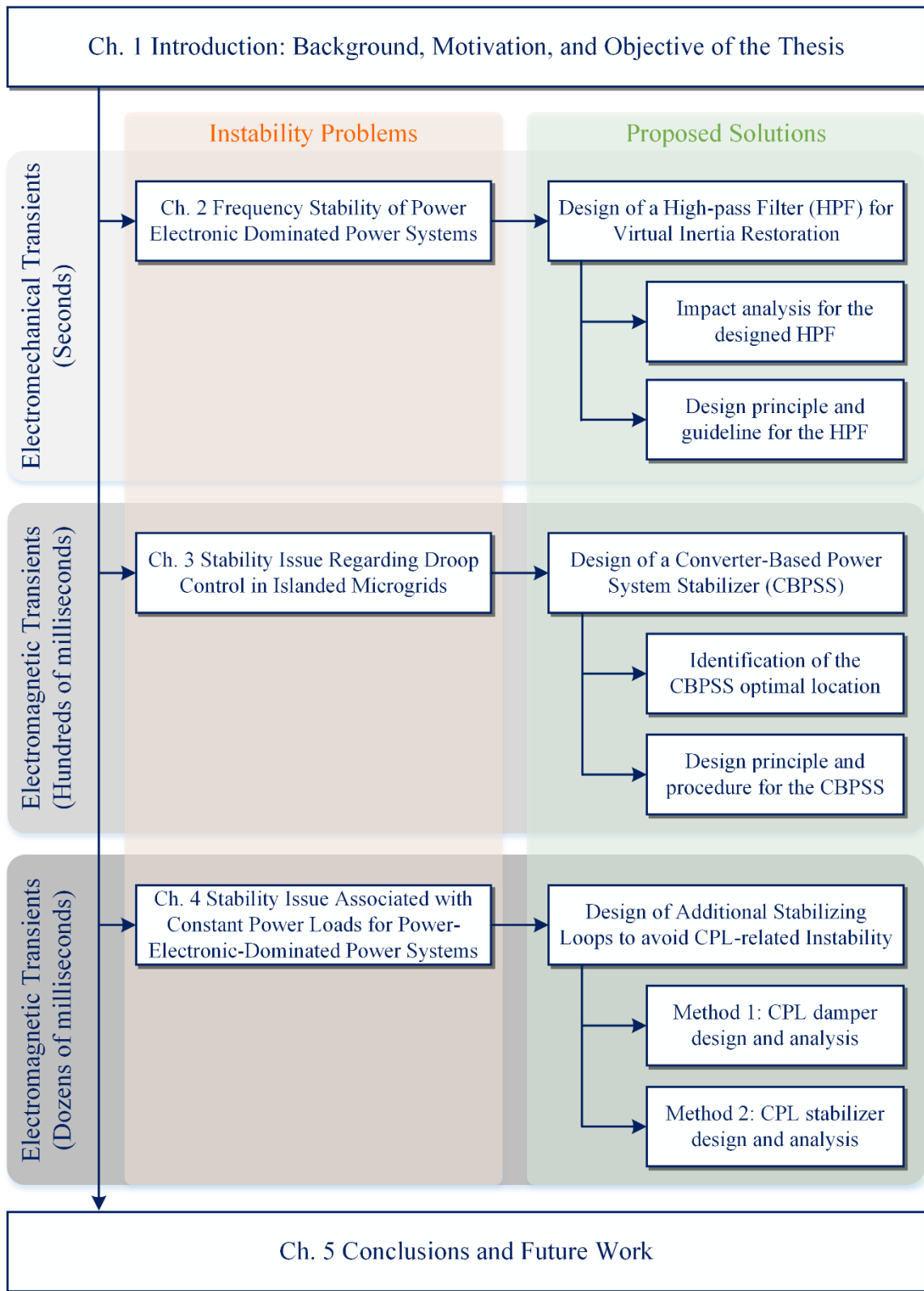


**Figure 1.8** : Illustration of the overall organizational structure for the thesis.

---

Chapter 2 focuses on the frequency stability of power-electronic-dominated power systems, which are resulted from the lack of inertia. First, it is explained that how the lack of inertia translates into the high RoCoF levels and large frequency deviations. Then, a GCC based virtual inertia control scheme is introduced with the utilization of the energy stored in DC-link capacitors. However, due to the proportional relationship between grid frequency and DC-link voltage, the DC-link voltage cannot be restored after providing inertial support in the GCC-based virtual inertia control scheme, thus deteriorating the lifetime of DC-link capacitors, and losing the capability to provide multiple inertial supports in cascading frequency events. In light of these problems, a high pass filter-based method is proposed to recover the DC-link voltage automatically after providing inertial support in this chapter with detailed design procedures.

Chapter 3 studies the stability issue of droop controlled islanded microgrids. For islanded microgrids with droop control to achieve power-sharing among multiple power generating units, a relatively large droop gain benefits the accurate power-sharing at the expense of sacrificed dynamic stability. Moreover, it is revealed that such stability issue is associated with the power control stages of power converters, and simply tuning control parameters could not deal with this stability problem. Therefore, a CBPSS is developed in Chapter 3 to synthesis a damping torque to the islanded microgrid, so that the stability and transient performance can be enhanced. In addition, the approach to identify the optimal installation location of the designed CBPSS is also demonstrated.

Chapter 4 highlights the instability regarding CPLs in power-electronic-dominated power systems. It is illustrated that the tightly regulated power converters behave as CPLs, featuring negative incremental impedance and introducing adverse impacts on the stability of power-electronic-dominated power systems. Moreover, with the increase of the power level of CPLs, such adverse effects also grow, and finally, it may trigger instability, threatening the security and reliability of the whole system. In addition, participation factor studies demonstrate that voltage controllers of power converters principally dominate such instability. In light of this problem, two schemes, e.g., a damper-based scheme and a stabilizer-based scheme, are proposed to deal with the CPL-induced instability.



---

Chapter 5 concludes the main contribution of the thesis, and several new perspectives are also presented as the future research topics. Firstly, the interaction analysis between synchronous generators and power electronic converters is considered as an emerging research topic, especially for power-electronic-dominated power systems, in which the capacity of power converters is comparable with synchronous generators. In addition, as power grids are evolving towards a cyber physical system, consisting with electrical-coupled physical systems and communication-coupled cyber systems, the security of such cyber physical systems under cyber-attacks is considered as another potential research perspective.



---

## Chapter 2

### Frequency Stability of Power-Electronic-Dominated Power Systems

*This chapter focuses on the frequency stability of power-electronic-dominated power systems resulted from the lack of inertia, and the typical response time of frequency stability dynamics is from seconds to tens of seconds. First, it is illustrated in this chapter how the lack of inertia translates into the high RoCoF levels and large frequency deviations. Then, a GCC based control scheme is introduced to provide virtual inertia by utilizing the energy stored in DC-link capacitors. However, due to the proportional relationship between grid frequency and DC-link voltage, the DC-link voltage cannot be restored after providing inertial support, thus deteriorating the lifetime of DC-link capacitors, and losing the capability to provide multiple inertial support during cascading frequency events. In light of such problems, a high-pass filter based approach is proposed to restore the DC-link voltage of GCCs automatically after providing inertial support.*

---

## 2.1. Introduction

The South Australia blackout in 2016 is the first recorded blackout event occurred in the grid with a high penetration of renewable energies, and the renewable generation in the system supplied nearly 50% of the total demand before the blackout [65]. Unlike synchronous generators, renewable generators such as wind turbines and PV arrays are interfaced with power grids through power converters, which have no rotational inertia [66]. This is because renewable generators are normally operated at the maximum power point tracking (MPPT) mode, and thus they do not respond to frequency events as synchronous generators do. Therefore, as the penetration level of renewable energies in power systems grows, the inertia of the grid decreases remarkably [67]. Furthermore, the ever-decreasing inertia leads to high rate-of-change-of-frequency (RoCoF) levels and large frequency deviations [68], which may cause undesirable UFLS, cascading failures [69], or even state-wide blackouts.

As reported by the Australian Energy Market Operator (AEMO), the lack of inertia becomes a new threat to the operation of modern power grids [70]. In [71, 72], pitch angles of wind turbines are controlled such that the turbines operated below the maximum power point, and hence part of the wind energy is reserved for inertia emulation. In [73], a deloading scheme and MPPT control are well coordinated to provide inertia support and frequency droop control. However, the deloading approach necessitates the curtailment of wind power, and thus incurring extra opportunity costs.

Adding an extra power reference to the control of wind turbines, which is in proportion to the RoCoF, is another way to emulate inertia. The resultant inertial power can be released from the rotors of wind turbines to support frequency regulation. In [74-76], the rotor speed is tightly regulated as a function of the RoCoF or the grid frequency deviation to exploit the kinetic energy from rotors for inertia support. In [18], the authors propose a method of tuning the inertia emulated by doubly-fed induction generators (DFIGs) through the design of PLLs. However, as PLLs are mainly used for grid synchronization, the modification of PLLs may deteriorate the control of energy conversion systems [77]. The virtual

---

synchronous control (VSynC) for inertia emulation of DFIGs has been reported in [78] with its effectiveness verified in a weak AC grids. Although these methods can make use of the kinetic energy stored in the rotors of wind turbines and enable them to participate in inertia support, frequent rotor speed variations increase the mechanical stress and reduce the lifetime of wind turbines. More importantly, a second frequency drop may happen during the speed recovery period, which will worsen the power system stability [76].

Recently, energy storage systems (ESSs) are showing great promise for inertia emulation. As an example, an ESS, together with a wind generator, is employed to provide virtual inertia in hope of minimizing frequency deviations [79]. In [80], the flywheel storage system, which is also used in cooperation with a wind generation system, achieves inertia emulation, and a central controller is introduced to coordinate these two systems. A multi-level ESS serving as an energy buffer is connected to the DC-link of the power converter in [81], and it works together with wind turbines for inertia emulation. In [82], the hybrid ESS is employed to regulate the grid frequency, where the supercapacitor emulates the inertia while the battery provides the primary frequency regulation. Although having great potentials, ESSs increase the capital and operating costs.

Another potential inertia supplier is found to be GCCs. In this case, the energy stored in the DC-link capacitors of GCCs can be used to emulate inertia. The concept of distributed virtual inertia generated by GCCs is proposed with its effectiveness verified in [83]. This method features no change or minimized change of hardware, and hence it is economically attractive. Nevertheless, due to the proportional relationship between grid frequency and DC-link voltages, DC-link voltages are tied to the frequency even after power converters releasing the inertial power for inertia support. As a result, DC-link voltages cannot be restored until the grid frequency goes back to its nominal value. Without voltage recovery, the low DC-link voltages may lead to overmodulation of GCCs when a step-up load change causes another DC-link voltage drop [84]. Moreover, since the DC-link voltage cannot be restored automatically after providing inertial support, GCCs cannot provide inertia support in the face of cascading frequency events.

---

Additionally, the DC-link voltage fluctuations in normal operating conditions of power systems become a concern. Specifically, under normal operating conditions, the power mismatch between generation and demand gives rise to grid frequency fluctuations. Since DC-link voltages are proportionally related to the grid frequency by the virtual inertia control, grid frequency fluctuations will be translated into the DC-link voltage fluctuations, which may further result in inaccurate power regulation [85] and deteriorate the lifetime of the GCC DC-link capacitors.

In view of these concerns, an autonomous DC-link voltage restoration method for GCCs providing virtual inertia support is proposed in this chapter. A high-pass filter (HPF) is cascaded with the virtual inertia block to extract high-frequency components from the grid frequency. Therefore, the virtual inertia control of GCCs has no effect in the quasi-steady state. In other words, DC-link voltages can be restored autonomously after releasing the inertial power, and thus the DC-link voltage fluctuations in normal operating conditions can be suppressed. Moreover, with the automatically restored DC-link voltage, it is possible for GCCs to provide virtual inertia support during cascading frequency events. Finally, simulation and experimental results are presented to verify the effectiveness of the proposed method.

## **2.2. Frequency Instability with the Reduction of Inertia**

### **2.2.1. Frequency Instability Caused by the Lack of Inertia**

Inertia plays a critical role in maintaining frequency stability for power systems, and the lack of inertia may lead to grid-wide frequency instability. The inertia of power system is defined as the per unit kinetic energy stored in rotors of synchronous generators and turbines, which is expressed as

$$H = \frac{E_k}{VA_{base}} = \frac{J\omega_{mn}^2}{2VA_{base}} \quad (2-1)$$

---

in which  $E_k$  signifies the kinetic energy stored in synchronous generators when the rotor is rotating at its rated speed;  $J$  represents the combined moment of inertia of synchronous generators and turbines;  $\omega_{mn}$  is the nominal mechanical angular speed of rotors;  $V_{A_{base}}$  stands for the nominal power of synchronous generators;  $H$  denotes the inertia coefficient, which quantitatively measure the time for the nominal power output of synchronous generators that can be supplied individually by the kinetic energy stored in rotors. It is reported that typical values of  $H$  are 5 s for gas-fired generators, 3.5 s for coal-fired generators, and 3 s for hydraulic generators.

For conventional power systems, which are dominated by synchronous generator-based power generation, synchronous generators with rotating rotors provide inertia for frequency support naturally. Since the rotor speed of synchronous generators are rigidly synchronized with the grid frequency, during a low-frequency event, the rotating speed of synchronous generator rotors will slow down automatically, and the kinetic energy stored in the rotors of synchronous generator will be released consequently to contribute to balancing the mismatch between power generation and power demand immediately, so that the frequency stability of power system can be maintained as a result.

However, things are different for modern power systems with increasing penetration of renewable energies, in which synchronous generators are gradually being replaced by converter-interfaced renewable generators. Different from synchronous generators, power converters, which are embedded with no rotating components, feature zero kinetic energy, and provide no inertia for power grids. Besides, the dynamics of these converter-interfaced renewable generators are decoupled from power grids, as a consequence, even though some kinds of renewable generators, such as wind turbines, have rotors and the associated kinetic energy, the rotor speed of wind turbines are fully isolated from grid-side frequency by power converters for a better tracking of maximum power point and a higher degree of control flexibility. Thus, the rotor speed of wind turbines is tightly regulated to exploit the maximum power and cannot respond to frequency events in grid side. As a result, no inertia can be naturally supplied from the converter-interfaced renewable generation. With the

expectation that the synchronous-generator-based generation is continually substituted by converter-based renewable generation, the total inertia of power system declines.

Fig. 2.1 visualizes the effect of the reduction of inertia on frequency response during a low-frequency event, in which a lower frequency nadir and a higher rate of change of frequency, e.g., RoCoF, are witnessed with the reduction of inertia. In power systems, under-frequency protective relays are commonly equipped to protect generators from mechanically overstress caused by low frequency, and the lower frequency nadir leads to a higher risk of generator tripping. Besides, the anti-islanding protective relays are based on RoCoF levels, and thus the excessive RoCoF caused by the lack of inertia may trigger anti-islanding protections and result in system splitting.

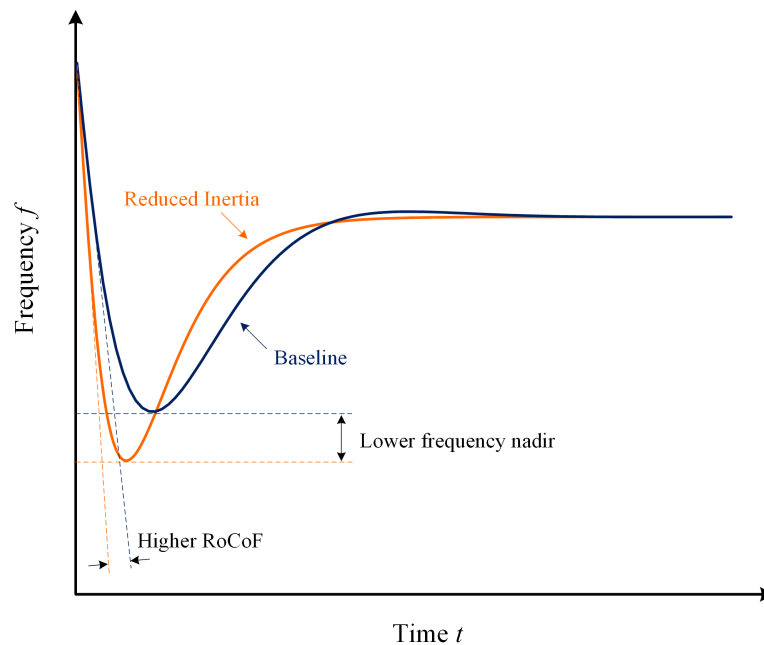


**Figure 2.1** : Effect of inertia in a low-frequency event.

### 2.2.2. Virtual Inertia Provided by GCCs

Different approaches have been developed to enhance inertia and avoid frequency instability in power systems with high penetration of renewable generation. In the following section, the virtual inertia provided by GCCs will be demonstrated. The



simplified structure of a typical power system is illustrated in Fig. 2.2, where  $P_M$  signifies the net shaft power input to the synchronous generators (SGs),  $P_E$  is the electrical air-gap power of SGs, and it is equal to  $(P_D+P_L)$  without considering power converters.  $P_D$  stands for the power consumed by frequency-dependent loads, and  $P_L$  denotes the power absorbed by frequency-independent loads.  $P_{GCC}$  refers to the net power absorption of GCCs, and it is equal to the power consumed by power electronics-coupled loads minus the power generated by renewable generators, such as PV arrays and wind turbines.

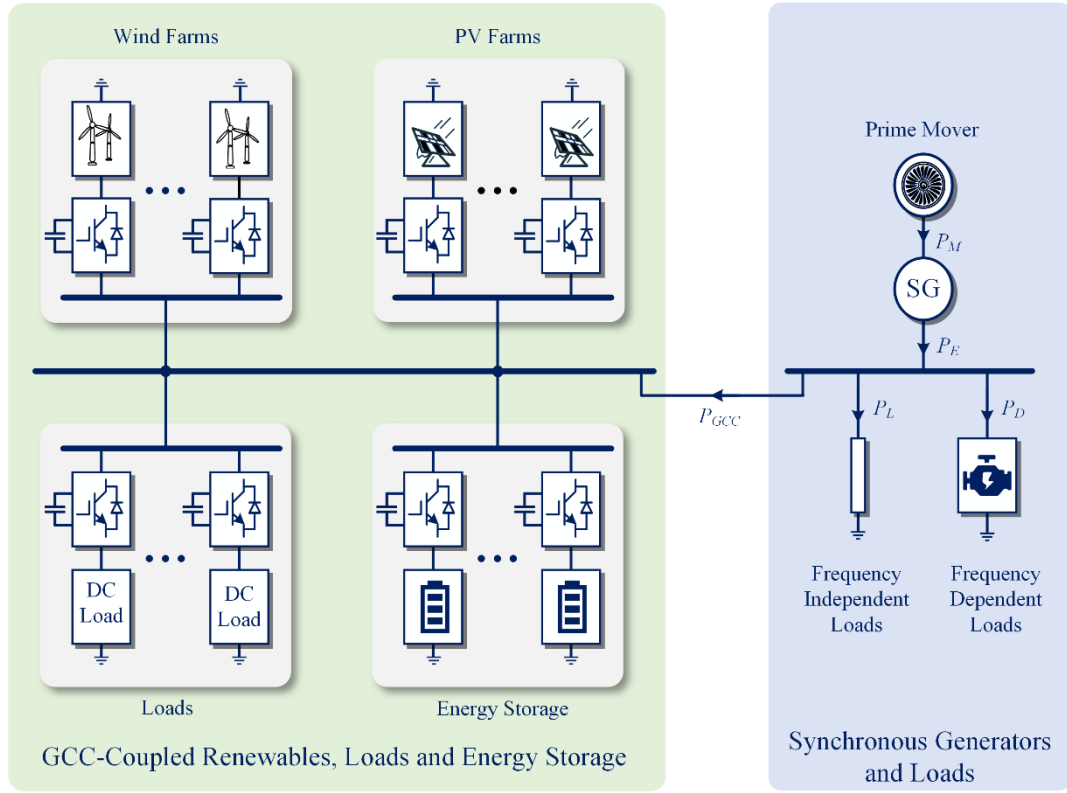


**Figure 2.2:** Simplified structure of a typical power system with power-electronic-coupled components.

Without considering the inertia contributed by GCCs, the dynamic behavior of the power system under small disturbances can be mathematically described by the following swing equation (in per unit notations) [86]:

$$\Delta P_M - \Delta P_E = \Delta P_M - (\Delta P_L + \Delta P_D) = 2H \frac{d\Delta f}{dt} \quad (2-2)$$

where the prefix  $\Delta$  denotes the changes of variables;  $H$  signifies the inertia constant, and the physical meaning of  $2H$  is the time required for rated torque to accelerate the rotor from standstill to rated speed [87];  $f$  represents the grid frequency. In (2-2),  $\Delta P_D$  can be further expressed as  $D\Delta f$ , in which  $D$  is the damping factor.

GCCs are proven to have a great potential for inertia emulation and improvement, as already verified in [83]. For illustration, the schematic of the GCC equipped with the virtual inertia control is shown in Fig. 2.3, where the DC-link capacitor serves as a potential inertia supplier.

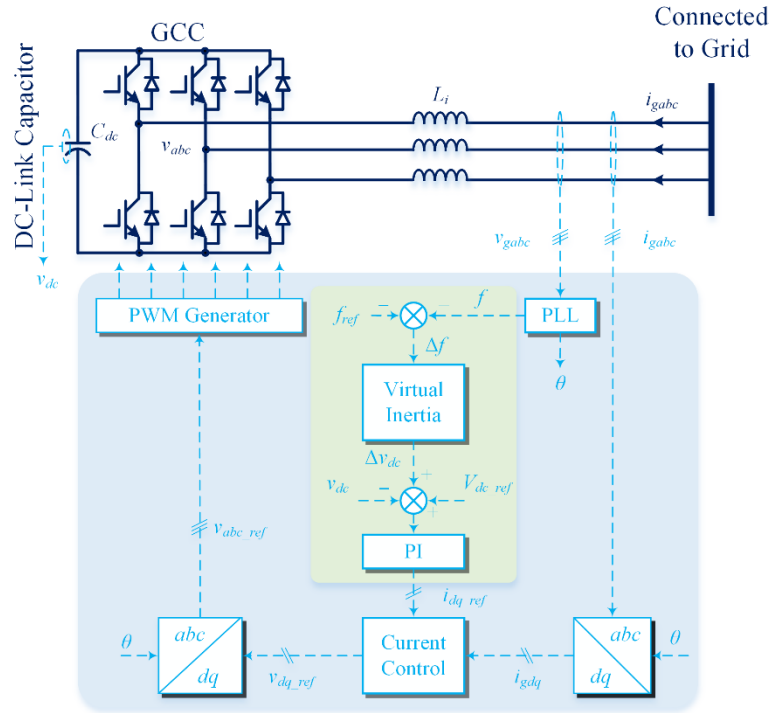


**Figure 2.3:** Schematic of the GCC equipped with the virtual inertia control.

In Fig. 2.3, the three-phase grid voltages  $v_{gabc}$  are measured and synchronized by a PLL, which provides the phase-angle information for grid synchronization and current regulation in the synchronous  $dq$ -frame. The voltage of the DC-link capacitor  $v_{dc}$  can be controlled to its reference value  $V_{dc\_ref}$  by changing the  $d$ -axis current reference  $i_{d\_ref}$ . The virtual inertia control block allowing the inertia emulation is introduced. It directly links the grid

frequency to the DC-link voltage so that the DC-link capacitor can absorb or release energy when the grid frequency deviates from its nominal value. Taking the effect of the virtual inertia from GCCs into consideration, the swing equation in (2-2) is modified as

$$\Delta P_M - \Delta P_L - D \cdot \Delta f - \Delta P_{GCC} = 2H \frac{d\Delta f}{dt} \quad (2-3)$$

In (2-3),  $\Delta P_{GCC}$  denotes the inertial power provided by GCCs, and it can be expressed as

$$\begin{aligned} \Delta P_{GCC} &= \frac{d\Delta E_C}{dt} = \frac{d}{dt} \left[ \frac{1}{2} C_{dc} V_{dc\_ref}^2 - \frac{1}{2} C_{dc} (V_{dc\_ref} - \Delta v_{dc})^2 \right] \\ &= C_{dc} V_{dc\_ref} \frac{d\Delta v_{dc}}{dt} \end{aligned} \quad (2-4)$$

where  $\Delta E_C$  is the energy change of the DC-link capacitor due to the change of the DC-link voltage;  $V_{dc\_ref}$  represents the rated DC-link voltage;  $\Delta v_{dc}$  denotes the change of the DC-link voltage.

Upon normalizing, (2-4) becomes

$$\begin{aligned} \Delta P_{GCC\_pu} &= \frac{C_{dc} \cdot V_{dc\_ref}}{VA_{rated}} \cdot V_{dc\_ref} \cdot \frac{d}{dt} (\Delta v_{dc} / V_{dc\_ref}) \\ &= \frac{C_{dc} \cdot V_{dc\_ref}^2}{VA_{rated}} \cdot \frac{d\Delta v_{dc\_pu}}{dt} \\ &= 2H_c \cdot \frac{d\Delta v_{dc\_pu}}{dt} \end{aligned} \quad (2-5)$$

where  $VA_{rated}$  is the rated power of the GCC. In (2-5), the inertia constant of DC-link capacitors is defined as

$$H_c = \frac{C_{dc} \cdot V_{dc\_ref}^2}{2VA_{rated}} \quad (2-6)$$

In [83], the virtual inertia block was designed to be a proportional controller relating the DC-link voltage to the grid frequency through a gain  $K_{fv}$ , which can be expressed as

$$K_{fv} = \frac{\Delta V_{dc\_max}}{\Delta f_{max}} \quad (2-7)$$

where  $\Delta V_{dc\_max}$  and  $\Delta f_{max}$  are the maximum DC-link voltage variation and the maximum grid frequency change, respectively. Through this method, the energy stored in the DC-link capacitors of GCCs can be exploited to emulate inertia, and the corresponding equivalent inertia constant or virtual inertia constant can be derived as

$$H_{vi} = \frac{C_{dc} \cdot V_{dc\_ref}^2}{2VA_{rated}} \cdot \frac{\Delta V_{dc\_max}}{\Delta f_{max}} \quad (2-8)$$

It is revealed in (2-8) that when the virtual inertia control is included, the GCC can provide inertia support during frequency contingencies. As a result, the equivalent inertia constant of the power system shown in Fig. 2.2 will increase from  $H$  to  $(H + H_{vi})$ .

### 2.3. Autonomous DC-Link Voltage Restoration for GCCs Providing Virtual Inertia

To restore the DC-link voltages of GCCs after releasing their inertial power during frequency events, a HPF-based method is proposed in this chapter, and the HPF is incorporated and cascaded with the proportional controller  $K_{fv}$  in the virtual inertia control block. For demonstration, the block diagram of the frequency regulation architecture including the proposed HPF is detailed in Fig. 2.4, in which  $T_G$  represents the speed governor coefficient,  $T_{CH}$  denotes the time constant of the main inlet volume,  $T_{RH}$  stands for the time constant of the reheater,  $F_{HP}$  is the turbine HP coefficient, and  $R$  is the droop coefficient [86]. As shown in Fig. 2.4, high-frequency components of the grid frequency will be extracted by the HPF for inertia emulation during frequency events. Then, the filtered grid frequency change will be transformed into the DC-link voltage deviation  $\Delta V_{dc}$ , which will further regulate GCCs to output more power  $\Delta P_{GCC}$  for frequency support in face of disturbance.

When power systems operate normally or restore from frequency events, the grid frequency will reach its quasi-steady state. Under these conditions, the output of the HPF will be zero. Therefore, the grid frequency and the DC-link voltage will be decoupled by the HPF, and

the inertia emulation function of GCCs will be disabled. As a result, the DC-link capacitor can achieve voltage restoration and prepare itself for another frequency event.

Since the HPF shown in Fig. 2.4 plays a decisive role on the inertia supportability of GCCs and the restoration time of DC-link voltages, as will be revealed in the following sections, special attention should be paid to the design of the HPF. Its transfer function can be expressed as

$$G_{h\_pass}(s) = \frac{s}{s + 2\pi f_{cut}} \quad (2-9)$$

where  $f_{cut}$  denotes the cut-off frequency of the HPF, and it determines the dynamics of DC-link voltages under frequency events.

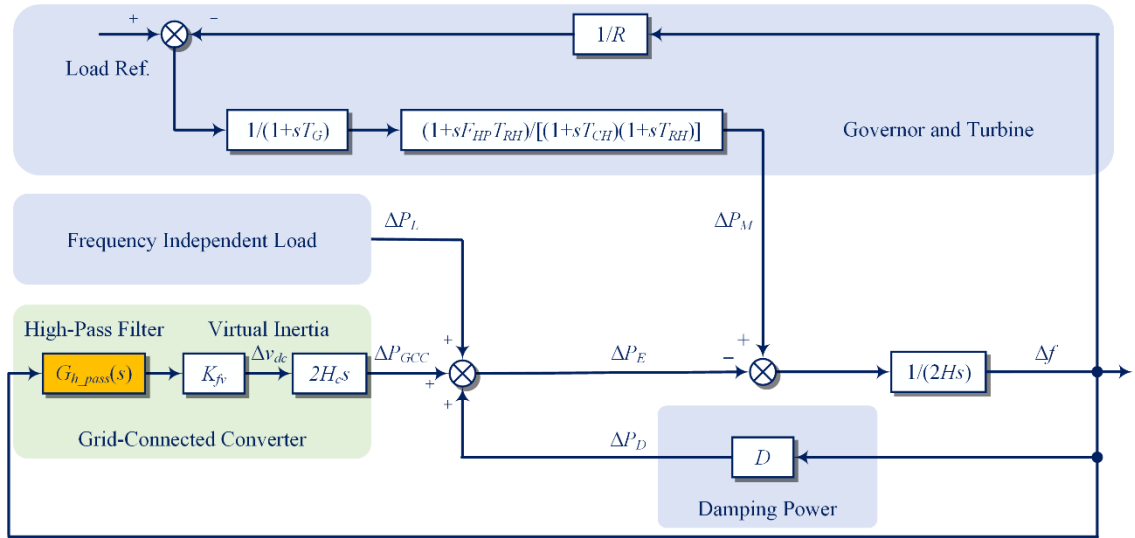


**Figure 2.4:** Block diagram of the frequency regulation architecture including the proposed DC-link voltage restoration block.

### 2.3.1. Effect of the HPF on the Inertial Supportability of GCCs

Based on the control system shown in Fig. 2.4, the transfer function from the power deviation  $\Delta P_L$  to the grid frequency deviation  $\Delta f$ , e.g.,  $G_{PL \rightarrow f}(s)$ , can be derived as

$$\begin{aligned}
G_{PL \rightarrow f}(s) &= \frac{\Delta f}{\Delta P_L} \\
&= \frac{-R(1+T_G s)(1+T_{CH} s)(1+T_{RH} s)(s+2\pi f_{cut})}{\left\{ R(1+T_G s)(1+T_{CH} s)(1+T_{RH} s) \left[ 2H_c K_{fv} s^2 + (2Hs + D)(s+2\pi f_{cut}) \right] \right\} + (1+F_{HP} T_{RH} s)(s+2\pi f_{cut})} \quad (2-10)
\end{aligned}$$

According to [83, 88], due to small time constants of speed governor and main inlet volume, the poles associated with  $T_G$  and  $T_{CH}$  have a minor influence on the system dynamics, and hence they can be ignored to simplify analysis. Therefore, the original transfer function  $G_{PL \rightarrow f}(s)$  denoted by (2-10) can be simplified to a third-order equation, expressed as

$$\begin{aligned}
G_{PL \rightarrow f}(s) &= \frac{\Delta f}{\Delta P_L} = \frac{-R(1+T_{RH} s)(s+2\pi f_{cut})}{\left\{ R(1+T_{RH} s) \left[ 2H_c K_{fv} s^2 + (2Hs + D)(s+2\pi f_{cut}) \right] \right\} + (1+F_{HP} T_{RH} s)(s+2\pi f_{cut})} \\
&= \frac{-R(1+T_{RH} s)}{R(1+T_{RH} s) \left( \frac{2H_c K_{fv} s + 2Hs + D}{s + 2\pi f_{cut}} \right) + F_{HP} T_{RH} s + 1} \quad (2-11)
\end{aligned}$$

To investigate the worst stability case, the impact of the damping coefficient  $D$  in (2-11) is ignored as claimed in [87, 89]. Thus,  $G_{PL \rightarrow f}(s)$  expressed in (2-11) can be further simplified to a second-order equation, expressed as

$$\begin{aligned}
G_{PL \rightarrow f}(s) &= \frac{\Delta f}{\Delta P_L} = \frac{-R(1+T_{RH} s)}{R(1+T_{RH} s) \left[ (2H + 2H_c K_{fv}) s - 2H_c K_{fv} \cdot 2\pi f_{cut} \right] + F_{HP} T_{RH} s + 1} \\
&= \frac{-R(1+T_{RH} s)}{\left\{ RT_{RH} (2H + 2H_c K_{fv}) s^2 + \left( 2HR + 2H_c K_{fv} R - 2T_{RH} H_c K_{fv} R \cdot 2\pi f_{cut} + F_{HP} T_{RH} \right) s \right\} + (1 - 2H_c K_{fv} R \cdot 2\pi f_{cut})} \quad (2-12) \\
&= G_0 \frac{s + z_1}{s^2 + 2\zeta \omega_n s + \omega_n^2}
\end{aligned}$$

where

$$G_0 = \frac{-1}{2H + 2H_c K_{fv}}, \quad z_1 = \frac{1}{T_{RH}}, \quad \omega_n = \sqrt{\frac{1 - 2H_c K_{fv} R \cdot 2\pi f_{cut}}{RT_{RH}(2H + 2H_c K_{fv})}}, \quad (2-13)$$

$$\zeta = \frac{(2HR + 2H_c K_{fv} R - 2T_{RH} H_c K_{fv} R \cdot 2\pi f_{cut} + F_{HP} T_{RH})}{2RT_{RH}(2H + 2H_c K_{fv})} \sqrt{\frac{RT_{RH}(2H + 2H_c K_{fv})}{1 - 2H_c K_{fv} R \cdot 2\pi f_{cut}}}$$

The comparisons between  $G_{PL \rightarrow f}(s)$  expressed in (2-10) and its simplified second-order form represented in (2-12) are shown in Fig. 2.5. Based on the pole-zero map shown in Fig. 2.5(a), it is seen that for the original transfer function expressed in (2-10),  $P_3$  and  $Z_2$  nearly overlap. Besides, the imaginary parts of  $P_4$ ,  $P_5$ ,  $Z_3$ , and  $Z_4$  are much less than those of  $P_1$ ,  $P_2$  and  $Z_1$ . Therefore, the influence of poles  $P_3$ ,  $P_4$ ,  $P_5$  and zeros  $Z_2$ ,  $Z_3$ ,  $Z_4$  on the dynamic responses of  $G_{PL \rightarrow f}(s)$  can be ignored, and the original transfer function in (2-10) can be simplified to a second-order equation characterized by  $P_1$ ,  $P_2$  and  $Z_1$ , denoted by (2-12).

According to the comparisons of step responses shown in Fig. 2.5(b), although the frequency nadir of (2-12) is slightly lower than that of the original transfer function (2-10) due to the removal of the damping coefficient  $D$ , the maximum difference of the frequency responses between these two cases is less than 5% of the maximum frequency deviations. Therefore, the effectiveness of the proposed simplified model is validated.

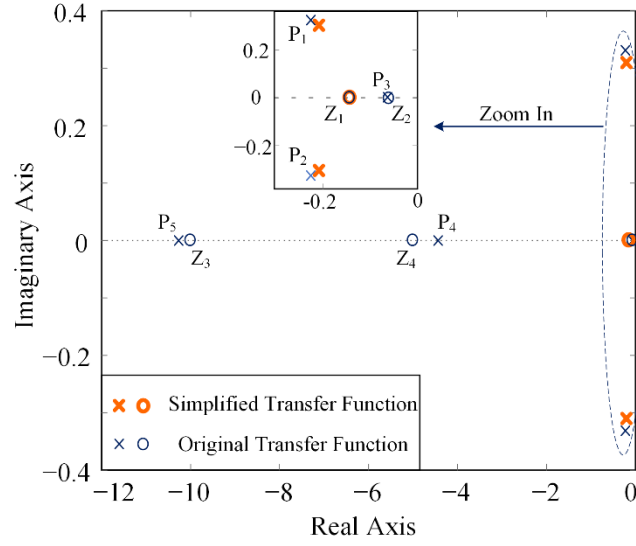
Considering a step-up load change, the grid frequency can be expressed in the  $s$  domain as

$$f(s) = f_{ref}(s) + \Delta f(s) = \frac{1}{s} + G_{PL \rightarrow f}(s) \cdot \frac{1}{s}$$

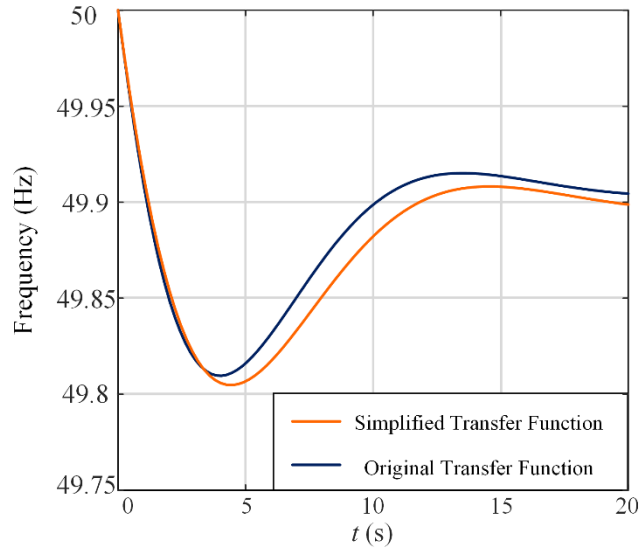
$$= \frac{1}{s} + G_0 \left\{ \frac{1}{\omega_d} \cdot \frac{\omega_d}{(s + \zeta\omega_n)^2 + \omega_d^2} + \frac{z_1}{\omega_n^2} \left[ \frac{1}{s} - \frac{s + \zeta\omega_n}{(s + \zeta\omega_n)^2 + \omega_d^2} - \frac{\zeta\omega_n}{\omega_d} \cdot \frac{\omega_d}{(s + \zeta\omega_n)^2 + \omega_d^2} \right] \right\} \quad (2-14)$$

where  $f_{ref}(s) = 1/s$  is the per-unit reference signal,  $\Delta f(s) = G_{PL \rightarrow f}(s)/s$  denotes the frequency deviation.  $\omega_d$  stands for the damped frequency, which is expressed as

$$\omega_d = \omega_n \sqrt{1 - \zeta^2} \quad (2-15)$$



(a)



(b)

**Figure 2.5:** Comparisons between  $G_{PL \rightarrow f}(s)$  and its simplified second-order form. (a) Pole-zero map. (b) Frequency response under 4% step-up load change.

By taking the inverse Laplace transform of (2-14), the expression of the grid frequency in the time domain can be derived as

$$f(t) = 1 + G_0 \frac{z_1}{\omega_n^2} - G_0 e^{-\zeta \omega_n t} A_1 \sin(\omega_d t + \phi) \quad (2-16)$$

where



$$A_1 = \sqrt{\left(\frac{z_1}{\omega_n^2}\right)^2 + \left(\frac{-z_1\zeta + \omega_n}{\omega_n\omega_d}\right)^2}, \quad \phi = \arctan\left[\frac{\omega_d z_1}{(z_1\zeta - \omega_n)\omega_n}\right] \quad (2-17)$$

Based on (2-16)), some important dynamic performance indices can be derived. The RoCoF is obtained by differentiating the expression of grid frequency  $f(t)$  in (2-16) with respect to time  $t$  as

$$\begin{aligned} \text{RoCoF} &= \frac{d}{dt} f(t) \\ &= G_0 \left[ \zeta \omega_n e^{-\zeta \omega_n t} A_1 \sin(\omega_d t + \phi) - e^{-\zeta \omega_n t} A_1 \omega_d \cos(\omega_d t + \phi) \right] \end{aligned} \quad (2-18)$$

By setting (2-18) equal to zero, the time of grid frequency reaching the frequency nadir, e.g.,  $t_{nadir}$ , can be derived as

$$t_{nadir} = \frac{1}{\omega_d} \cdot \left[ \arctan\left(\frac{\sqrt{1-\zeta^2}}{\zeta}\right) - \phi + \pi \right] \quad (2-19)$$

Taking (2-19) into (2-16), the frequency nadir  $f_{nadir}$  can be obtained as

$$f_{nadir} = 1 + \frac{G_0 z_1}{\omega_n^2} + G_0 e^{-\zeta \omega_n t_{nadir}} A_1 \sqrt{1-\zeta^2} \quad (2-20)$$

Based on (2-18) and (2-20), the relationships between the cut-off frequency  $f_{cut}$  and the RoCoF, overshoot  $\sigma$ , frequency nadir  $f_{nadir}$ , and settling time  $t_s$  are demonstrated in Fig. 2.6, respectively. As illustrated in Fig. 2.6 (a) and (b), the change of  $f_{cut}$  has little influence on the RoCoF and overshoot  $\sigma$  at the start of frequency events. However, as shown in Fig. 2.6 (c) and (d), with the increase of  $f_{cut}$ , the frequency nadir  $f_{nadir}$  decreases, while the settling time  $t_s$  increases. This indicates that the inertia supportability of GCCs declines with the increases of  $f_{cut}$ , and it will take a longer time for the system to reach steady state. This fact can be explained by the characteristics of the HPF. With a larger  $f_{cut}$ , fewer high-frequency components of the grid frequency deviation can pass the HPF. Due to the proportional controller inside the virtual inertia block, the inertial power exported from GCCs reduces as well, and thus leading to a lower frequency nadir.

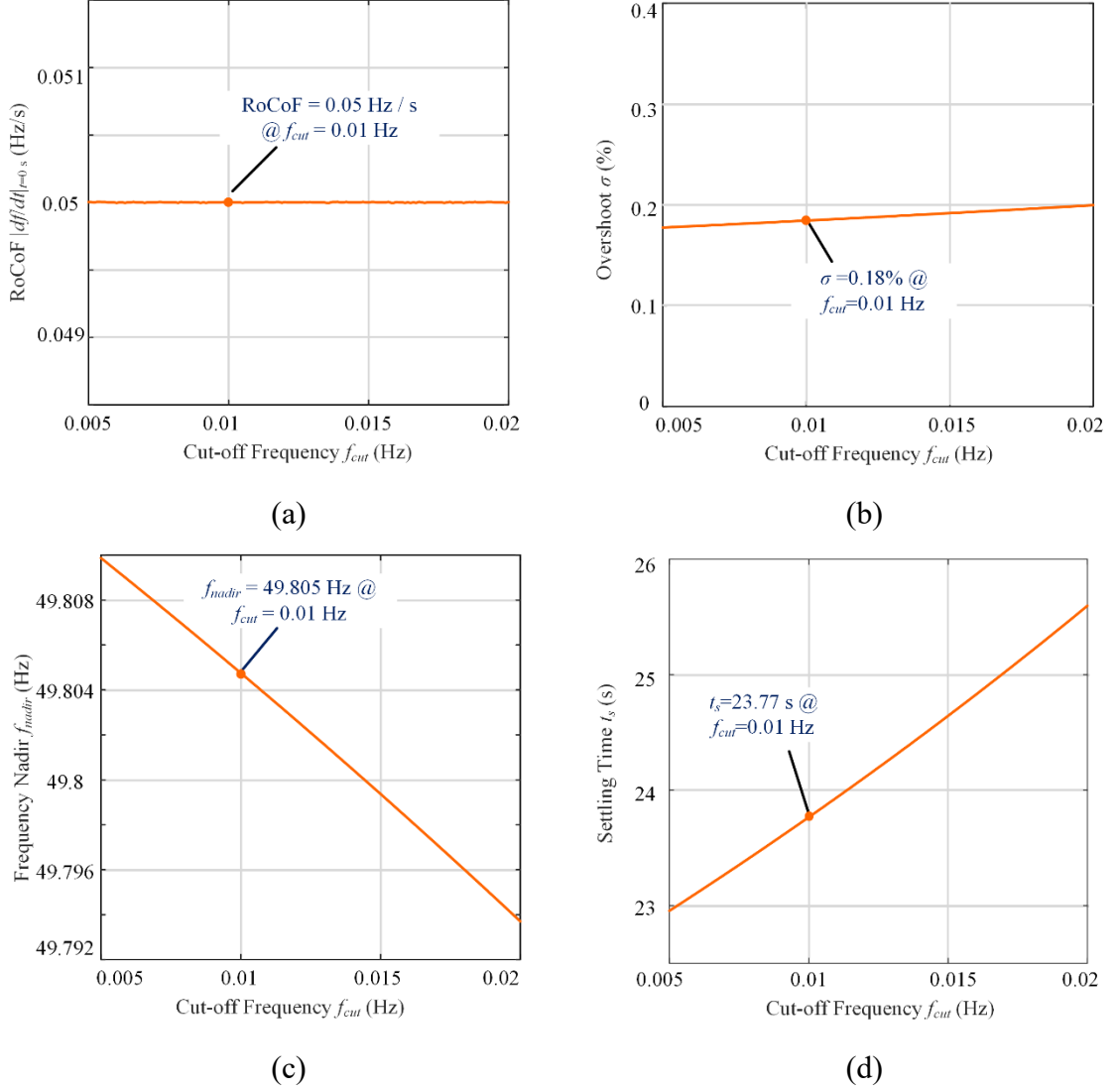


**Figure 2.6:** Relationships between the dynamic performance indices and the value of the cut-off frequency  $f_{cut}$ . (a) RoCoF  $|df/dt|_{t=0s}$ . (b) Overshoot  $\sigma$ . (c) Frequency nadir  $f_{nadir}$ . (d) Settling time  $t_s$ .

To quantify the influence of the HPF on the inertial supportability of GCCs, an index  $\mu$  is defined as

$$\begin{aligned} \mu &= \frac{(f_{ref} - f_{nadir}) - (f_{ref} - f_{nadir\_BM})}{(f_{ref} - f_{nadir\_BM})} \times 100\% \\ &= \frac{f_{nadir\_BM} - f_{nadir}}{f_{ref} - f_{nadir\_BM}} \times 100\% \end{aligned} \quad (2-21)$$

where  $f_{ref}$  is the nominal frequency of power systems.  $f_{nadir\_BM}$  signifies the frequency nadir during frequency events in the benchmark case without the HPF.  $f_{nadir}$  denotes the frequency nadir in the case with the proposed HPF, which is represented in (2-20). To limit the adverse impact of the HPF on the inertia supportability of GCCs,  $\mu$  should be less than 10%.

**Table 2.1:** System parameter values.

Symbol	Description	Value
$T_G$	Speed governor coefficient	0.1 s
$T_{CH}$	Time constant of main inlet volumes	0.2 s
$T_{RH}$	Time constant of reheater	7.0 s
$F_{HP}$	Turbine HP coefficient	0.3 s
$R$	Droop coefficient	0.05
$H$	Inertia coefficient of SG	5.0 s
$D$	Damping coefficient	1.0
$K_{fv}$	Proportional gain	22.5
$V_{dc}$	Rated DC-link voltage	400 V
$\Delta V_{dc\_max}$	Maximum DC-link voltage deviation	36 V
$C_{dc}$	DC-link capacitance	2.82 mF
$\Delta f_{max}$	Maximum frequency deviation	0.2 Hz
$VA_{rated}$	Power rating	1000 kVA

Based on (2-21), the relationship between  $f_{cut}$  of the HPF and the index  $\mu$  is obtained, as shown in Fig. 2.7, where the system parameters are listed in Table. 2.1. It can be obtained from Fig. 2.7 that to satisfy the requirement of  $\mu < 10\%$ ,  $f_{cut}$  should be less than 0.0125 Hz, as shown in the shaded area of Fig. 2.7.

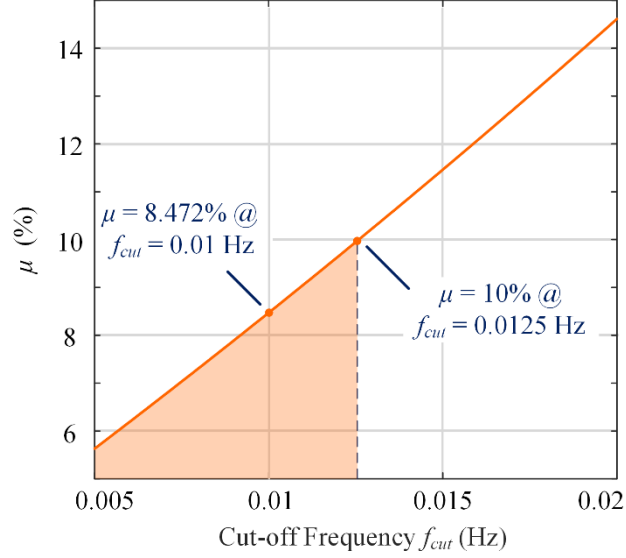


**Figure 2.7:** Relationship between  $f_{cut}$  and the index  $\mu$ .

### 2.3.2. Impact of Cut-Off Frequency on DC Voltage Restoration Time

Based on Fig. 2.4, the transfer function from the power deviation  $\Delta P_L$  to the DC-link voltage deviation  $\Delta V_{dc}$ , e.g.,  $G_{PL \rightarrow V_{dc}}(s)$ , is derived as

$$\begin{aligned}
 G_{PL \rightarrow V_{dc}}(s) &= \frac{\Delta V_{dc}}{\Delta P_L} = \frac{\Delta V_{dc}}{\Delta f} \cdot \frac{\Delta f}{\Delta P_L} \\
 &= K_{fv} \cdot \frac{s}{s + 2\pi f_{cut}} \cdot G_{PL \rightarrow f}(s)
 \end{aligned} \tag{2-22}$$

By substituting  $G_{PL \rightarrow f}(s)$  expressed in (2-10) into (2-22),  $G_{PL \rightarrow V_{dc}}(s)$  can be derived as

$$\begin{aligned}
 G_{PL \rightarrow V_{dc}}(s) &= \frac{\Delta V_{dc}}{\Delta P_L} \\
 &= \frac{-K_{fv} R (1 + T_G s) (1 + T_{CH} s) (1 + T_{RH} s) (s + 2\pi f_{cut}) \cdot s}{\left\{ R (1 + T_G s) (1 + T_{CH} s) (1 + T_{RH} s) [(2H + 2H_c K_{fv}) s^2 \right.} \\
 &\quad \left. + 2H \cdot 2\pi f_{cut} s + D] + (1 + F_{HP} T_{RH} s) (s + 2\pi f_{cut}) \right\}}
 \end{aligned} \tag{2-23}$$

In (2-23),  $G_{PL \rightarrow V_{dc}}(s)$  is a fifth-order equation, which is too complex to analyze its dynamic characteristics. By substituting the simplified form of  $G_{PL \rightarrow f}(s)$  expressed in (2-12) into (2-22), the simplified form of  $G_{PL \rightarrow V_{dc}}(s)$  in (2-23) is derived as

$$\begin{aligned}
 G_{PL \rightarrow V_{dc}}(s) &= \frac{\Delta V_{dc}}{\Delta P_L} \\
 &= G_0 \frac{s + z_1}{s^2 + 2\zeta\omega_n s + \omega_n^2} \cdot K_{fv} \frac{s}{(s + 2\pi f_{cut})} \\
 &= G_0 K_{fv} \frac{(s + z_1)s}{(s^2 + 2\zeta\omega_n s + \omega_n^2)(s + 2\pi f_{cut})}
 \end{aligned} \tag{2-24}$$

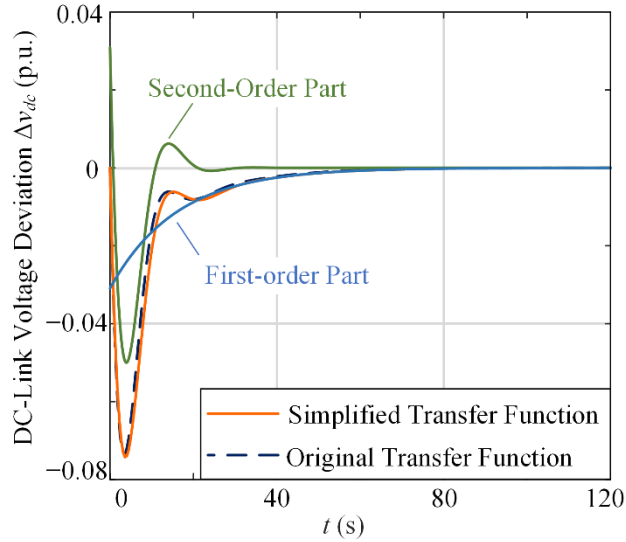


**Figure 2.8:** DC-link voltage responses (under a 4% step-up load change).

The comparisons between the step responses of  $G_{PL \rightarrow V_{dc}}(s)$  expressed in (2-23) and its simplified form represented in (2-24) are depicted in Fig. 2.8. It can be seen from Fig. 2.8 that the differences between these two cases are always less than 5% DC-link voltage deviations, and thus the effectiveness of the simplified form of  $G_{PL \rightarrow V_{dc}}(s)$  expressed in (2-24) is verified.

Considering a step-up load change, the DC-link voltage deviation  $\Delta V_{dc}(s)$  in the  $s$  domain is expressed as

$$\begin{aligned}
\Delta V_{dc}(s) &= G_{PL \rightarrow V_{dc}}(s) \cdot \frac{1}{s} \\
&= G_0 K_{fv} \frac{(s + z_1)}{(s^2 + 2\zeta\omega_n s + \omega_n^2)(s + 2\pi f_{cut})} \\
&= G_0 K_{fv} \left[ \frac{a_1 s + a_2}{(s + \zeta\omega_n)^2 + \omega_d^2} + \frac{a_3}{s + 2\pi f_{cut}} \right] \\
&= G_0 K_{fv} \left[ a_1 \cdot \frac{s + \zeta\omega_n}{(s + \zeta\omega_n)^2 + \omega_d^2} + \frac{a_2 - a_1 \zeta\omega_n}{\omega_d} \cdot \frac{\omega_d}{(s + \zeta\omega_n)^2 + \omega_d^2} \right. \\
&\quad \left. + a_3 \cdot \frac{1}{s + 2\pi f_{cut}} \right]
\end{aligned} \tag{2-25}$$

where

$$\begin{aligned}
a_1 &= \frac{z_1 - 2\pi f_{cut}}{(2\pi f_{cut})^2 - 2\zeta\omega_n \cdot 2\pi f_{cut} + \omega_n^2}, \quad a_2 = \frac{\omega_n^2 - 2\zeta\omega_n z_1 + 2\pi f_{cut} z_1}{(2\pi f_{cut})^2 - 2\zeta\omega_n \cdot 2\pi f_{cut} + \omega_n^2}, \\
a_3 &= \frac{2\pi f_{cut} - z_1}{(2\pi f_{cut})^2 - 2\zeta\omega_n \cdot 2\pi f_{cut} + \omega_n^2}
\end{aligned} \tag{2-26}$$

By taking the inverse Laplace transform of (2-25), the expression of the DC-link voltage deviation in the time domain is derived as

$$\begin{aligned}
\Delta V_{dc}(t) &= G_0 K_{fv} \left[ a_1 \cdot e^{-\zeta\omega_n t} \cos(\omega_d t) + \frac{a_2 - a_1 \zeta\omega_n}{\omega_d} \cdot e^{-\zeta\omega_n t} \sin(\omega_d t) + a_3 \cdot e^{-2\pi f_{cut} t} \right] \\
&= G_0 K_{fv} \left[ A_2 \sin(\omega_d t + \gamma) \cdot e^{-\zeta\omega_n t} + a_3 \cdot e^{-2\pi f_{cut} t} \right] \\
&= \Delta V_{dc\_2-order}(t) + \Delta V_{dc\_1-order}(t)
\end{aligned} \tag{2-27}$$

where

$$A_2 = \sqrt{a_1^2 + \left( \frac{a_2 - a_1 \zeta\omega_n}{\omega_d} \right)^2}, \quad \gamma = \arctan \frac{a_1 \omega_d}{a_2 - a_1 \zeta\omega_n} \tag{2-28}$$

As reflected by (2-27),  $\Delta V_{dc}(t)$  consists of two parts, i.e., a second-order part  $\Delta V_{dc\_2-order}(t)$  and a first-order part  $\Delta V_{dc\_1-order}(t)$ , which are expressed as the following, respectively:

$$\begin{cases} \Delta V_{dc\_2-order}(t) = G_0 K_{fv} \cdot A_2 \sin(\omega_d t + \gamma) \cdot e^{-\zeta\omega_n t} \\ \Delta V_{dc\_1-order}(t) = G_0 K_{fv} \cdot a_3 \cdot e^{-2\pi f_{cut} t} \end{cases} \tag{2-29}$$

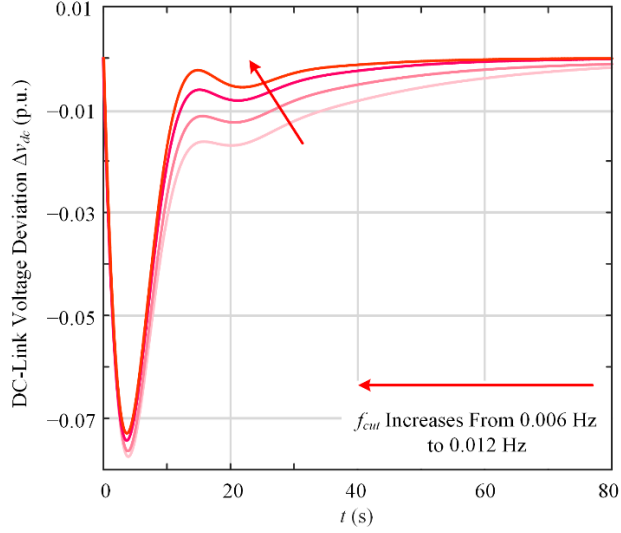
---

The responses of  $\Delta V_{dc\_2-order}(t)$  and  $\Delta V_{dc\_1-order}(t)$  under a 4% step-up load change are also shown in Fig. 2.8. It can be seen from Fig. 2.8 that the curve of  $\Delta V_{dc}(t)$  is the combination of the curves of  $\Delta V_{dc\_2-order}(t)$  and  $\Delta V_{dc\_1-order}(t)$ . With different  $f_{cut}$ , the step responses of  $\Delta V_{dc}(t)$  are shown in Fig. 2.9(a), and the step responses of  $\Delta V_{dc\_2-order}(t)$  and  $\Delta V_{dc\_1-order}(t)$  are shown in Fig. 2.9(b).

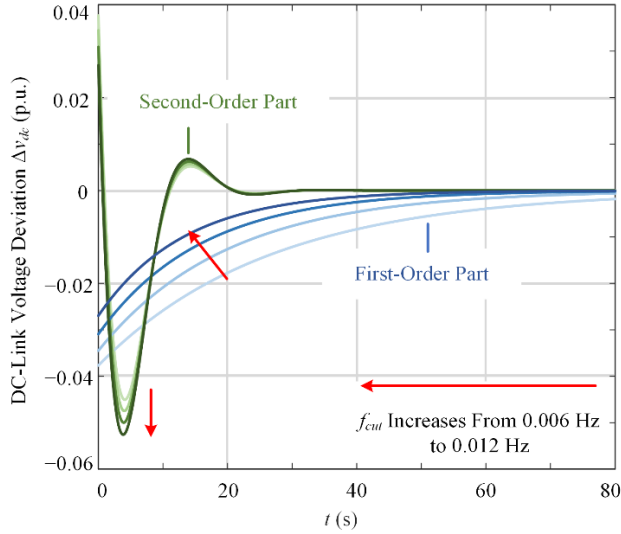
Regarding the DC-link voltage restoration after inertia support, the restoration time is a key factor to be considered when designing the cut-off frequency  $f_{cut}$  of the HPF. In this chapter, the restoration time  $t_{res}$  of the DC-link voltage is defined to be the time for the DC-link voltage to reach 99% of its nominal voltage, and  $t_{res}$  should not be too large to interfere with the subsequent frequency control actions.

As reported in [86], there are three-fold control layers in power systems to keep the frequency stable. The primary frequency control aims to arrest the fast frequency deviation, and its response time ranges from 10 to 60 s [90]. Since the inertial response from generators and GCCs belongs to the primary frequency control, the DC-link voltage restoration should be completed within the primary frequency control response time. In [91], the restoration time of rotor speeds of wind turbines is set to be 30 s. Following this design, the DC-link voltage restoration time  $t_{res}$  is designed to be 10 to 30 s in this chapter.

From Fig. 2.9(a), it can be observed that with the increase of  $f_{cut}$ , it takes less time for the DC-link voltage deviation  $\Delta V_{dc}(t)$  to reach zero. This is reasonable from the perspective of the HPF, because fewer high-frequency components of the grid frequency signal can pass the HPF with a larger  $f_{cut}$ . Correspondingly, the reference of the DC-link voltage deviation  $\Delta V_{dc}$  declines to zero more quickly, and the restoration time will be reduced.



(a)



(b)

**Figure 2.9:** Step responses of  $\Delta V_{dc}(t)$ ,  $\Delta V_{dc\_2-order}(t)$  and  $\Delta V_{dc\_1-order}(t)$  as a function of  $f_{cut}$ . (a)  $\Delta V_{dc}(t)$ . (b)  $\Delta V_{dc\_2-order}(t)$  and  $\Delta V_{dc\_1-order}(t)$ .

It is noted from Fig. 2.9(b) that the change of  $f_{cut}$  has significant influence on  $\Delta V_{dc\_1-order}(t)$ , and the time for  $\Delta V_{dc\_1-order}(t)$  to reach its quasi-steady-state reduces considerably with the increase of  $f_{cut}$ . While the impact of  $f_{cut}$  on  $\Delta V_{dc\_2-order}(t)$  is very limited, and the change of  $f_{cut}$  only has a negligible influence on the nadir of  $\Delta V_{dc\_2-order}(t)$ . Furthermore,  $\Delta V_{dc\_2-order}(t)$  reaches its quasi-steady-state much more quickly than  $\Delta V_{dc\_1-order}(t)$  does. Thus, the



restoration time of the DC-link voltage  $t_{res}$  is mainly determined by  $\Delta V_{dc\_1-order}(t)$ . Therefore, the restoration time  $t_{res}$  can be estimated and calculated from  $\Delta V_{dc\_1-order}(t)$  as

$$\Delta V_{dc\_1-order}(t) = G_0 K_{fv} \cdot a_3 \cdot e^{-2\pi f_{cut} t} = -0.01 \Rightarrow t_{res} \approx -\frac{1}{2\pi f_{cut}} \cdot \ln\left(\frac{-0.01}{G_0 K_{fv} \cdot a_3}\right) \quad (2-30)$$

Based on (2-30) and system parameters shown in Table 2.1, the relationship between  $t_{res}$  and  $f_{cut}$  under a 4% step-up load change is depicted in Fig. 2.10. It can be obtained from Fig. 2.10 that  $f_{cut}$  should be within the range from 0.00685 to 0.01360 Hz to meet the requirement of  $10 \text{ s} < t_{res} < 30 \text{ s}$ , as shown in the shaded area of Fig. 2.10.

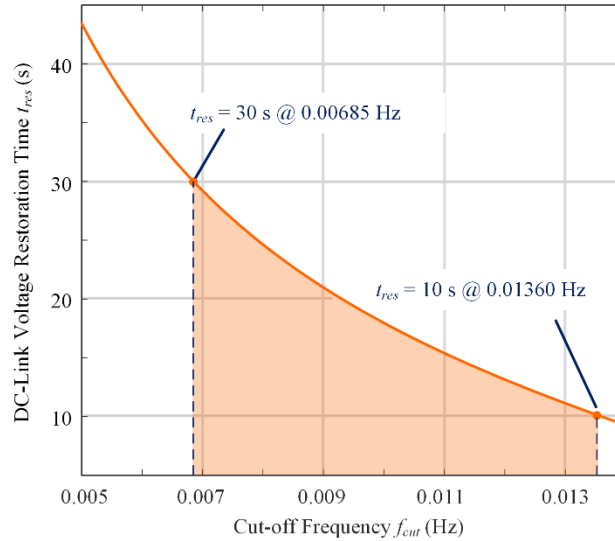
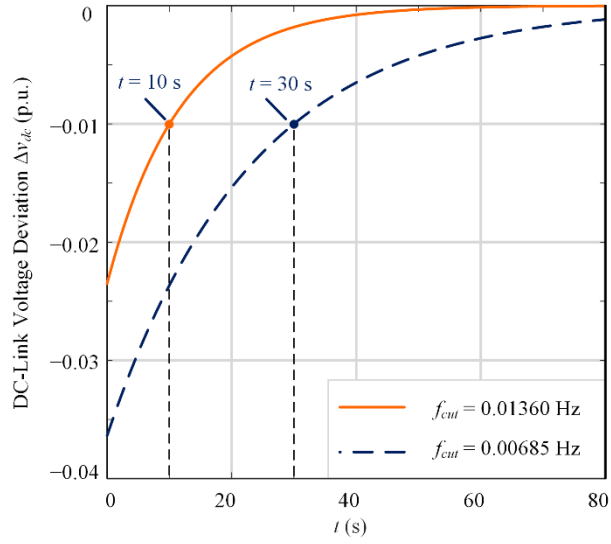
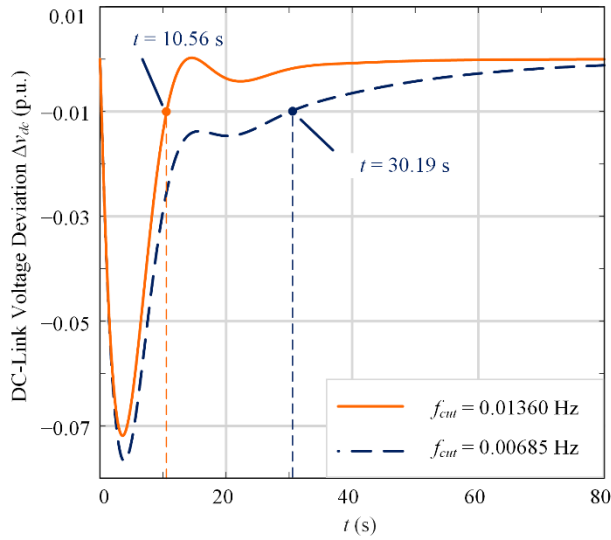


**Figure 2.10:** Relationship between the DC-link voltage restoration time  $t_{res}$  and the cut-off frequency  $f_{cut}$ .

The responses of  $\Delta V_{dc}(t)$  and  $\Delta V_{dc\_1-order}(t)$  with  $f_{cut} = 0.00685 \text{ Hz}$  and  $f_{cut} = 0.01360 \text{ Hz}$  under a 4% step-up load change are shown in Fig. 2.11, respectively. It can be observed from Fig. 2.11 that when  $f_{cut} = 0.00685 \text{ Hz}$ ,  $t_{res} = 30 \text{ s}$  in term of  $\Delta V_{dc\_1-order}(t)$ , and in the case of  $\Delta V_{dc}(t)$ ,  $t_{res} = 30.19 \text{ s}$ ; when  $f_{cut} = 0.01360 \text{ Hz}$ ,  $t_{res} = 10 \text{ s}$  in the case of  $\Delta V_{dc\_1-order}(t)$ , and  $t_{res} = 10.56 \text{ s}$  in the case of  $\Delta V_{dc}(t)$ . The differences between the restoration times estimated and calculated based on  $\Delta V_{dc\_1-order}(t)$  and the exact restoration times of  $\Delta V_{dc}(t)$  are very small. Hence, it is accurate enough to calculate  $t_{res}$  of  $\Delta V_{dc}(t)$  according to (2-30).



(a)



(b)

**Figure 2.11:** Restoration times  $t_{res}$  of the 1-order subsystem  $\Delta V_{dc\_1-order}(t)$  and the DC-link voltage deviation  $\Delta V_{dc}(t)$ . (a) Restoration time estimated from  $\Delta V_{dc\_1-order}(t)$ . (b) Restoration time calculated from  $\Delta V_{dc}(t)$ .

### 2.3.3. Design Procedure of the HPF

As analyzed above, both the inertial supportability of GCCs and the restoration time of DC-link voltage should be considered in the design stage of  $f_{cut}$ . To ensure the successful

inertial support of GCCs (i.e.,  $\mu < 10\%$ ) and a fair DC-link voltage restoration time (i.e.,  $10 \text{ s} < t_{res} < 30 \text{ s}$ ), the flowchart for the design of  $f_{cut}$  is given in Fig. 2.12. Following the procedures in Fig. 2.12, with the system parameters provided in Table 2.1, the cut-off frequency of the HPF  $f_{cut}$  should be selected in a range from 0.00685 Hz to 0.0125 Hz.

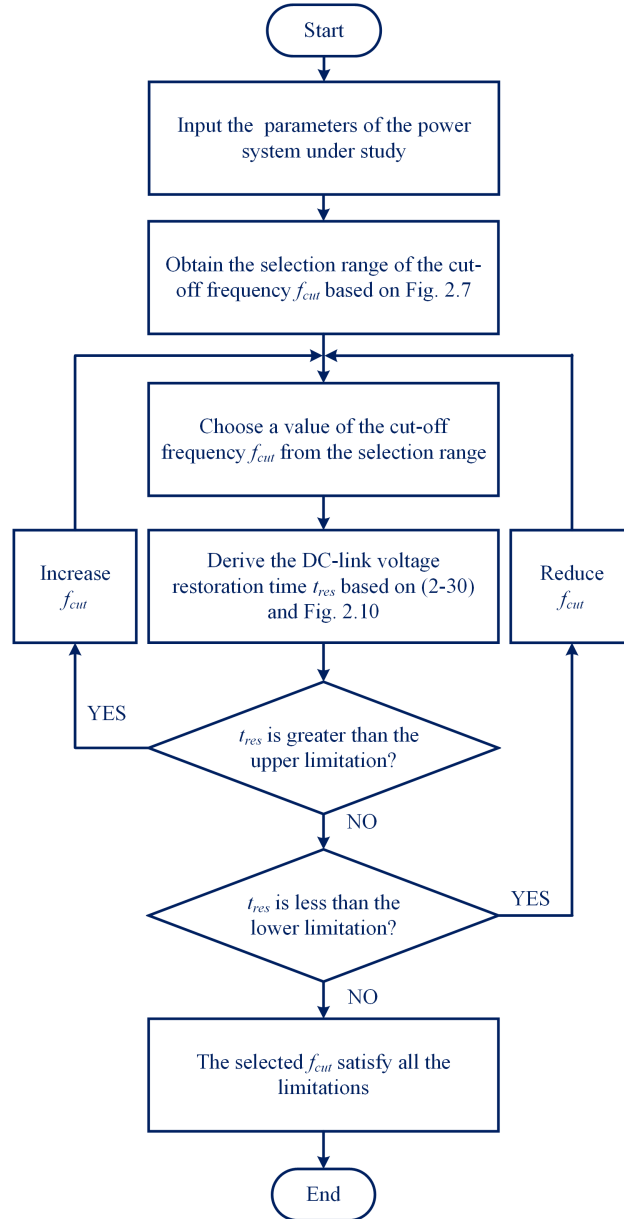


**Figure 2.12:** Design flowchart of the cut-off frequency  $f_{cut}$ .

---

## 2.4. Case Study

### 2.4.1. Simulation Results

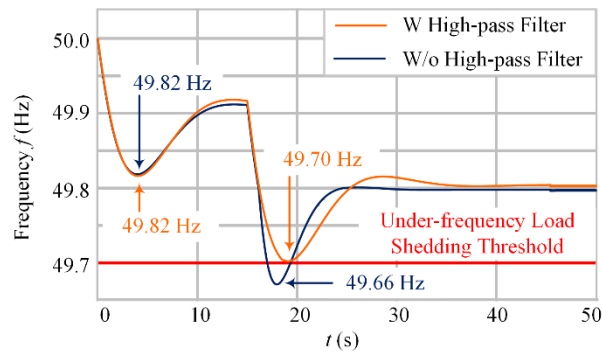
#### 1) Response to Cascading Frequency Events

The proposed DC-link voltage autonomous restoration method has been successfully verified in simulations through the Matlab/Simulink software. The system models shown in Fig. 2.3 without and with the proposed method have been constructed, and the parameters of the system can be found in Table 2.1. Based on the design procedure given in Section 2.3, the cut-off frequency  $f_{cut}$  of the HPF is set to be 0.01 Hz to guarantee that the inertia supportability of GCCs can be maintained, and the DC-link voltage restoration time can be kept in the range from 10 s to 30 s. The simulation results of frequency and DC-link voltage responses when subjected to the cascading 4% step-up load changes are shown in Fig. 2.13.

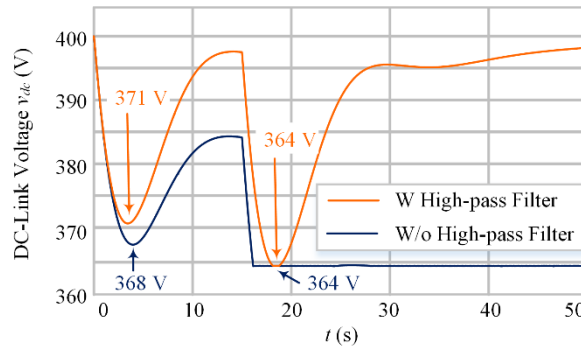
As observed from Fig. 2.13, without the proposed method, the frequency nadir in the 1<sup>st</sup> step-up load change is 49.82 Hz, and the DC-link voltage drops to 368 V to release power and provide inertia support. After the 1<sup>st</sup> load change, due to the proportional relationship between  $f$  and  $v_{dc}$ , the DC-link voltage changes in proportional to the grid frequency and cannot restore its nominal value, and as a result, the GCC could not provide inertial support in the cascaded frequency events. Then, when subjected to the 2<sup>nd</sup> step-up load change, the frequency declines to 49.66 Hz, and the maximum frequency deviation  $\Delta f_{max}$  is 0.34 Hz accordingly. Since the DC-link voltage is not restored after the 1<sup>st</sup> step-up load change, the DC-link voltage quickly touches its saturated value, e.g., 364 V, during the 2<sup>nd</sup> step-up load change.

It should be remarked that the thresholds of under-frequency load shedding are prescribed by many grid codes. For example, in Singapore, the threshold is set to be 49.70 Hz in the Transmission Code of the Energy Market Authority [92]. Once the grid frequency drops

below the threshold value, e.g., 49.70 Hz, non-critical loads will be automatically tripped out by the under-frequency load shedding system to assist the dynamic stability of the power system at the expense of additional operating costs. As shown in Fig. 2.13(a), without the proposed autonomous virtual inertia restoration method, the grid frequency drops below 49.70 Hz in the 2<sup>nd</sup> frequency event, and thus the under-frequency load shedding will be triggered, which incurs additional operating costs in practical conditions.



(a)



(b)

**Figure 2.13:** Simulation results of frequency and DC-link voltage responses to 4% step-up load changes. (a) Post-disturbance frequency responses. (b) Post-disturbance DC-link voltage responses.

When the proposed method is adopted, it can be seen from Fig. 2.13 that the frequency nadir in the 1<sup>st</sup> step-up load change is around 49.82 Hz, which is almost the same as that in the case without the proposed method. Thus, following the HPF design procedure, the

---

inertial supportability of GCCs is guaranteed. Meanwhile, the DC-link voltage drops to 371 V to output inertial power and provide inertia support. After the 1<sup>st</sup> load change, it can be observed that the DC-link voltage is no longer in proportion to the grid frequency. Instead, it quickly increases to 398 V, e.g., 99.5% of its nominal value. With the restored DC-link voltage, the GCC is capable of providing multiple inertia supports in the cascading frequency events, and as a result, in the 2<sup>nd</sup> step-up load change, the frequency nadir is 49.70 Hz, and the maximum frequency deviation  $\Delta f_{\max}$  is 0.30 Hz. As a result, a nearly 11.8% improvement in term of the maximum frequency deviation as compared with the previous case can be expected. Moreover, since the frequency nadir is maintained not crossing the threshold, the under-frequency load shedding can also be avoided according to the Singapore Transmission code.

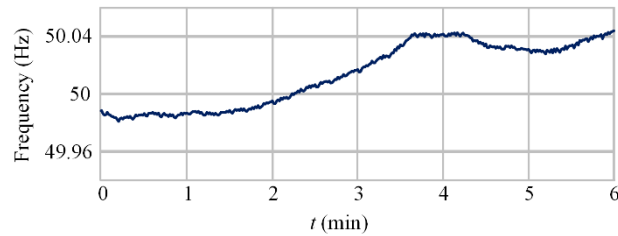
After providing virtual inertia support in the 2<sup>nd</sup> load change, the DC-link voltage reduces to 364 V, and it can be quickly restored again to get prepared for another frequency event. In addition, in Fig. 2.13(a), the two frequency response curves overlap with each other after load step changes, indicating that the proposed method has no adverse impact on the RoCoF as analyzed in Section 2.3.

## 2) Response to Grid Frequency Fluctuations in Normal Operating Conditions

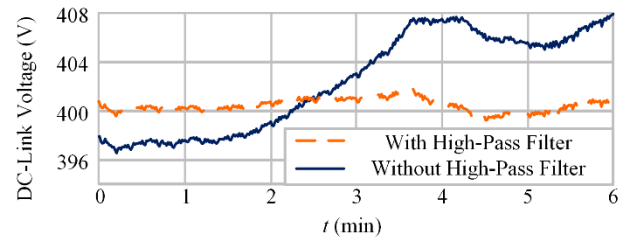
To test the effectiveness of the proposed method in suppressing the DC-link voltage fluctuations in normal operating conditions, a set of 6-minute grid frequency data recorded from the Singapore power system on 13th December 2017 was employed and plotted in Fig. 2.14(a). It is clear that the grid frequency varies from 49.98 Hz to 50.05 Hz. In accordance with the grid frequency curve, the DC-link voltage curves with and without the proposed method are shown in Fig. 2.14(b).

It is evidently demonstrated in Fig. 2.14(b) that without the proposed method, due to the proportional controller inside the virtual inertia block, the DC-link voltage shares the same waveform with the grid frequency, and extensive fluctuations can be observed with changes from 397 V to 408 V. When the proposed method is incorporated, the DC-link

voltage no longer follows the fluctuations of the grid frequency and remains nearly around a constant value of 400 V, e.g., the rated voltage. As a consequence, the maximum DC-link voltage deviation is also reduced to only 2 V accordingly, which indicates a 75% reduction in term of the fluctuation magnitude as compared with the case without the designed HPF.



(a)



(b)

**Figure 2.14:** Simulation results of DC-link voltage responses to grid frequency fluctuations in normal operating conditions. (a) Grid frequency. (b) DC-link voltage.

## 2.4.2. Experimental Results

### 1) Response to Cascading Frequency Events

In order to further verify the effectiveness of the proposed method, hardware experiments were carried out based on a small-scale power system, whose schematic diagram is shown in Fig. 2.15, where the system parameters are the same as simulation parameters in Table 2.1, except for that the power rating, which is derated to 1 kVA.

The experimental power system consists of a virtual synchronous generator (VSG) and a GCC. The VSG is used to emulate the synchronous generator so that the effectiveness of the proposed DC-link voltage restoration method for GCCs can be validated, and its detailed control structure can be found in [82]. The GCC, equipped with the virtual inertia control as well as the DC-link voltage restoration control, is connected in parallel with the VSG. A double-loop controller (the cascaded voltage and current control) is utilized to regulate the GCC, and its control loop is detailed in [35].

A photo of the experimental platform is shown in Fig. 2.16. As shown in Fig. 2.16, a dSPACE control platform (dSPACE: Microlabbox) was involved to realize the control algorithms of the GCC and the VSG. The DC-link voltage of the VSG was supplied by a constant DC power source (Itehc: IT6500C). One oscilloscope (Teledyne LeCroy: HDO8038) was employed to display and record the experimental waveforms. Fig. 2.17 demonstrates the steady-state waveforms of the three-phase grid voltages  $v_{abc}$  and the three-phase currents  $i_{Vabc}$ . It can be observed that these waveforms are sinusoidal with the help of the VSG control. The steady-state waveforms also show that the incorporation of the HPF does not affect the normal operating conditions of the power system.

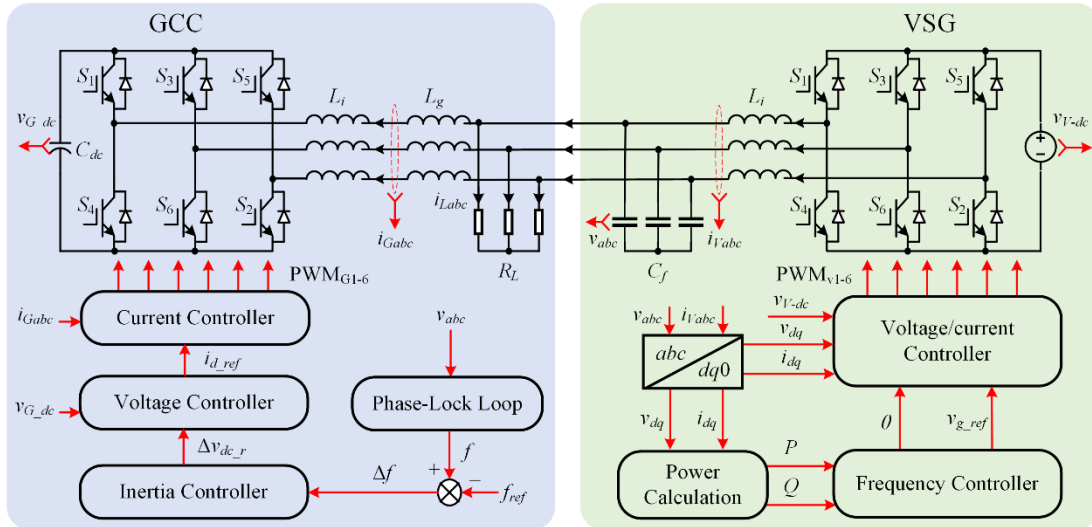


**Figure 2.15:** Schematic diagram of the experimental small-scale power system.



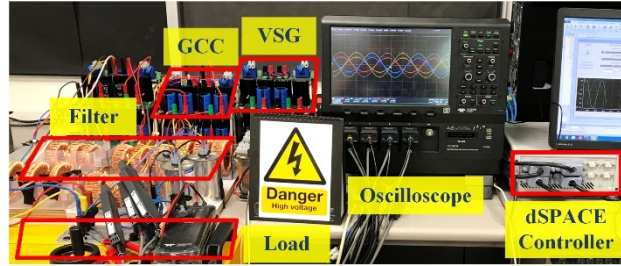


**Figure 2.16:** Photo of the experimental platform.

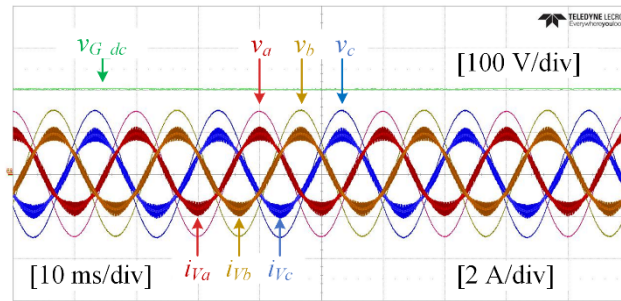


**Figure 2.17:** Steady-state experimental waveform.

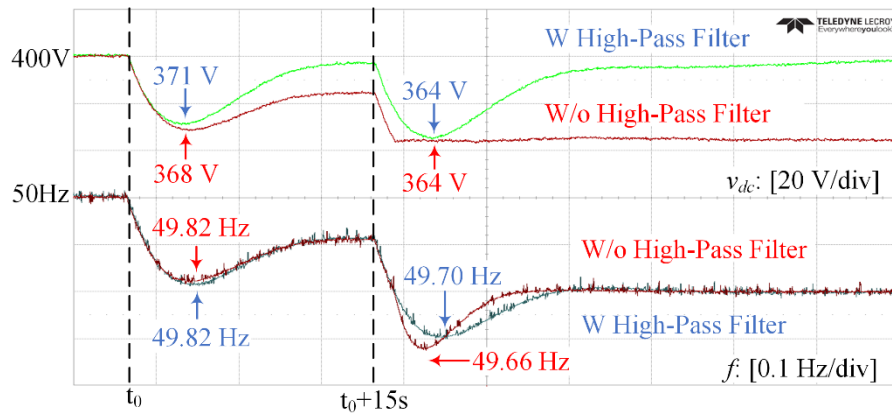


**Figure 2.18:** Experimental results of the systems with and without the proposed DC-link voltage restoration method during 4% cascading step-up load changes.

Fig. 2.18 shows the experimental results of the systems with and without the proposed DC-link voltage restoration method when subjected to the cascading 4% step-up load changes. Without the proposed method, the frequency nadir is 49.82 Hz in the 1<sup>st</sup> load change and 49.66 Hz in the 2<sup>nd</sup> load change. Besides, the DC-link voltage of the GCC varies in proportion to the grid frequency and cannot restore to its nominal value. With the proposed

method enabled, it can be obtained from Fig. 2.18 that the DC-link voltage can be quickly restored after the load change. In addition, the frequency nadir in the 1<sup>st</sup> load change is 49.82 Hz, which is the same as that obtained without the proposed method. In the 2<sup>nd</sup> load change, the frequency nadir rises from 49.66 Hz to 49.70 Hz, indicating an 11.8% reduction in the maximum frequency deviation.

## 2) Response to Grid Frequency Fluctuations in Normal Operating Conditions

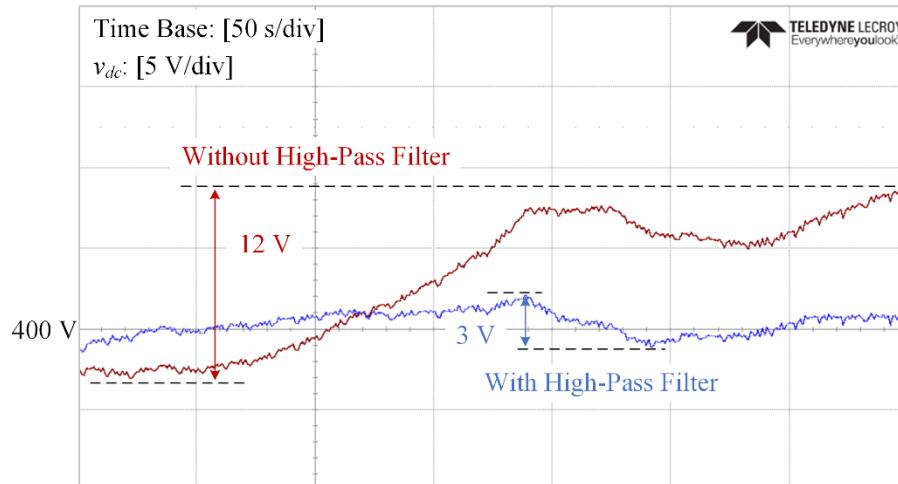


**Figure 2.19:** Experimental results of the DC-link voltage responses under normal operating conditions.

To further validate the effectiveness of the proposed method in suppressing the DC-link voltage fluctuations in normal operating conditions, experiments have been conducted based on the small-scale power system depicted in Fig. 2.16. The frequency of the Singapore power system (see Fig. 2.14(a)) is used as the input to the inertia controller, and the experimental results are shown in Fig. 2.19. By comparing Fig. 2.14(a) and Fig. 2.19, it can be noticed that without the HPF the waveform of the DC-link voltage follows that of the grid frequency, and the maximum DC-link voltage change is 12 V. With the proposed method activated, the DC-link voltage no longer changes proportionally to the grid frequency, and it is maintained around its rated value. Specifically, the maximum DC-link voltage change declines to 3 V, indicating a 75% reduction in term of the fluctuation magnitude.

---

## 2.5. Summary

This chapter has proposed an autonomous DC-link voltage restoration method for grid-connected converters. It is achieved by using a high-pass filter, which extracts out only high-frequency components from the grid frequency for inertial emulation during frequency events. As a result, the DC-link voltages of grid-connected converters can be restored autonomously after releasing their inertial power during each frequency event and thus avoid the abnormal working conditions of power converters. Moreover, the restored DC-link voltages make it possible for grid-connected converters to provide inertia support during cascading frequency events. Furthermore, the proposed method also decouples the DC-link voltage from the grid frequency under normal operating conditions of power systems, and thus the DC-link voltage fluctuations can be extensively suppressed. The design procedure of the high-pass filter is also presented in this chapter, considering both the inertia supportability of grid-connected converters and the DC-link voltage restoration time. Simulation and experimental results have successfully verified the effectiveness of the proposed method.



---

## Chapter 3

### Stability Issue Regarding Droop Control in Islanded Microgrids

*This chapter studies the stability issue of droop controlled islanded microgrids. For islanded microgrids employing droop control to achieve power-sharing among multiple power generating units, a relatively large droop gain benefits the accurate power-sharing at the expense of sacrificed dynamic stability. Moreover, it is revealed that such stability issue is associated with the power control stages of power converters, with a typical response time of hundreds of milliseconds, and simply tuning control parameters could not deal with this stability problem. Therefore, a converter-based power system stabilizer (CBPSS) is developed in this chapter to synchronize a damping torque to the islanded microgrid, so that the stability and transient performance can of the islanded microgrids be enhanced. In addition, the approach to identify the optimal installation location of the designed CBPSS is also demonstrated.*

---

### 3.1. Introduction

In response to the carbon reduction issue, an increasing amount of renewable energy is being integrated into modern power systems, and the conventional power grids are evolving towards smart grids for a more sustainable future. In such a transition, the concept of microgrid plays a critical role and serves as the medium to accommodate renewable generators on the distribution level [93, 94]. One of the compelling characteristics of microgrids is the possibility of seamless switch between grid-connected and islanded operating modes, and thus significantly improving the power supply reliability for local loads and flexibility for the emerging smart grids [95]. Besides, the microgrid also features upgraded power generation efficiency as well as improved power quality [11, 52]. Thus, the practical applications of microgrids have been extensively witnessed in the past decade. In microgrids, distributed generators are usually coupled through VSCs, and the well-known droop control is highly preferred due to the merits of autonomous power sharing and communication independency [96].

One main concern regarding the wide application of microgrids is the stability issue in face of disturbances. To address this concern, the state-space model of an autonomous microgrid is established in [97], involving detailed dynamics regarding controllers within different time frames as well as filters and networks. On the basis of the established model, the stability of microgrids is discussed from diversified perspectives [8-12]. The impacts of grid strength and control parameters on microgrid stability are investigated in [98, 99]; a graphic tool is provided in [100] to recognize the stability region of microgrids. Besides, the interactions between microgrids and active loads are analyzed in [101, 102].

Then, different approaches have been developed to enhance the stability of microgrids. Optimization methods are given in [99, 103] to tune the control parameters regarding interface VSCs, so that the overall stability of microgrids can be ensured. Adaptive control also shows potential in the stability enhancement of microgrids: a feedforward loop is developed in [104] to modify the dynamics between interface VSCs and the host microgrid, and the parameters of the designed feedforward loop are adaptively selected according to

---

operating conditions; in [105], a transient droop gain is designed to stabilize microgrids, which is adaptively tuned to improve the damping of the overall microgrid. Besides, multi-level control architectures are used to solve the microgrid instability problem: a two-level hierarchical control based on phase measurement unit is proposed in [106] to eliminate the microgrid frequency deviations caused by load fluctuations; the effectiveness of the distributed secondary control approach in avoiding Hopf bifurcation of microgrids is validated in [107].

Power system stabilizer (PSS), of which the concept was first proposed by DeMello [108], has been mutually applied to damp synchronous generator oscillations. For synchronous generators, fast acting excitation system with high-gain automatic voltage regulator (AVR) gives good voltage controllability and increases synchronizing torques, but at the expense of deteriorating damping torques and giving rise to oscillatory behaviors of generators [108]. Therefore, PSS is designed for synchronous generators to compensate the phase lag regarding the excitation system [109]. Besides, studies in [110] demonstrate that, for synchronous generators, the frequency response from the AVR input to the resultant electrical torque at the generator shaft is principally determined by the synchronous generator itself, and thus a single-machine-infinite-bus (SMIB) model is commonly employed in the design of PSS for synchronous generators [111-113].

However, things are different for converter-based islanded microgrids. In spite of the substantial difference between physical structures of power converters and synchronous generators, the low-frequency oscillations in converter-based islanded microgrids are mainly caused by the power exchange between converters with large droop gains. Moreover, since power output characteristic of converters is determined by droop gains, reducing droop gains will compromise the power output characteristic of converters. As a result, additional control loops need to be designed to deal with the low-frequency oscillations in converter-based islanded microgrids. Besides, converters inside an islanded microgrid are tightly coupled with each other [114], and thus the dynamics of one converter are not only characterized by the control loops of its own, but also impacted by the regulating actions of other converters inside the microgrid [115]. Therefore, the PSS design

---

method in synchronous generators, which is based on the SMIB model and aimed to handle the oscillations associated with fast-acting excitation systems, cannot be transplanted directly to the converter-based scenarios, and the influence of interaction between converters should also be considered in the design of PSS for converter-based islanded microgrids.

Several attempts have been carried out to apply the concept of PSS to converter-based situations. In [116], an auxiliary controller is designed to compensate the phase lags of low-pass filters inside power controllers of grid forming converters, so that the low-frequency oscillation in microgrid can be mitigated. Nonetheless, as described in [97, 117], the low-frequency oscillation of an islanded microgrid is associated with the sophisticated interaction among multiple controllers and circuits. As a result, merely compensating the phase lag of the low-pass filter is not enough for a comprehensive phase compensation. Studies in [118, 119] highlight the instability associated with large droop gains of converters, and a phase compensation loop is designed to solve this problem. However, the parameters of the phase compensator are obtained with swarm optimization method, e.g., a kind of evolutionary algorithms, which is not intuitive and hard to be generalized to other cases. Moreover, the evolutionary algorithm may fall into local optimum, and it is hard to converge when the parameter searching space is huge [120], probably leading to the failure of obtaining available parameters for phase compensators. In addition, the design of these phase compensation loops in [116, 118, 119] assumes that the converters are connected to infinite buses, neglecting the interaction among converters in islanded microgrids.

In light of these problems, this chapter proposes a converter-based PSS (CBPSS), serving as a supplementary control loop to improve the stability of islanded microgrids. Different from the PSS for synchronous generators or the PSS applied to converters in above-mentioned studies, the proposed CBPSS is designed from the view of microgrids, taking the interaction among converters inside microgrids into consideration. The proposed CBPSS starts with the identification of the forward loop from the CBPSS to the islanded microgrid, signifying a clear physical mechanism of stabilizing effect to the microgrid via introducing an additional damping torque. Then, the parameters of the CBPSS are deigned



---

accordingly so that the phase lag of the identified forward loop can be compensated. Different from previous studies, the CBPSS parameters can be obtained easily without the need of any evolutionary algorithms, and thus, drawbacks of evolutionary algorithms can be avoided. Consequently, an additional damping torque is generated from the CBPSS for the microgrid. Furthermore, an eigenvalue-mobility-based method is presented to find the optimal installation location for the proposed CBPSS in the islanded microgrid, so that the maximum stabilizing effect can be realized with the least controller design effort.

The remainder of this chapter is organized as follows. The model of an islanded microgrid with the proposed CBPSS is first established. After that, the design of the proposed CBPSS is illustrated along with the selection of optimal location of the CBPSS. Case studies including modal analysis and time-domain simulations, as well as experimental results also are given to verify the feasibility and effectiveness of the CBPSS.

### **3.2. Stability Problem with Droop Control**

The typical schematic of the islanded microgrid under study is depicted in Fig. 3.1, in which three VSCs work together to supply two local loads. Each VSC is connected to an ac bus, and  $u_{bi}$  stands for the node voltage of the  $i$ th bus. The three ac buses connect with each other through two connecting lines, and the current flowing through the  $i$ th connecting line is denoted by  $i_{linei}$ . For the  $i$ th VSC in Fig. 3.1,  $L_{fi}$  and  $C_{fi}$  are the inductance and capacitance of the LC filter, respectively;  $L_{ci}$  is the coupling inductance between the  $i$ th VSC and its associated ac bus;  $u_{ii}$  designates the terminal voltage and  $u_{oi}$  signifies the output voltage; the currents flow through  $L_{fi}$  and  $L_{ci}$  are denoted by  $i_{li}$  and  $i_{oi}$ , respectively.

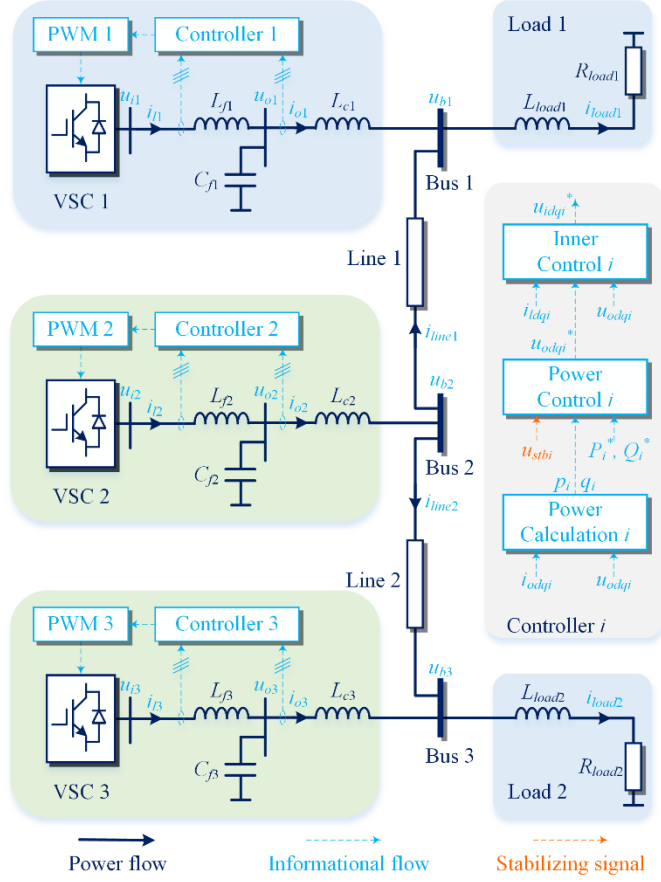


**Figure 3.1:** Diagram of a typical islanded microgrid.

### 3.2.1. Model of VSC Subsystem

For a single VSC, its model contains the controller part and the circuit part. For the controller part, as illustrated in Fig. 3.1, a cascaded architecture is implemented under the synchronous  $dq$  frame, and both the outer power controller and the inner voltage and current controller are incorporated in the cascaded control architecture.

#### 1) Power controller.

For the power controller of the  $i$ th VSC, droop characteristics are employed to generate  $\omega_{ci}$ , the angular speed of the rotating  $dq$  frame, and  $u_{odi}^*$ , the reference of the output voltage for the fundamental component.

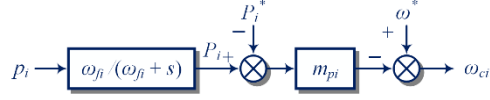


**Figure 3.2:** Active power droop control of the  $i$ th VSC.

For the active power droop control, as shown in Fig. 3.2, the basic idea is to emulate the governor response of synchronous generators, so that the VSC can respond to load changes by modifying  $\omega_{ci}$  accordingly. Based on Fig. 3.2, the active power droop control of the  $i$ th VSC is expressed as

$$\omega_{ci} = \omega_c^* - m_{pi} (P_i - P_i^*) \quad (3-1)$$

where  $P_i^*$  and  $\omega_c^*$  signify the references of the active power and the angular speed, respectively;  $m_{pi}$  represents the active power droop gain;  $P_i$  refers to the active power regarding the fundamental components of the  $i$ th VSC, and it is obtained by filtering  $p_i$ , the instantaneous active power of the  $i$ th VSC, as

$$P_i = \frac{\omega_{fi}}{s + \omega_{fi}} p_i \quad (3-2)$$

in which  $\omega_{fi}$  is the cut-off frequency of the low-pass filter [121, 122].

By substituting (3-2) into (3-1) and eliminating the derivatives of constant terms, the active power droop control of the  $i$ th VSC can be re-expressed as

$$\frac{1}{\omega_{fi} m_{pi}} s \omega_{ci} = P_i^* - p_i - \frac{1}{m_{pi}} (\omega_{ci} - \omega_c^*) \quad (3-3)$$

From (3-3), it is observed that the active power droop control shares a similar form with the motion equation of synchronous generators, and thus the equivalent inertia  $M_{ci}$  and damping term  $D_{ci}$  for the  $i$ th VSC are defined respectively as

$$M_{ci} = \frac{1}{\omega_{fi} m_{pi}}, \quad D_{ci} = \frac{1}{m_{pi}} \quad (3-4)$$

For the ease of statement, the angle difference  $\delta_{ci}$  between the  $i$ th VSC coordinate and the common frame is denoted as

$$s\delta_{ci} = \omega_{ci} - \omega_n \quad (3-5)$$

where  $\omega_n$  is the nominal angular frequency.

By linearizing (3-3) and (3-5), the small-signal model of the active power droop control in the motion equation form is obtained, as shown in Fig. 3.3, in which the prefix “ $\Delta$ ” stands for small deviations from steady-state values.

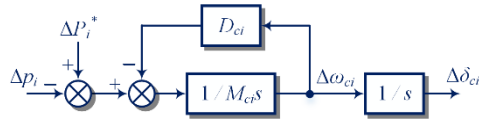


**Figure 3.3:** Active power control in the motion equation form.

Similar to the active power control, the droop characteristic is also applied in reactive power regulation to tune the output voltage reference  $u_{odi}^*$  for the  $i$ th VSC, as shown in Fig. 3.4.

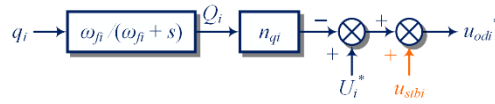


**Figure 3.4:** Reactive power droop control of the  $i$ th VSC.

However, different from the conventional reactive power droop control, an additional stabilizing signal  $u_{stbi}$ , generated by the proposed CBPSS, is added into the reactive power control loop to improve the microgrid stability. The structure of the CBPSS to produce  $u_{stbi}$  will be detailed in Section III. Then, from Fig. 3.4, the reactive power control of the  $i$ th VSC equipped with the proposed CBPSS, is denoted as

$$u_{odi}^* = U_i^* - n_{qi} Q_i + u_{stbi} \quad (3-6)$$

where  $U_i^*$  is the voltage reference;  $n_{qi}$  is the reactive power droop gain;  $Q_i$  denotes the fundamental component reactive power of the  $i$ th VSC, obtained from the instantaneous reactive power  $q_i$  by passing through a low-pass filter.

In addition to the power controller, the control loop of the  $i$ th VSC also includes the inner voltage and current controller, and the widely used proportional and integral (PI) controllers are adopted for the inner control loops to track  $u_{odi}^*$ . Details of the inner controller can be found in [97]. For the circuit model of the  $i$ th VSC, dynamics of LC filter as well as the coupling inductance are also considered, and all these models are established in the individual  $dq$  frame of the  $i$ th VSC.

## 2) Model of the VSC subsystem.

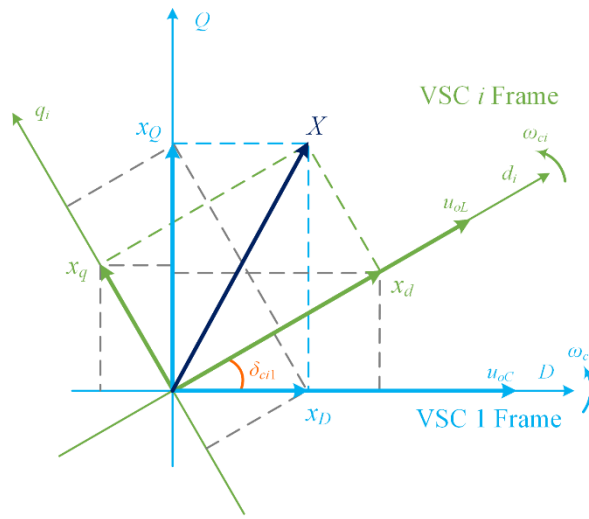


**Figure 3.5 :** Coordinate transformation.

For the microgrid, there are always more than one VSC, and each VSC is modelled on its own  $dq$  frame, as shown in Fig. 3.5. To establish the VSC subsystem model, the frame of VSC 1 is taken as the reference frame, signified as  $DQ$ , and all other VSCs modelled in their individual frames, denoted as  $dq_i$  for the  $i$ th VSC, are converted into the  $DQ$  frame, with the following equation

$$x_{DQ} = \begin{bmatrix} \cos \delta_{ci1} & -\sin \delta_{ci1} \\ \sin \delta_{ci1} & \cos \delta_{ci1} \end{bmatrix} x_{dq} \quad (3-7)$$

in which  $\delta_{ci1}$  is the angle difference between the frame  $dq_i$  and reference frame  $DQ$ , as

$$\delta_{ci1} = \delta_{ci} - \delta_{c1} \quad (3-8)$$

Then, the model of the VSC subsystem is derived by combining all the individual VSC models, as

$$s[\Delta\mathbf{X}_{CON}] = \mathbf{A}_{CON}[\Delta\mathbf{X}_{CON}] + \mathbf{B}_{1CON}[\Delta\mathbf{U}_{bDQ}] + \mathbf{B}_{2CONi}[\Delta\mathbf{u}_{stbi}] \quad (3-9)$$

where  $[\Delta\mathbf{X}_{CON}]$  is the VSC subsystem state variable vector;  $\Delta\mathbf{U}_{bDQ}$  is the node voltage vector.  $\mathbf{A}_{CON}$  denotes the state matrix;  $\mathbf{B}_{1CON}$  and  $\mathbf{B}_{2CONi}$  signify the input matrices of different inputs to the VSC subsystem.

The outputs of the VSC subsystem are selected as

$$[\Delta\omega_{c1}] = \mathbf{C}_{CON\omega}[\Delta\mathbf{X}_{CON}] \quad (3-10)$$

$$[\Delta\mathbf{I}_{oDQ}] = \mathbf{C}_{CONC}[\Delta\mathbf{X}_{CON}] \quad (3-11)$$

### 3.2.2. Model of the Microgrid with the CBPSS

#### 1) Model of the network and load subsystem.

To give a detailed microgrid model, dynamics of the network and loads are considered. Both the network and loads are modelled on the reference  $DQ$  frame. The network subsystem can be written as

$$s[\Delta\mathbf{I}_{lineDQ}] = \mathbf{A}_{NET}[\Delta\mathbf{I}_{lineDQ}] + \mathbf{B}_{1NET}[\Delta\mathbf{U}_{bDQ}] + \mathbf{B}_{2NET}[\Delta\omega_{c1}] \quad (3-12)$$

A general RL load is considered in this chapter with a state-space model expressed as

$$s[\Delta\mathbf{I}_{loadDQ}] = \mathbf{A}_{LOAD}[\Delta\mathbf{I}_{loadDQ}] + \mathbf{B}_{1LOAD}[\Delta\mathbf{U}_{bDQ}] + \mathbf{B}_{2LOAD}[\Delta\omega_{c1}] \quad (3-13)$$

In (3-12) and (3-13),  $[\Delta\mathbf{I}_{lineDQ}]$  and  $[\Delta\mathbf{I}_{loadDQ}]$  denote the line currents and load currents, respectively. Details on the network and load subsystem models can be obtained in [97].

#### 2) State-space model of the microgrid with CBPSS.

From (3-9), (3-12), and (3-13), the node voltages  $[\Delta\mathbf{U}_{bDQ}]$  of the microgrid are taken as the

input into each subsystem, and a method is presented in [97] to define the node voltages with the virtual resistance  $r_N$ , as

$$\left[ \Delta U_{bDQ} \right] = \mathbf{R}_N \mathbf{M}_{CON} \left[ \Delta \mathbf{I}_{oDQ} \right] + \mathbf{R}_N \mathbf{M}_{NET} \left[ \Delta \mathbf{I}_{lineDQ} \right] + \mathbf{R}_N \mathbf{M}_{LOAD} \left[ \Delta \mathbf{I}_{loadDQ} \right] \quad (3-14)$$

where  $\mathbf{R}_N$  is a diagonal matrix with elements being  $r_N$ ;  $\mathbf{M}_{CON}$ ,  $\mathbf{M}_{NET}$ , and  $\mathbf{M}_{LOAD}$  stand for the mapping matrices to assign the VSCs, lines or loads to different node voltages, among which  $\mathbf{M}_{CON}$  is a unity matrix;  $\mathbf{M}_{NET}$  is a matrix filled with +1 or -1, depending on the direction of line current is entering or leaving the node;  $\mathbf{M}_{LOAD}$  is a matrix filled with -1 at the entries corresponding to the nodes with loads connected.

With the node voltages defined in (3-14), the microgrid becomes an autonomous system, and thus the model of the microgrid with the proposed CBPSS installed at the  $i$ th VSC can be derived by integrating the VSC subsystem model, given by (3-9), the network subsystem model, expressed in (3-12), and the load subsystem model, characterized by (3-13), as

$$s \left[ \Delta \mathbf{X}_{MG} \right] = \mathbf{A}_{MG} \left[ \Delta \mathbf{X}_{MG} \right] + \mathbf{B}_{iMG} \left[ \Delta u_{stbi} \right] \quad (3-15)$$

in which

$$\left[ \Delta \mathbf{X}_{MG} \right] = \left[ \Delta \mathbf{X}_{CON}^T \quad \Delta \mathbf{I}_{lineDQ}^T \quad \Delta \mathbf{I}_{loadDQ}^T \right]^T \quad (3-16)$$

and the characteristic matrix  $\mathbf{A}_{MG}$  is expressed as

$$\mathbf{A}_{MG} = \left[ \begin{array}{c|c|c} \mathbf{A}_{CON} + \mathbf{B}_{1CON} \mathbf{R}_N \mathbf{M}_{CON} \mathbf{C}_{CONC} & \mathbf{B}_{1CON} \mathbf{R}_N \mathbf{M}_{NET} & \mathbf{B}_{1CON} \mathbf{R}_N \mathbf{M}_{LOAD} \\ \hline \mathbf{B}_{1NET} \mathbf{R}_N \mathbf{M}_{CON} \mathbf{C}_{CONC} + \mathbf{B}_{2NET} \mathbf{C}_{CON\omega} & \mathbf{A}_{NET} + \mathbf{B}_{1NET} \mathbf{R}_N \mathbf{M}_{NET} & \mathbf{B}_{1NET} \mathbf{R}_N \mathbf{M}_{LOAD} \\ \hline \mathbf{B}_{1LOAD} \mathbf{R}_N \mathbf{M}_{CON} \mathbf{C}_{CONC} + \mathbf{B}_{2LOAD} \mathbf{C}_{CON\omega} & \mathbf{B}_{1LOAD} \mathbf{R}_N \mathbf{M}_{NET} & \mathbf{A}_{LOAD} + \mathbf{B}_{1LOAD} \mathbf{R}_N \mathbf{M}_{LOAD} \end{array} \right] \quad (3-17)$$

The output of the microgrid model is selected as the angular speed of the  $i$ th VSC, as

$$\left[ \Delta \omega_{ci} \right] = \mathbf{C}_{iMG} \left[ \Delta \mathbf{X}_{MG} \right] \quad (3-18)$$

For the proposed CBPSS, the  $i$ th VSC angular speed  $\Delta \omega_{ci}$  is taken as the input of the CBPSS to generate the stabilizing signal  $\Delta u_{stbi}$ , expressed as

$$\Delta u_{stbi} = G_{CBPSS_i}(s) \cdot \Delta \omega_{ci} \quad (3-19)$$

in which  $G_{CBPSS_i}(s)$  denotes the transfer function from  $\Delta \omega_{ci}$  to  $\Delta u_{stbi}$  when the proposed CBPSS is installed at the  $i$ th VSC.

Combing (3-15), (3-18), and (3-19), a closed-loop model of the microgrid with the proposed CBPSS is established and shown in Fig. 3.6. Details of the structure, the design, and the selection of optimal installation location of the CBPSS will be presented in the following.

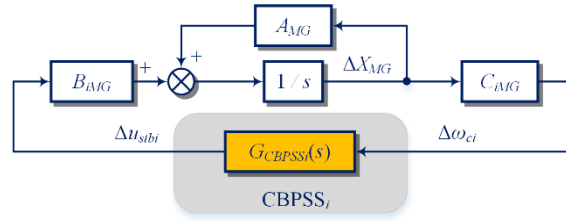


**Figure 3.6:** Closed-loop model of the microgrid with the CBPSS.

### 3.3. Converter-Based Power System Stabilizer for Stability Enhancement of Droop-Controlled Islanded Microgrids

#### 3.3.1. Optimal Installation Location of the Proposed CBPSS

When utilizing the proposed CBPSS in microgrids, the first step is to recognize the optimal installation location of the CBPSS, e.g., at which converter the proposed CBPSS should be installed. Identification of the optimal installation location is important because the concerned oscillation mode of the microgrid may be insensitive to some VSCs. As a result, installing CBPSSs on the insensitive VSCs has little contribution to damp the concerned oscillation mode, but only increases the complexity of control architecture. Besides, the optimal installation location of the CBPSS ensures that the maximum stabilizing effect can be achieved with the least controller design effort. In this chapter, the eigenvalue mobility



is employed to determine the CBPSS optimal installation location.

For (3-15), assuming a feedback is expressed as

$$\Delta u_{stbi} = \delta K \cdot \Delta \omega_{ci} \quad (3-20)$$

in which  $\delta K$  is the incremental feedback gain.

With the feedback, the open-loop model (3-15) turns into a closed-loop system, and an eigenvalue migration  $\delta \lambda_i$ , which is the difference between the open-loop system eigenvalue and the closed-loop system eigenvalue, is resulted from the feedback. Then, the eigenvalue mobility  $\mu_i$  is defined as

$$\mu_i = \left\| \frac{\delta \lambda_i}{\delta K} \right\| \quad (3-21)$$

where “ $\| \cdot \|$ ” stands for the Euclidean norm.

According to (3-21),  $\mu_i$  reflects the ratio of the incremental change of the open-loop eigenvalue  $\lambda_i$  to the gain used to effect such a change, and a larger  $\mu_i$  means a greater impact in modifying  $\lambda_i$ , assuming the same control gain is given [123].

By taking (3-18) and (3-20) into (3-15), the closed-loop model with the feedback involved is derived, as

$$s[\Delta \mathbf{X}_{MG}] = (\mathbf{A}_{MG} + \mathbf{B}_{iMG} \cdot \delta K \cdot \mathbf{C}_{iMG})[\Delta \mathbf{X}_{MG}] \quad (3-22)$$

Thus, the eigenvalue migration  $\delta \lambda_i$  can be calculated as [124]

$$\delta \lambda_i = w_i^T \mathbf{B}_{iMG} \cdot \delta K \cdot \mathbf{C}_{iMG} v_i \quad (3-23)$$

where  $v_i$  and  $w_i^T$  are the right and left eigenvectors of  $\mathbf{A}_{MG}$  corresponding to the open-loop eigenvalue  $\lambda_i$ , respectively, and they are normalized to have  $w_i^T v_i = 1$ .

By substituting (3-23) into (3-21), the expression of the eigenvalue mobility is modified as

$$\mu_i = \left\| \frac{\delta \lambda_i}{\delta K} \right\| = \left\| w_i^T \mathbf{B}_{iMG} \mathbf{C}_{iMG} v_i \right\| \quad (3-24)$$

From (3-24),  $\mu_i$  gives an indication of how feasible it is to modify the eigenvalue  $\lambda_i$ , and it

---

reveals the controllability of a given system when the feedback is imposed via different VSCs in the microgrid. In (3-24), as the angles between the vector  $w_i^T (v_i)$  and columns of  $\mathbf{B}_{iMG}$  (rows of  $\mathbf{C}_{iMG}$ ) depart from  $90^\circ$ , the mode becomes more controllable, and the value of  $\mu_i$  grows.

For the optimal installation location of the CBPSS, when the CBPSS is placed at different VSCs,  $\mathbf{B}_{iMG}$  and  $\mathbf{C}_{iMG}$  vary, and  $\mu_i$  changes, providing useful information on the controllability of the concerned oscillation mode when the CBPSS is installed at different VSCs. Then, the CBPSS should be placed at the VSC with the largest  $\mu_i$ , so that the greatest damping effect can be realized with the least control effort.

### 3.3.2. Design of the Proposed CBPSS

With the optimal installation location of the CBPSS identified, a phase compensation method is further applied to enhance microgrid stability. Through this effort, the damping ratio of the microgrid critical mode can be improved. The basic idea of the phase compensation approach lies on compensating the phase lag of a forward loop, so that the overall effect of the control loop after phase compensation turns into generating a pure damping torque to the system, and thus the stability can be enhanced.

With the proposed CBPSS, a forward loop from  $\Delta u_{stbi}$  to the microgrid is formed, and the critical part in achieving accurate phase compensation relies on the clear identification of the forward loop. Only with the clear identification of the forward loop, can the proposed CBPSS be tailored to synthesize a pure damping torque and consequently stabilize the microgrid.

Assuming the proposed CBPSS is installed at the  $i$ th VSC, due to the similarity between active power droop control and motion equation, the microgrid model (3-15) can be arranged as

$$s \begin{bmatrix} \Delta \mathbf{z}_1 \\ \Delta \omega_{ci} \\ \Delta \mathbf{z}_3 \end{bmatrix} = \begin{bmatrix} \mathbf{A}_{11} & \mathbf{A}_{12} & \mathbf{A}_{13} \\ 0 & -\frac{D_{ci}}{M_{ci}} & -\mathbf{A}_{23} \\ \mathbf{A}_{31} & \mathbf{A}_{32} & \mathbf{A}_{33} \end{bmatrix} \begin{bmatrix} \Delta \mathbf{z}_1 \\ \Delta \omega_{ci} \\ \Delta \mathbf{z}_3 \end{bmatrix} + \begin{bmatrix} \mathbf{0} \\ 0 \\ \mathbf{B}_3 \end{bmatrix} [\Delta u_{stbi}] \quad (3-25)$$

where  $\Delta \mathbf{z}_1$  and  $\Delta \mathbf{z}_3$  are the vectors containing all the state variables in  $\Delta \mathbf{X}_{MG}$ , except for  $\Delta \omega_{ci}$ ; correspondingly, the state matrix  $\mathbf{A}_{MG}$  is also divided into different blocks corresponding to  $\Delta \mathbf{z}_1$ ,  $\Delta \omega_{ci}$ , and  $\Delta \mathbf{z}_3$ , as shown in (3-25).

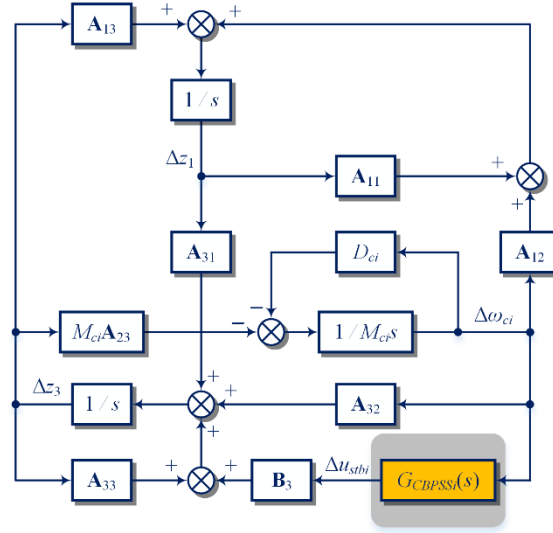


**Figure 3.7:** Motion-equation form of the closed-loop system.

Then, by substituting the CBPSS transfer function (3-19) into (3-25), the closed-loop system depicted in Fig. 3.6 is converted into Fig. 3.7. From Fig. 3.7, the clear physical meaning of the designed CBPSS is obtained, e.g., forming a supplementary loop and thus generating an additional electrical torque for the microgrid. The additional electrical torque produced by the proposed CBPSS is expressed as

$$\Delta T_{CBPSSi} = F_{stbi}(s) \cdot \Delta u_{stbi} \quad (3-26)$$

where  $F_{stbi}(s)$  is the transfer function of the forward loop from the CBPSS output  $\Delta u_{stbi}$  to the synthesized electrical torque  $\Delta T_{CBPSSi}$ . From Fig. 3.7, the forward loop transfer function can be clearly identified, expressed as

$$F_{stbi}(s) = M_{ci} \mathbf{A}_{23} \left\{ (s\mathbf{I} - \mathbf{A}_{33}) - \mathbf{A}_{31} (s\mathbf{I} - \mathbf{A}_{11})^{-1} \mathbf{A}_{13} \right\}^{-1} \mathbf{B}_3 \quad (3-27)$$

Assuming that the  $j$ th oscillation mode of the microgrid with an eigenvalue  $\lambda_j$  is the critical mode to be stabilized, substituting  $\lambda_j$  into (3-27) gives

$$F_{stbi}(\lambda_j) = G_F \angle \varphi_F \quad (3-28)$$

in which  $G_F$  and  $\varphi_F$  are the magnitude and phase lag of the forward loop  $F_{stbi}(s)$  at  $\lambda_j$ , respectively.

With the phase lag of the forward loop  $F_{stbi}(s)$  obtained in (3-28), the proposed CBPSS can be designed conveniently with the phase compensation method. In other words, to stabilize the  $j$ th oscillation mode of the microgrid, the design objective of the CBPSS is to compensate the phase lag  $\varphi_F$  for the forward loop  $F_{stbi}(s)$  at  $\lambda_j$ , so that a pure damping torque in phase with  $\Delta\omega_{ci}$  can be synthesized to boost the microgrid stability. Thus, the following equation should be satisfied, as

$$F_{stbi}(\lambda_j) G_{CBPSSi}(\lambda_j) = D_{stb} \quad (3-29)$$

where  $D_{stb}$  stands for the desired damping contributed by the CBPSS for the microgrid  $j$ th oscillation mode  $\lambda_j$ . It should be noted, since  $F_{stbi}(s)$  is derived from the microgrid model, the effect of the interaction among converters is considered in  $\varphi_F$ .

To realize the objective in (3-29), the structure of the proposed CBPSS, e.g.,  $G_{CBPSS}(s)$ , is illustrated in Fig. 3.8, in which a phase compensator  $G_{II}(s)$  is cascaded with a filter block  $G_{filter}(s)$ . The filter block  $G_{filter}(s)$  is consisted of a 1<sup>st</sup>-order low-pass filter with a cut-off frequency  $\omega_{lp}$  to reject high-frequency noises, and a washout filter with a time constant  $T_w$  to remove DC offset. Besides, a 2<sup>nd</sup>-order bandpass filter with a central frequency  $\omega_{bp}$  is also involved in the filter block  $G_{filter}(s)$  to pick out the components corresponding to the concerned mode  $\lambda_j$ , preventing other unconcerned modes being affected by the proposed CBPSS.

By substituting  $\lambda_j$  into  $G_{filter}(s)$ , the magnitude and phase angle of the filter block can be calculated as

$$G_{filter}(\lambda_j) = G_{filter} \angle \varphi_{filter} \quad (3-30)$$

where  $G_{filter}$  and  $\varphi_{filter}$  are the magnitude and phase angle of  $G_{filter}(s)$  associated with  $\lambda_j$ ,

respectively.

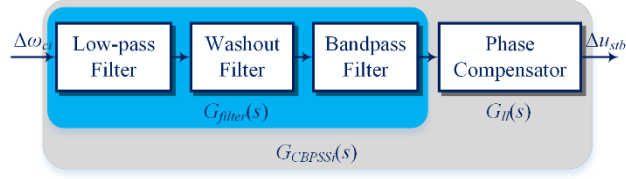


**Figure 3.8:** Structure of the CBPSS.

For the phase compensator, a lead-lag structure is adopted in this chapter, expressed as

$$G_{II}(s) = K_0 \cdot K_1 \frac{1+sT_2}{1+sT_1} \cdot K_2 \frac{1+sT_4}{1+sT_3} \quad (3-31)$$

where  $K_0$ ,  $K_1$ , and  $K_2$  are the gains of  $G_{II}(s)$ ;  $T_1$ ,  $T_2$ ,  $T_3$  and  $T_4$  are the time constants.

Based on (3-28), (3-29), and (3-30), to stabilize the  $j$ th oscillation mode of the microgrid, the phase compensator should satisfy

$$G_{II}(\lambda_j) = \frac{D_{stb}}{G_F G_{filter}} \angle -(\varphi_F + \varphi_{filter}) \quad (3-32)$$

Then, the parameters of the phase compensator can be determined by solving the following equations

$$K_1 \frac{1+T_2\lambda_j}{1+T_1\lambda_j} = K_2 \frac{1+T_4\lambda_j}{1+T_3\lambda_j} = 1 \angle -\frac{\varphi_F + \varphi_{filter}}{2} \quad (3-33)$$

$$K_0 = \frac{D_{stb}}{G_F G_{filter}} \quad (3-34)$$

With CBPSS parameters derived with the above-mentioned equations, the phase lag of the forward loop  $F_{stbi}(s)$  can be compensated accurately at the concerned mode  $\lambda_j$ , and thus a pure damping torque is generated by the proposed CBPSS to enhance the stability of the islanded microgrid.

---

## 3.4. Case Study

### 3.4.1. Modal Analysis

#### 1) Illustration of the proposed method.

The microgrid depicted in Fig. 3.1 is taken as an example to demonstrate the optimal location and design of the proposed CBPSS. As described in Section II, VSCs in the microgrid are modelled with 13<sup>th</sup>-order models, involving the dynamics of the power controller, the voltage and current controller, as well as the LC filter and coupling inductances. Then, by integrating the VSC subsystem (3-9), with the network subsystem (3-12), and load subsystems (3-13), a 47<sup>th</sup>-order microgrid model is yielded, written in the form as (3-15), and parameters employed to set up the microgrid state-space model are given in Table 3.1.

From the linearized microgrid model, 22 oscillation modes are observed via modal analysis, and they fall into four different clusters, as depicted in Fig 3.9. In the low-frequency part, the oscillation mode with an eigenvalue “ $\lambda_1 = -5.57 + j64.97$ ” is recognized as the critical mode, of which the damping ratio is only 8.53%, as signified by yellow circles in Fig. 3.9, and thus the proposed CBPSS will be designed to stabilize the critical mode.

To identify the optimal location of the CBPSS in the islanded microgrid, the eigenvalue mobilities of the critical mode  $\lambda_1$  regarding different VSCs of the microgrid are calculated with (3-24), and results are presented in Table 3.2. From Table 3.2, the sensitivities of various VSCs in the microgrid to the critical mode  $\lambda_1$  are different, and the eigenvalue mobility is the greatest when the VSC 2 is taken as the location of the CBPSS, with a value of  $1.59 \times 10^{-4}$ , which is 3 times greater than that with the CBPSS at VSC 1, or more than 30 times larger than that of the case with CBPSS at VSC 3. Therefore, VSC 2 is identified as the optimal location to install CBPSS for damping the mode  $\lambda_1$  for the microgrid.

**Table 3.1:** The Microgrid specification under study.

Parameter	Value
Voltage level	$U_{dc} = 1000 \text{ V}$ , $u_{abc} = 220 \text{ V}$ (RMS value)
LC filter	$L_{f1} = L_{f2} = L_{f3} = 1.35 \text{ mH}$ , $r_{f1} = r_{f2} = r_{f3} = 0.1 \text{ } \Omega$ , $C_{f1} = C_{f2} = C_{f3} = 50 \text{ } \mu\text{F}$
Coupling impedance	$L_{c1} = L_{c2} = L_{c3} = 0.35 \text{ mH}$ , $r_{c1} = r_{c2} = r_{c3} = 0.03 \text{ } \Omega$
Cut-off frequency	$\omega_{f1} = \omega_{f2} = \omega_{f3} = 31.41 \text{ rad/s}$
Active power droop	$m_{p1} = m_{p3} = 0.00047$ , $m_{p2} = 0.00094$
Reactive power droop	$n_{q1} = n_{q2} = n_{q3} = 0.00001$
Voltage control	$k_{pv1} = k_{pv2} = k_{pv3} = 0.05$ , $k_{iv1} = k_{iv2} = k_{iv3} = 390$
Current control	$k_{pc1} = k_{pc2} = k_{pc3} = 10.5$ , $k_{ic1} = k_{ic2} = k_{ic3} = 16000$
Network impedance	$L_{line1} = 0.32 \text{ mH}$ , $r_{line1} = 0.23 \text{ } \Omega$ , $L_{line2} = 1.85 \text{ mH}$ , $r_{line2} = 0.35 \text{ } \Omega$
Load	$L_{load1} = 5 \text{ mH}$ , $r_{load1} = 25 \text{ } \Omega$ , $L_{load2} = 5 \text{ mH}$ , $r_{load2} = 20 \text{ } \Omega$

Then, with the CBPSS installed at VSC 2, the angular speed of VSC 2,  $\Delta\omega_{c2}$ , is taken as the input of the CBPSS, and the output stabilizing signal  $u_{stb2}$  of the CBPSS is imposed on the reactive power control loop of VSC 2 to damp the critical mode, as illustrated in Fig. 3.4. Following the procedures presented in Section III and by substituting  $\lambda_1$  into (3-27), the magnitude and phase lag of the forward loop  $F_{stb2}$  regarding  $\lambda_1$  is recognized as  $F_{stb2}(\lambda_1) = 535.65 \angle 6.18^\circ$ .

Thus, the phase angle of  $G_{CBPSS}(s)$  should be designed as  $-6.18^\circ$ , so that the phase lag of  $F_{stb2}(\lambda_1)$  can be fully fixed, and consequently a pure damping torque will be synthesized to stabilize the critical mode. For the desired damping  $D_{stb}$  contributed by the CBPSS, as

shown in (3-29), a method is given in [125] to estimate the order of magnitude of  $D_{stb}$ , and in this chapter,  $D_{stb}$  is set to be 1800. Then, following the design objective (3-29), and by solving (3-33) and (3-34), parameters of the proposed CBPSS is calculated and listed in Table 3.3.

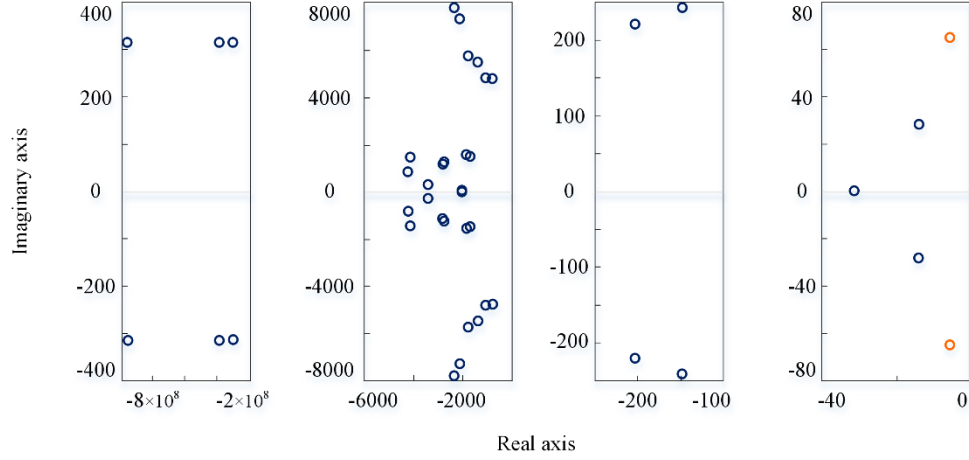


**Figure 3.9:** Pole map of the microgrid without CBPSS.

**Table 3.2:** Eigenvalue mobility of VSCs to the critical mode  $\lambda_1$ .

	PSS @ VSC 1	PSS @ VSC 2	PSS @ VSC 3
Eigenvalue mobility	$4.68 \times 10^{-5}$	$1.59 \times 10^{-4}$	$4.29 \times 10^{-6}$

**Table 3.3:** CBPSS parameters when installed at VSC 2.

Parameter	Description	Value
$\omega_{bp}$	Bandpass filter center frequency	64.97 rad/s
$\omega_{lp}$	Low-pass filter cut-off frequency	64.97 rad/s
$T_w$	Washout filter time constant	5 s
$K_0$	Gain of lead-lag compensator	3.78
$K_1, K_2$	Gain of lead-lag compensator	0.7317
$T_1, T_3$	Lead-lag compensator time constant	0.01 s
$T_2, T_4$	Lead-lag compensator time constant	0.0198 s



## 2) Verification of the CBPSS optimal location.

Taking the CBPSS equipped at VSC 2 into consideration, the microgrid open-loop model (3-15) turns into a closed-loop system, as depicted in Fig. 3.6, and the critical mode eigenvalue  $\lambda_1$  associated with the closed-loop system is calculated and given in Table 3.4. Besides, to illustrate the effectiveness of eigenvalue mobility in identifying the CBPSS optimal installation location, the closed-loop eigenvalues when the CBPSS is deployed at VSC 1 or VSC 3 are also calculated and illustrated in Fig. 3.10, and also summarized with damping ratios in Table 3.4.

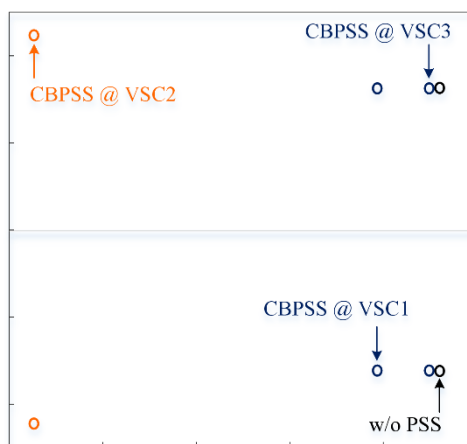


**Figure 3.10:** Critical mode eigenvalue distribution with the CBPSS equipped at VSC 1, VSC 2, and VSC 3.

It should be noted that when the CBPSS is deployed at VSC 1 or VSC 3, the parameters of the associated CBPSS are designed separately with the same procedure as the case of CBPSS installed at VSC 2, and to ensure a fair comparison, the same desired damping  $D_{stb}$  is set when the CBPSS is placed at different VSCs.

From Table 3.4, the damping ratio of the critical mode  $\lambda_1$  is enhanced with the proposed CBPSS, no matter the CBPSS is installed at VSC 1, VSC 2, or VSC 3, and thus the stability of the overall microgrid is enhanced. Nonetheless, when the CBPSS is placed at different VSCs, the damping ratio improvement differs, and with the CBPSS equipped at the

identified optimal location, e.g., VSC 2, the greatest damping ratio enhancement of the critical mode from 8.53% to 24.90% is witnessed from Table 3.4, and correspondingly  $\lambda_1$  is shifted from “ $-5.57 + j64.97$ ” to “ $-22.92 + j89.13$ ”. However, when the CBPSS is placed at VSC 1 or VSC 3, the improvement of the critical mode damping ratio is not as effective as that in the case of VSC 2, and the damping ratio of  $\lambda_1$  is only boosted from 8.53% to 12.62% or 9.25%, respectively.

**Table 3.4:** Eigenvalues with CBPSSs installed at different VSCs.

	Eigenvalue $\lambda_1$	Damping ratio
w/o CBPSS	$-5.57 + j64.97$	8.53%
CBPSS @ VSC 1	$-8.24 + j64.76$	12.62%
<b>CBPSS @ VSC 2</b>	<b><math>-22.92 + j89.13</math></b>	<b>24.90%</b>
CBPSS @ VSC 3	$-6.01 + j64.77$	9.25%

Thus, based on the consistency between the damping ratio improvement as demonstrated in Table 3.4 and the eigenvalue mobility results listed in Table 3.2, the effectiveness of the presented eigenvalue mobility method in identifying the CBPSS optimal location is confirmed.

The phase portraits of the  $dq$ -axis output currents of VSC 1, VSC 2, and VSC 3 under the circumstance of without CBPSS, CBPSS installed at VSC 1, VSC 2 and VSC 3 are also illustrated in Fig. 3.11. From Fig. 3.11, it is demonstrated that when the proposed CBPSS installed at different VSCs, the effect on improving stability also varies, even though the CBPSS is designed following the same procedure. When the CBPSS is installed at VSC 2, the system converges to the new equilibrium point quickly with few oscillations. However, when the proposed CBPSS is installed at VSC 1 or VSC 3, the effectiveness of the improving stability is not as significant as the case with VSC 2, and the system takes a longer time to reach the new equilibrium point. When comparing the phase portrait of the cases with the CBPSS installed at VSC 1 or VSC 3 with the case without the CBPSS, it can be found that the improvement in the post-disturbance dynamic response is very limited. As a result, the optimal location of the CBPSS is proved.

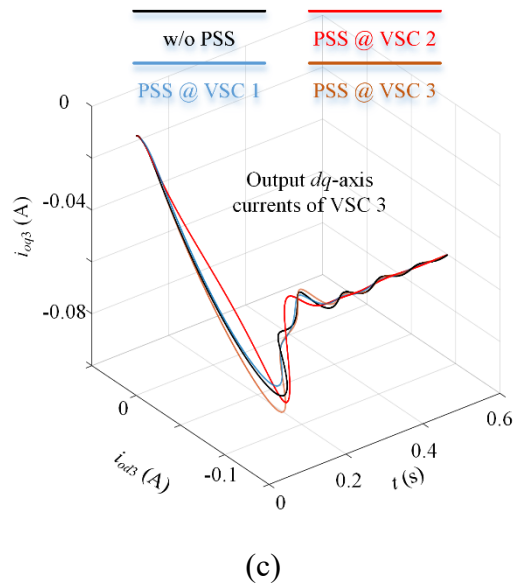
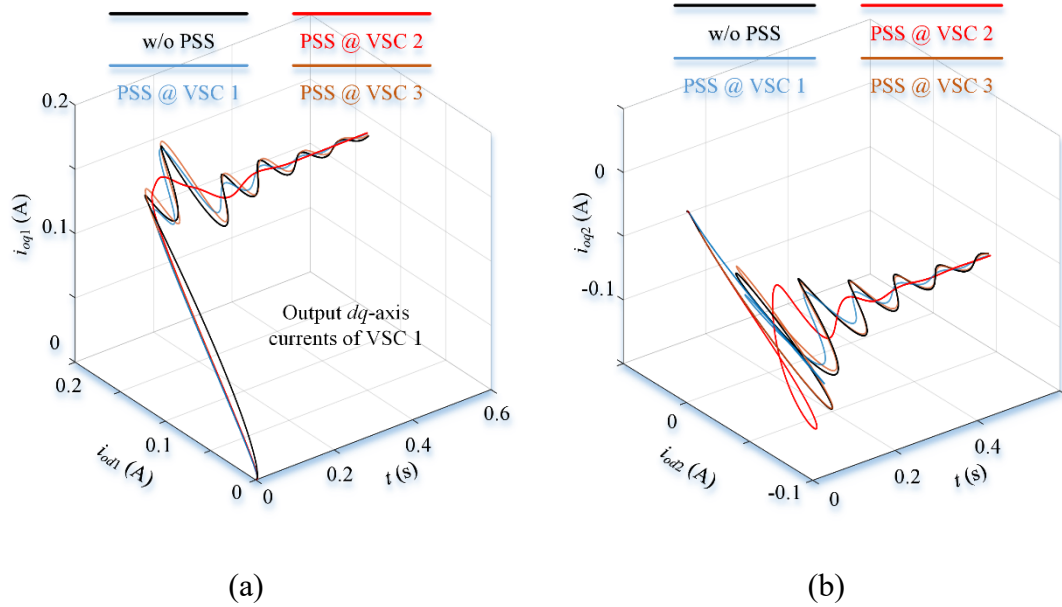


**Figure 3.11:** Phase portrait of VSC output currents with the CBPSS equipped on different VSCs. (a)  $dq$ -axis output currents of VSC 1. (b)  $dq$ -axis output currents of VSC 2. (c)  $dq$ -axis output currents of VSC 3.

Besides, when the CBPSS is placed at VSC 2, the complete closed-loop eigenvalue distribution is portrayed in Fig. 3.12. Comparing Fig. 3.12 with Fig. 3.9, only the eigenvalues associated with the critical mode are shifted to the left side by the CBPSS, as

indicated by yellow circles in Fig. 3.12 and Fig. 3.9, while other oscillation modes remain almost unaffected. This fact exhibits the effectiveness of the bandpass filter in the designed CBPSS, and it contributes to eliminating interactions between the CBPSS with other unconcerned microgrid oscillation modes. As a result, only the dynamics of the critical mode are influenced by the proposed CBPSS, preventing potential adverse impacts on other oscillation modes of the microgrid.

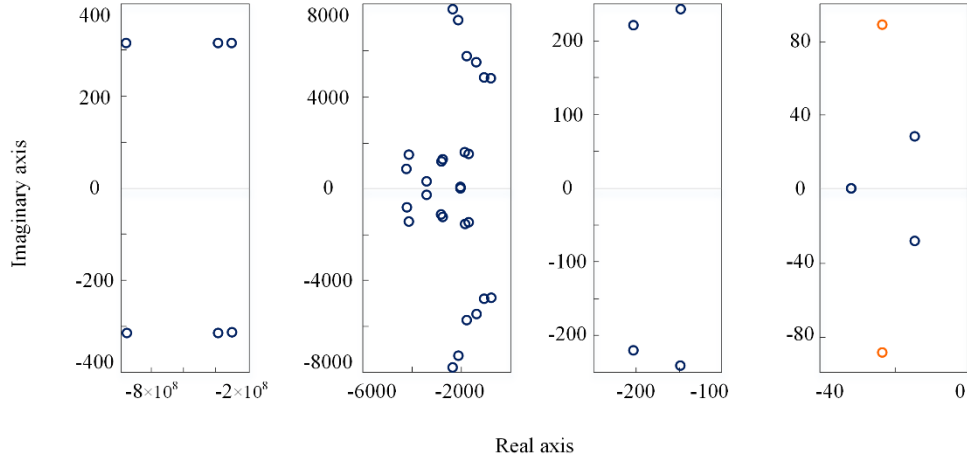


**Figure 3.12:** Pole map of the microgrid with CBPSS placed at VSC 2.

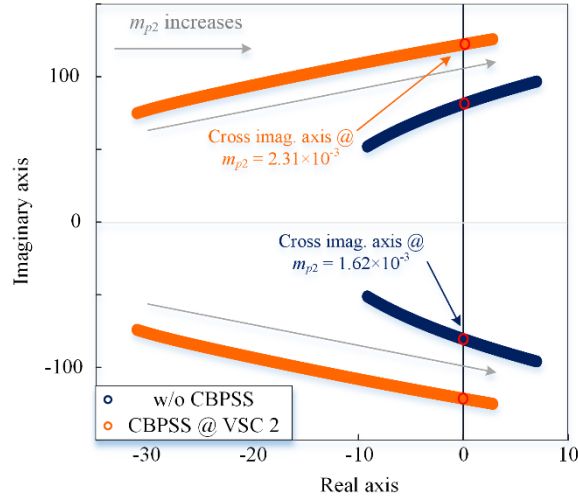
### 3) Expansion of the stability margin.

The effect of the proposed CBPSS in expanding the microgrid stability margin is examined in this part. For the critical mode  $\lambda_1$ , participation factor analysis [126, 127] is carried out to recognize the parameter that has crucial impacts on its dynamic, and the results are given in Table 3.5.

It is obtained from Table 3.5 that the critical mode is principally dominated by the state variables of the power control associated with VSC 2, accounting for 66.55% of total participation of the mode  $\lambda_1$ . Therefore, the stability of the mode  $\lambda_1$  is checked with the change of  $m_{p2}$ , e.g., the active power droop gain of VSC 2, while other conditions remain the same as Table 3.1. The root locus of the critical mode eigenvalue  $\lambda_1$  corresponding to the microgrid with and without the CBPSS placed at VSC 2 is depicted in Fig. 3.13.

**Table 3.5:** Participation factors of the critical mode  $\lambda_1$ .

	Power control	Inner control	Filter
VSC 1	15.95%	1.77%	2.23%
VSC 2	<b>66.55%</b>	3.02%	3.78%
VSC 3	3.21%	0.16%	0.02%

**Figure 3.13:** Root locus with the change of  $m_{p2}$ .

From Fig. 3.13, with the increase of  $m_{p2}$ , the eigenvalues  $\lambda_1$  move toward the right side in both cases with and without the CBPSS in the microgrid, indicating a reduced stability of the overall microgrid with the increase of the active droop gain. However, given the same  $m_{p2}$ , with the CBPSS deployed at VSC 2, the eigenvalues always locate on the left side compared with that of the case without the CBPSS applied, indicating an enhanced microgrid stability with the help of the CBPSS, which is consistent with the results in Table 3.4.

Besides, with the CBPSS involved in the microgrid, the stability margin of the microgrid is enlarged. From Fig. 3.13, without the CBPSS, the eigenvalues  $\lambda_1$  enter the right half plane when  $m_{p2}$  is larger than “ $1.62 \times 10^{-3}$ ”, while with the proposed CBPSS in the microgrid, the eigenvalues  $\lambda_1$  do not cross imaginary axis until  $m_{p2}$  exceeds “ $2.31 \times 10^{-3}$ ”.

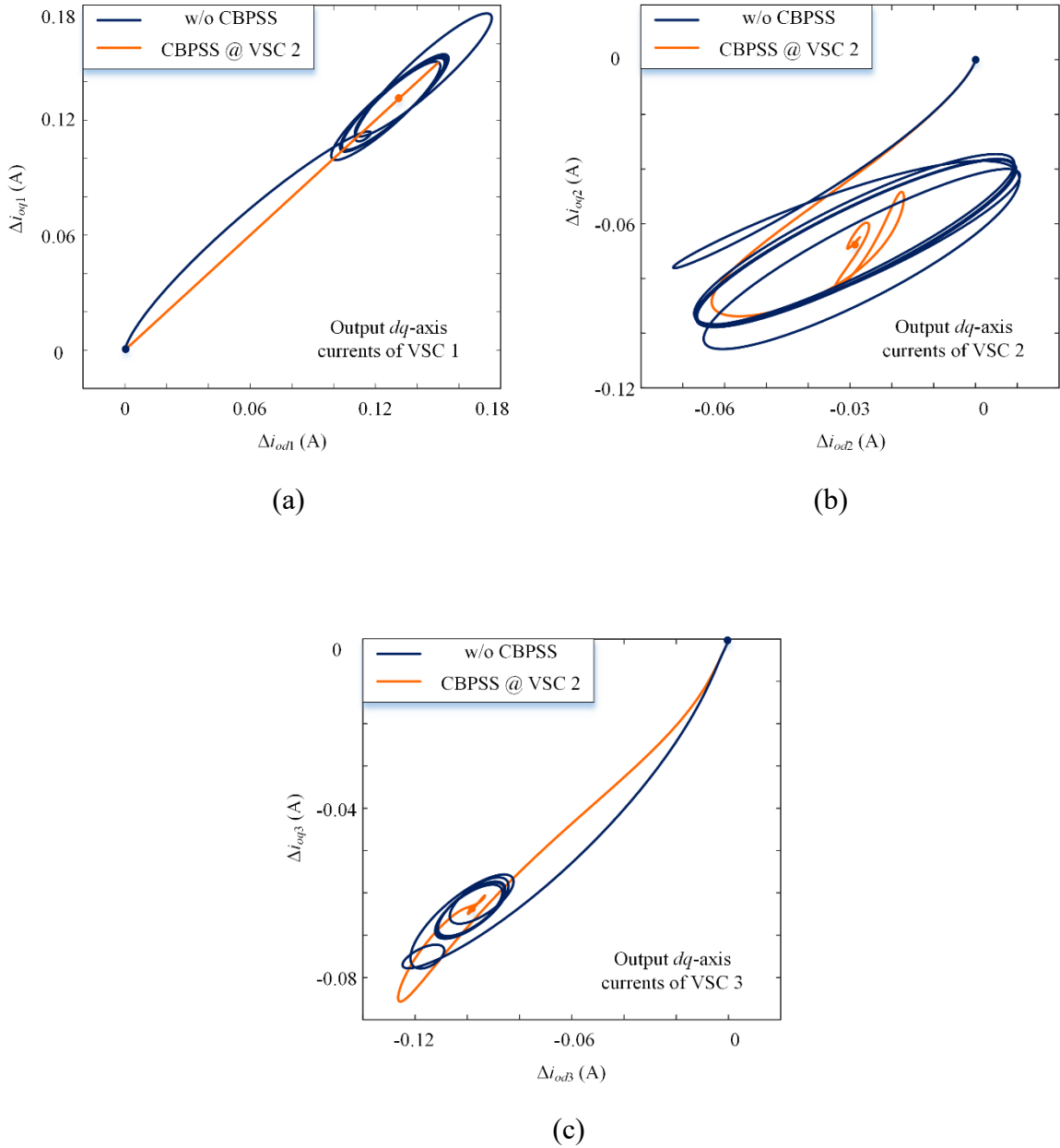


**Figure 3.14:** System phase portrait on the  $(\Delta i_{odi}, \Delta i_{oqi})$ -plane with the CBPSS installed on VSC 2. (a) output  $dq$ -axis currents of VSC 1. (b) output  $dq$ -axis currents of VSC 2. (c) output  $dq$ -axis currents of VSC 3.

---

The system phase portrait on the  $(\Delta i_{od}, \Delta i_{oq})$ -planes of VSC 1, VSC 2, and VSC 3, starting from the microgrid equilibrium point, are depicted in Fig. 3.14 to confirm the effect of the CBPSS in expanding the microgrid stability margin. In both the cases with and without the CBPSS applied in the microgrid, the value of  $m_{p2}$  is set to be “ $1.62 \times 10^{-3}$ ”.

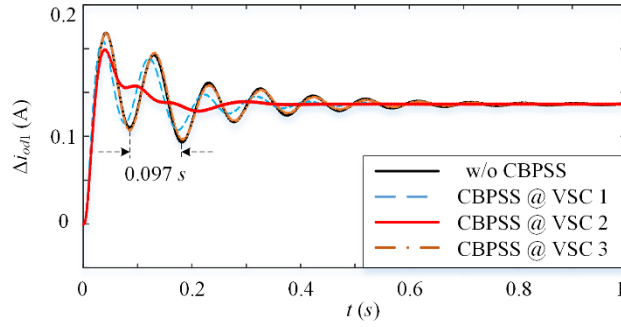
From Fig. 3.14, in the case without the CBPSS deployed in the microgrid, since the stability boundary of the microgrid is touched, as illustrated in Fig. 3.13, the system phase portrait cannot converge to the equilibrium point, and an oscillatory limit cycle is observed on the  $(\Delta i_{od}, \Delta i_{oq})$ -planes of VSC 1, VSC 2, and VSC 3. However, with the designed CBPSS placed at VSC 2 of the microgrid, the microgrid phase portrait initially unfolds in an oscillatory manner but eventually converges to the equilibrium point after a period of oscillation, displaying the characteristic of a stable system on the  $(\Delta i_{od}, \Delta i_{oq})$ -planes of VSC 1, VSC 2, and VSC 3. Therefore, it is proved that the microgrid stability margin is enlarged with the proposed CBPSS, and the CBPSS is capable of turning the oscillatory instable microgrid into a stable one.

### 3.4.2. Time-Domain Simulations

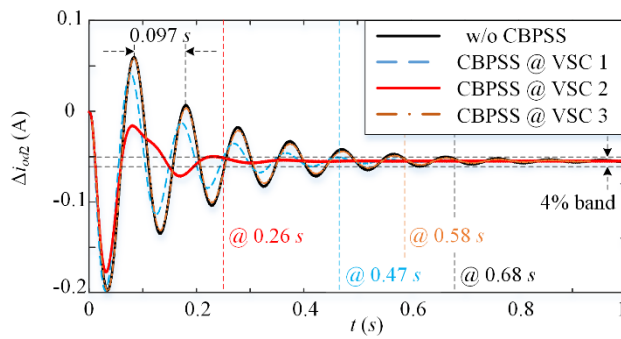
Time-domain simulations are carried out to verify the effectiveness of the proposed CBPSS in boosting the stability of the microgrid. The microgrid in Fig. 3.1 is established in Matlab/Simulink with detailed nonlinear models, and the parameters of the microgrid refer to Table 3.1.

#### 1) Microgrid stability enhancement with the proposed CBPSS.

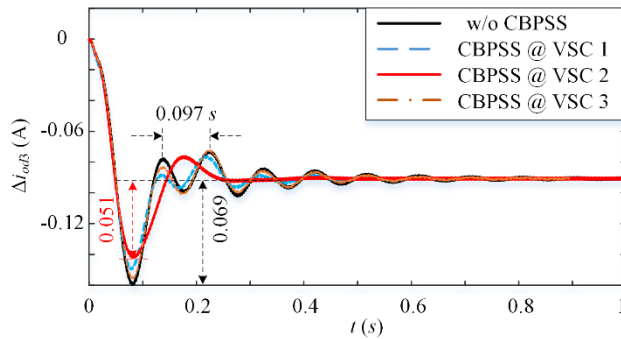
The effect of the proposed CBPSS is demonstrated in this part, and a 5% step-up change of the VSC 1 power reference is activated at  $t = 0$  s as perturbation. Four different scenarios are considered, e.g., without CBPSS in the microgrid, CBPSS placed at VSC 1, CBPSS deployed at VSC 2, and CBPSS installed at VSC 3.



(a)



(b)



(c)

**Figure 3.15:** Effect of the proposed CBPSS in suppressing microgrid oscillations. (a)  $d$ -axis output current of VSC 1. (b)  $d$ -axis output current of VSC 2. (c)  $d$ -axis output current of VSC 3.

It should be noted that when the CBPSS is deployed at VSC 2, its parameters are given in Table 3.3; the parameters of the CBPSS when placed at VSC 1 or VSC 3 are derived



---

following the procedures in Section 3.4. The same  $D_{stb}$  in (3-29) is applied within different scenarios, so that a fair comparison is guaranteed among scenarios with different CBPSS locations. The  $d$ -axis output currents of VSC 1, VSC 2, and VSC 3 are taken as examples to demonstrate the effect of the proposed CBPSS on the microgrid dynamic responses, as shown in Fig. 3.15.

From Fig. 3.15, the oscillation frequency of the microgrid in the time-domain simulation is 64.78 rad/s ( $2\pi/0.097$  rad/s), which is almost the same as the angular frequency of the critical mode identified from modal analysis, e.g., " $\lambda_1 = -5.57 + j64.97$ ". Thus, the accuracy of the derived mode is verified.

Besides, from Fig. 3.15, the microgrid dynamic responses are improved with the proposed CBPSS, no matter it is deployed at VSC 1, VSC 2, or VSC 3, thus proving the effectiveness of the proposed CBPSS in enhancing the stability of the microgrid. However, when the CBPSS is installed at different VSCs in the microgrid, different effects in suppressing oscillations are witnessed.

With the CBPSS deployed at the previously identified optimal location, e.g., VSC 2, it is observed that the post-disturbance oscillations are well suppressed: the settling time declines from 0.68 s to 0.26 s as shown in Fig. 3.15(b), signifying a 57% reduction, and the oscillation amplitude is also reduced, as depicted in Fig. 3.15(c). Nonetheless, when the CBPSS is deployed at VSC 1 or VSC 3, the impacts on oscillation suppression effect are not so compelling as that of the VSC 2 case. This is especially true for the scenario when the CBPSS is installed at VSC 3, which has an eigenvalue mobility only one thirtieth of that of VSC 2, as demonstrated in Table 3.2, the post-disturbance curves almost overlap with that of the case without CBPSS in microgrid as shown in Fig. 3.15, and little contribution is observed in improving the dynamic responses. This phenomenon again verifies that in a microgrid, some VSCs are insensitive to the certain oscillation mode, and thus deploying CBPSS on these insensitive VSCs has little contribution in improving the microgrid stability, but only increasing control complexity. As a result, the effectiveness of the method in identifying optimal installation location is validated from Fig. 3.15.

## 2) Microgrid stability margin expansion with the proposed CBPSS.

The effect of the CBPSS on expanding the microgrid stability margin is illustrated in this part, and  $m_{p2}$  is set to be “ $1.88 \times 10^{-3}$ ” in simulations, while other parameters remain unchanged as Table 3.1. From  $t = 0$  to  $1$  s, the microgrid operates with the CBPSS equipped at VSC 2, and then at  $t = 1$  s the CBPSS deployed at VSC 2 is switched off. The  $d$ -axis output current of VSC 1 is portrayed in Fig. 3.16.

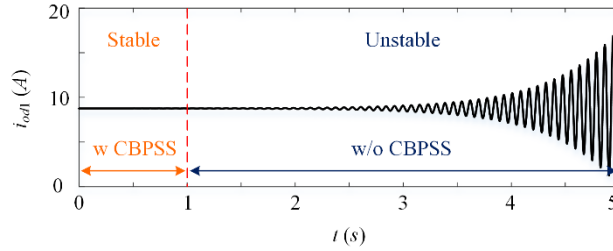


**Figure 3.16:** Expanded microgrid stability margin with the proposed method.

From Fig. 3.16, in the time period with the CBPSS, the microgrid operate stably, and the  $d$ -axis output current of VSC 1 is steady and constant. However, when the CBPSS is switched off, since the microgrid stability boundary is crossed, as illustrated in Fig. 3.13, oscillatory instability is observed in the  $d$ -axis output current of VSC 1, and finally the whole islanded microgrid loses stability. Therefore, it is validated that the application of the CBPSS enlarges the microgrid stability margin, and when the CBPSS is switched off from the islanded microgrid, instability occurs.

### 3.4.3. Experimental Verification

In addition to simulation results, experimental results from a scaled-down microgrid prototype are also provided for verification. Fig. 3.17 shows the picture of the laboratory setup, where the digital controls are implemented with a RT Box. Due to the limited PWM channels, we can only conduct hardware experiments for two three-phase VSCs. Since the presented CBPSS design method in Section III is derived based on a multiple-VSC

microgrid, therefore the effectiveness of the proposed method is still valid for multiple-VSC situations. The diagram of the laboratory prototype is depicted in Fig. 3.1, and the parameters of the hardware experiments are given in Table 3.6. Following the CBPSS design method detailed in the previous sections, the parameters of the CBPSS are obtained, demonstrated in Table 3.7.

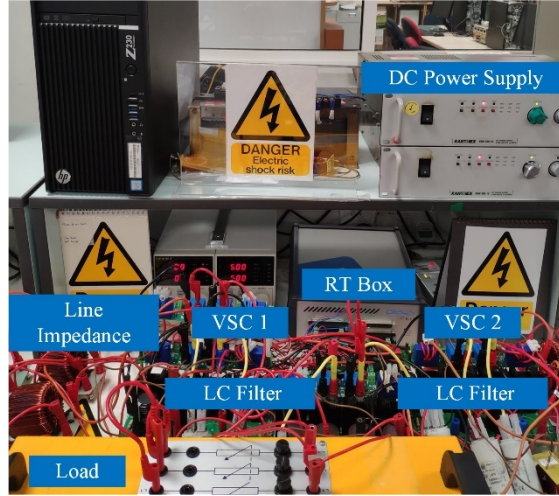


**Figure 3.17:** Photo of the laboratory prototype setup.

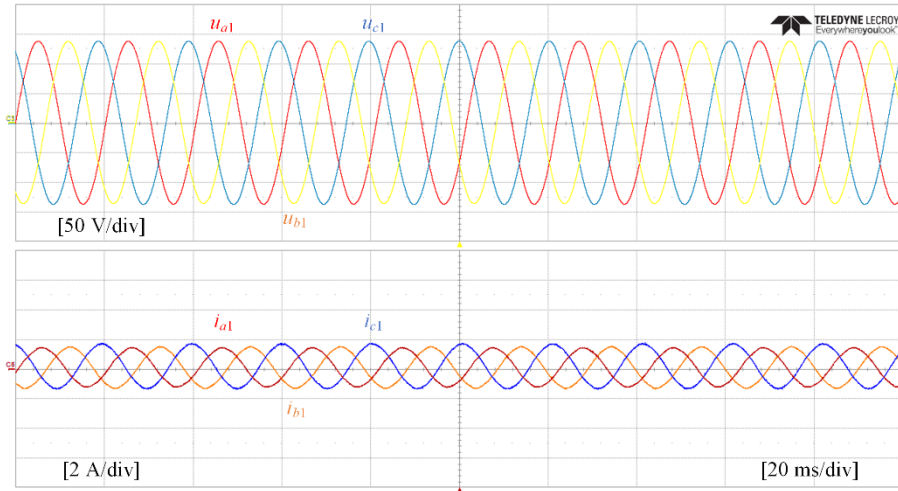
**Table 3.6:** Hardware experiment parameters.

Parameter	Value
Voltage level	$U_{dc1} = 300 \text{ V}$ , $u_{abc1} = 100 \text{ V}$ (RMS value); $U_{dc2} = 300 \text{ V}$ , $u_{abc2} = 100 \text{ V}$ (RMS value)
LC filter	$L_{f1} = 1 \text{ mH}$ , $C_{f1} = 15 \text{ } \mu\text{F}$ ; $L_{f2} = 1 \text{ mH}$ , $C_{f2} = 15 \text{ } \mu\text{F}$
Coupling impedance	$L_{c1} = 2 \text{ mH}$ , $L_{c2} = 1 \text{ mH}$
Network impedance	$L_{line} = 1 \text{ mH}$
Load	$r_{load} = 35 \text{ } \Omega$

**Table 3.7:** CBPSS parameters in hardware experiments.

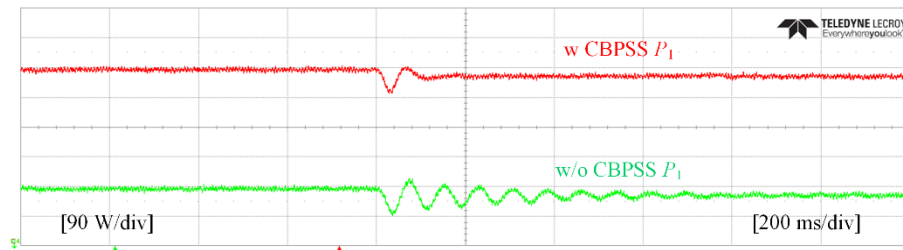
Parameter	Description	Value
$\omega_{bp}$	Bandpass filter center frequency	82.24 rad/s
$\omega_{lp}$	Low-pass filter cut-off frequency	82.24 rad/s
$T_w$	Washout filter time constant	5 s
$K_0$	Gain of lead-lag compensator	1.05
$K_1, K_2$	Gain of lead-lag compensator	0.9
$T_1, T_3$	Lead-lag compensator time constant	0.01 s
$T_2, T_4$	Lead-lag compensator time constant	0.0114 s

Fig. 3.18 demonstrates the steady-state three-phase voltage and current waveforms of VSC 1, and it can be observed that these three-phase waveforms are sinusoidal, and thus it is proved that the proposed CBPSS does not affect the normal operations of the islanded microgrid. In experiments, the disturbance is set to be a 10% step-down change of the power reference of VSC 1; the proposed CBPSS is designed following the method presented in Section III and installed on VSC 2, with its parameters detailed in Appendix. The post-disturbance power of VSC 1 with and without the proposed CBPSS installed on VSC 2 are depicted in Fig. 3.19.



**Figure 3.18:** Steady-state voltage and current waveforms.

In Fig. 3.19, with the CBPSS, the oscillations in the post-disturbance power of VSC 1 are well suppressed. However, without the proposed CBPSS, the output power of VSC 1 takes about 0.70 s to reach steady state, while with the proposed CBPSS, it only takes around 0.15 s to reach steady state, indicating a 78% reduction in term of settling time with the help of the CBPSS. Therefore, the practical feasibility and effectiveness of the proposed CBPSS in enhancing the stability of islanded microgrids is validated.



**Figure 3.19.:** Post-disturbance power and current waveforms.

### 3.5. Summary

In this chapter, a supplementary control loop, e.g., CBPSS, is proposed for droop-controlled islanded microgrids to enhance the stability in the face of disturbances. Firstly, the forward loop from the CBPSS to the given islanded microgrid is recognized, and then by use of the identified forward loop, the CBPSS parameters are designed accordingly to compensate the phase lag of the forward loop, and consequently an additional damping torque is generated to improve the stability of the islanded microgrid. Besides, an eigenvalue-mobility based approach is also presented to guide the selection of the optimal installation location for the proposed CBPSS in the islanded microgrid, and as a result, the greatest stabilizing effect can be achieved with the least controller design effort. The developed CBPSS features rigorous theoretical derivation and clear physical mechanism, and its effectiveness is verified with modal analysis and time-domain simulations. Hardware-based experiments are also conducted in a scaled-down laboratory prototype to show the practical feasibility and effectiveness of the proposed method.



---

## Chapter 4

### **Stability Issue Associated with Constant Power Loads for Power-Electronic-Dominated Power Systems**

*The instability caused by CPLs for power-electronic-dominated power systems is focused in this chapter. The tightly regulated power converters behave as CPLs, featuring negative incremental impedance and introducing adverse impacts on the stability of power-electronic-dominated power systems. Moreover, with the increase of the power level of CPLs, such adverse effects also grow, and finally, it may trigger instability, threatening the security and reliability of the whole system. Then, participation factor analysis demonstrate that voltage controllers of power converters principally dominate such instability, with a typical response time of dozens of milliseconds. In light of such instability problem, two control schemes, e.g., a damper-based scheme and a stabilizer-based scheme, are proposed to handle the instability issue associated with CPLs. The effectiveness of the proposed methods is verified with case studies.*

---

## 4.1. Introduction

The more electric aircraft (MEA) is a promising concept and tendency in modern aerospace industry with merits of improved energy efficiency and reduced maintenance costs [128, 129], and a large number of power electronic converters are employed in MEAs to perform energy conversion and realize flexible control between different power stages [130]. However, tightly regulated power converters in MEAs behave as CPLs, featuring negative incremental impedance [131]. In turn the negative impedance characteristic of CPLs can upset the stability of the interconnected energy conversion stages and even lead to system shutdown, threatening the safety of MEAs [132].

To settle this issue, studies have been carried out to alleviate the instability regarding CPLs. For CPLs in DC applications, different measures have been presented to handle the induced instability problem. In [133], bifurcation analysis is carried out for DC interconnected systems, and the CPL instability is addressed through a sliding mode controller for bidirectional boost converters, and a linear controller is demonstrated in [134] for stabilizing buck converters connecting with CPLs. For DC microgrids integrated with CPLs, a power buffer-based scheme is presented in [135] and a nonlinear disturbance observer-based scheme is developed in [136] to address the unfavorable influence. However, different from DC grids, for AC grids such as the onboard power systems in MEAs, there is no DC steady-state operating point [115]. Park transformation in [115] and harmonic linearization technique in [137, 138] are applied to translate an AC system into two equivalent DC channels. Nonetheless, studies in [139, 140] demonstrate strong coupling between the two equivalent DC channels, and thus the transferred equivalent DC channels cannot be treated as two independent DC circuits. As a result, the well-established stability control approaches for CPLs in DC systems cannot be simply transplanted into AC scenarios.

In view of the significant difference between CPLs in DC and AC applications, several attempts have been conducted to solve the instability problem with CPLs in AC grids. Stability analysis in [117, 141] illustrates that the mismatch of voltage control bandwidths



---

between source and load converters can exaggerate the negative effect of CPLs, making the system more prone to lose stability, and a coordinated parameter design approach is presented accordingly to mitigate the instability regarding CPLs. Passive stabilization method through circuit modification, such as adopting large filter capacitors or adding extra passive components, is presented in [142] with verified effectiveness in suppressing CPL induced oscillations. Although simple and straightforward, the passive approach is bulky in size and thus not applicable to MAEs due to space limit. In [143], a converter-based damping agent is designed so that the circuit impedances can be reshaped dynamically to offset the negative impedance of CPLs. However, the developed damping agent requires the employment of an additional converter, which is costly and also incurs extra power losses.

Recently, the model predictive control (MPC) [144] also shows potential in dealing with CPL-induced instability in AC grids. By adding a stability-associated penalty term in cost functions, the regulation objectives of MPC can be extended to cover the stability control for CPLs. To be specific, [145] combines the modulated MPC with a dichotomy algorithm so that better system dynamic response can be achieved. A Lyapunov stability criteria-based cost function is constructed in [146] to guarantee the stability of DC-link voltage in the face of CPLs. Moreover, a deadbeat approach together with an indirect voltage control scheme is developed in [147] to optimize the transient performance. However, since MPC is conducted by iteratively searching the optimal switching vectors during each limited sampling period to minimize the cost function, imposing extra stabilizing objectives into the cost functions escalates the computation burden for MPC algorithms. As a result, a higher requirement is posed for digital processors, incurring additional capital investment [148]. Besides, there is a tradeoff between the stabilizing control objective and the routine voltage and harmonic control objectives in the cost functions of MPC, yielding compromised voltage and harmonic regulation performance.

In contrast to the MPC-based method which relies on intensive iterative computation, linear control approaches feature simple structures and good compatibility with the commonly used cascaded control architectures for power converters [35]. In [149, 150], a virtual

---

impedance approach is applied to the load-side converters so that the oscillations resulted from CPLs can be well suppressed. Nonetheless, the load-side stability control will modify load operating characteristics, and the virtual impedance deteriorates the performance of the steady-state voltage regulation. In [151], a loop cancellation method based on DC voltage feedback is applied to the source-side converters, and the control gain is adaptively tuned to match different CPL power levels. Although there is no impact on load characteristic, a derivative term is involved in the stability control loop, which is sensitive to noise and may raise other stability concerns in practical use.

In light of these technical gaps, the CPL-induced instability in AC grids is focused in this chapter, and two different stability enhancement approaches are developed accordingly to improve the stability of an AC grid in the face of CPL, e.g., a damper-based scheme and a stabilizer-based scheme. The remainder of this chapter is organized as follows. The CPL induced instability in AC grids is illustrated first. Then, with modal analysis, it is found that the critical mode, which is destabilized significantly by the increase of CPL power level in AC grids, is principally denominated by the state variables associated with the voltage controllers of the source and load side converters. To handle the problem of CPL induced instability, the similarity between the integral part of voltage controller and motion equation of synchronous generators is demonstrated. After that, based on such similarity, different stability enhancement approaches are developed to enhance system stability in face of CPL via synthesizing additional damping torques. The effectiveness of the proposed approaches is validated with case studies.

## **4.2. Instability Problem Induced by CPLs**

### **4.2.1. System under Study**

Fig. 4.1 illustrates a gearbox-less configuration for electrical systems on MEAs, in which a generator is connected directly to the shaft of the MEA's turbine, serving as the main

power source, and the output of the generator has a variable frequency depending on the operating speed of the turbine. By removing the gearbox in this configuration, the reliability of the whole system is improved. Nonetheless, power converters (AC/DC and DC/AC) are required so that the variable-frequency output from the generator is transferred to the output with a fixed frequency of 400 Hz, for the MEA's electrical system. Besides, a battery is commonly deployed on MEAs, acting as the backup source to supply critical loads in case of emergency.

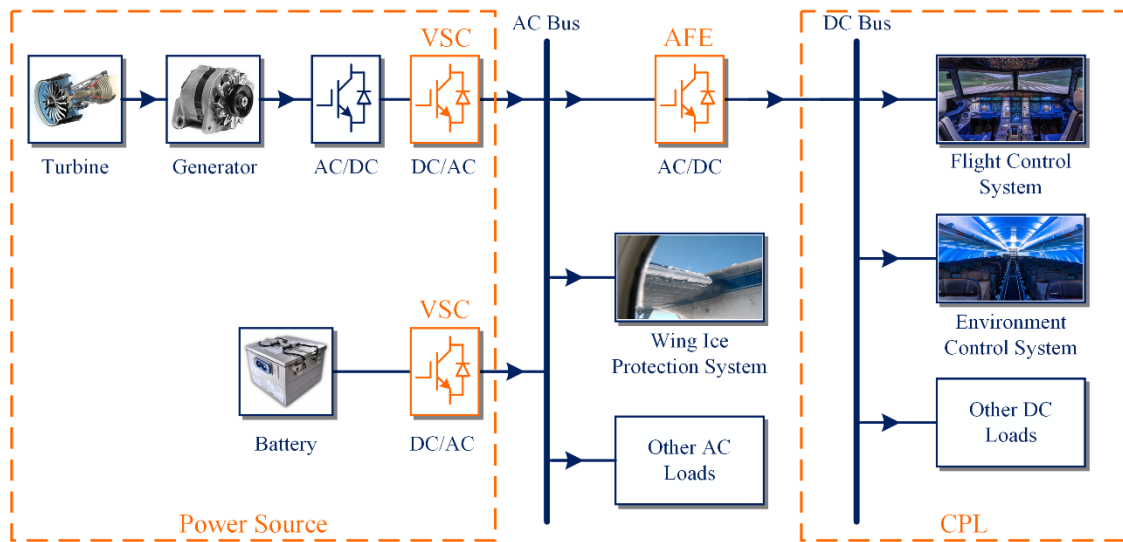


**Figure 4.1 :** A gear-less configuration for the power system on MEA.

As displayed in Fig. 4.1, AC loads and DC loads cohabit on MEAs. Different kinds of AC loads are supplied by the AC bus, of which the most important one is the wing ice protection system. Besides, an active front-end (AFE) is employed to realize power conversion from AC side to DC side to supply the MEA's DC loads, and a DC-link capacitor is deployed on the DC side of the AFE so that ripples can be significantly reduced, producing a smooth and constant DC-side voltage. Typical DC loads on MEAs include the flight control system and the environment control system, and these DC loads can be considered as CPLs, which display the characteristic of negative incremental impedance and deteriorate the overall stability of the whole MAE electrical system.

To highlight the instability problem resulted from CPLs and reduce the complexity of analysis for the MEA electrical system, a simplified electrical system is taken as an example, as shown in Fig. 4.2, consisted with a VSC and an AFE. The power source of the MEA electrical system is equivalently denoted by a voltage source converter (VSC), and the VSC is controlled to output constant three-phase sinusoidal voltages with a fixed frequency of 400 Hz. An AFE is employed to convert AC power to DC power and supply the CPL.

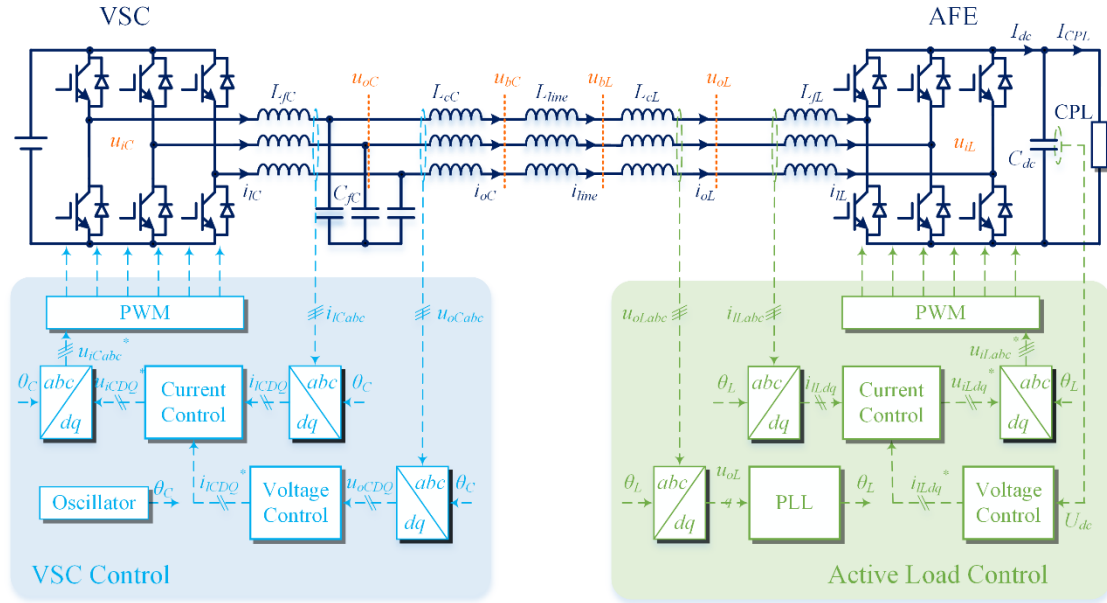


**Figure 4.2 :** Equivalent MEA electrical system.

In Fig. 4.2,  $L_{fc}$  and  $C_{fc}$  are the filter inductor and capacitor of the VSC, respectively.  $L_{cc}$  signifies the VSC-side coupling inductance.  $L_{line}$  is the connecting line between the VSC and the AFE, and  $L_{cl}$  stands for the AFE-side coupling inductance.  $L_{fl}$  denotes the filter inductor of the AFE.  $u_{iC}$  and  $u_{iL}$  are the terminal voltage of the VSC and the AFE, respectively.  $u_{oC}$  signifies the output voltage of the VSC, while  $u_{oL}$  denotes the input voltage of the AFE. Besides, for the ease of modeling, two bus voltages, e.g.,  $u_{bC}$  and  $u_{bL}$ , are defined, signifying the VSC-side and AFE-side bus voltages, respectively, as shown in Fig. 4.2.  $i_{iC}$  and  $i_{oC}$  stand for the currents flowing through  $L_{fc}$  and  $L_{cc}$ , respectively;  $i_{iL}$  and  $i_{oL}$  represent the currents flowing through  $L_{fl}$  and  $L_{cl}$ , respectively.  $i_{line}$  is the current flowing through the connecting line. On the DC side of the AFE,  $U_{dc}$  is the voltage across

the DC-link capacitor;  $I_{dc}$  is the input current into the DC part of the AFE, and  $I_{CPL}$  denotes the input current into the CPL.

Both the VSC and the AFE are controlled on synchronous  $dq$  frames, and the commonly used cascaded control architecture is employed in regulating their terminal voltages and currents. For the VSC, an oscillator is employed to produce a constant angle reference  $\theta_C$ , so that the output frequency of the VSC is fixed at 400 Hz.  $u_{oC}$  is measured and processed in the outer voltage controller of the VSC to generate the current reference for the inner current controller, and  $i_{IC}$  is measured and regulated in the current controller to generate the voltage reference for PWM. For the AFE, a PLL is adopted to synchronize the AFE with the VSC and generate the angle reference  $\theta_L$ . The DC-link voltage  $U_{dc}$  is measured and then regulated in the outer voltage controller, so that  $U_{dc}$  is tightly controlled to track its reference.  $i_{LL}$  is controlled in the inner current controller of the AFE to generate the terminal voltage reference for PWM.

### 1) . Coordinated transformation.

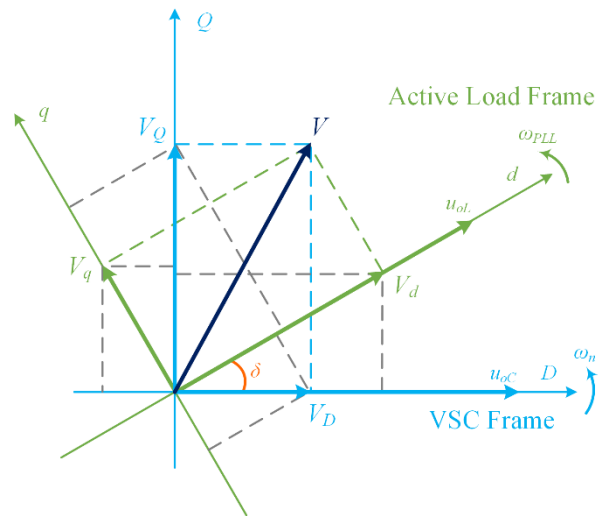


**Figure 4.3** : Coordinate transformation.

It should be noted that the models of the VSC and the AFE are established in different frames, e.g.,  $DQ$  frame for the VSC and  $dq$  frame for the AFE, as illustrated in Fig. 4.3. By

taking the VSC's  $DQ$  frame as reference, a coordinate transformation is required to convert the variables on the AFE's  $dq$  frame to the VSC's  $DQ$  frame, expressed as

$$\begin{bmatrix} x_D \\ x_Q \end{bmatrix} = \begin{bmatrix} \cos \delta & -\sin \delta \\ \sin \delta & \cos \delta \end{bmatrix} \begin{bmatrix} x_d \\ x_q \end{bmatrix} \quad (4-1)$$

where  $\delta$  is the angle difference between the AFE's  $dq$  frame and the VSC's  $DQ$  frame, and it is equal to  $(\theta_L - \theta_C)$ .

## 2). Model of the VSC.

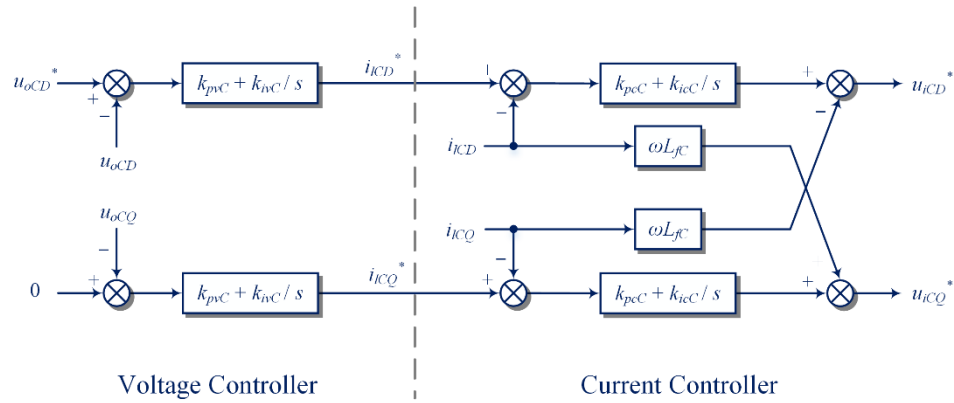


**Figure 4.4** : Cascaded control architecture of the VSC.

The VSC can be categorized into the controller part and the circuit part. For the controller part, the cascaded control architecture of the VSC is demonstrated in Fig. 4.4, including the outer voltage controller and the inner current controller. For the voltage controller, its dynamics are characterized by the following equations:

$$\begin{cases} s\varphi_{CD} = u_{oCD}^* - u_{oCD} \\ s\varphi_{CQ} = 0 - u_{oCQ} \end{cases} \quad (4-2)$$

$$\begin{cases} \dot{i}_{iCD}^* = k_{ivC}\varphi_{CD} + k_{pvC}(u_{oCD}^* - u_{oCD}) \\ \dot{i}_{iCQ}^* = k_{ivC}\varphi_{CQ} + k_{pvC}(0 - u_{oCQ}) \end{cases} \quad (4-3)$$

where  $\varphi_{CDQ}$  are the integral terms of the voltage controller; the superscript “ $*$ ” denotes reference values of the corresponding variables, and the same below;  $k_{ivC}$  and  $k_{pvC}$  are the integral and proportional gains of the voltage controller, respectively.

By taking the inductor current reference  $i_{iCDQ}^*$  from the voltage controller as inputs, the current controller dynamics of the VSC are described by the following equations:

$$\begin{cases} s\gamma_{CD} = i_{iCD}^* - i_{iCD} \\ s\gamma_{CQ} = i_{iCQ}^* - i_{iCQ} \end{cases} \quad (4-4)$$

$$\begin{cases} u_{iCD}^* = k_{icC}\gamma_{CD} + k_{pcC}(i_{iCD}^* - i_{iCD}) \\ u_{iCQ}^* = k_{icC}\gamma_{CQ} + k_{pcC}(i_{iCQ}^* - i_{iCQ}) \end{cases} \quad (4-5)$$

in which  $\gamma_{CDQ}$  are the integral terms of the current controller;  $k_{icC}$  and  $k_{pcC}$  are the integral and proportional gains of the current controller, respectively. The time delay associated with the PWM stage is neglected, and the terminal voltage  $u_{iCDQ}$  are assumed to track reference  $u_{iCDQ}^*$  immediately.

For the circuit part of the VSC, dynamics of the LC filter as well as the coupling inductance are all taken into consideration. By combining the controller part and the circuit part, and linearizing these equations around some steady-state operating point, the small-signal state-space model of the VSC can be written as the following form:

$$s[\Delta\mathbf{X}_{VSC}] = \mathbf{A}_{VSC}[\Delta\mathbf{X}_{VSC}] + \mathbf{B}_{VSC1}[\Delta\mathbf{u}_{bCDQ}] \quad (4-6)$$

$$[\Delta\mathbf{i}_{oCDQ}] = \mathbf{C}_{VSC}[\Delta\mathbf{X}_{VSC}] \quad (4-7)$$

where the prefix “ $\Delta$ ” signifies small variation from steady-state values, and the same below;  $\mathbf{A}_{VSC}$  is the characteristic matrix of the VSC model;  $\mathbf{B}_{VSC1}$  and  $\mathbf{C}_{VSC}$  are the input and output matrices of the VSC model, respectively. The bus voltage  $\Delta\mathbf{u}_{bCDQ}$  are taken as the inputs to the VSC model, and the output current  $\Delta\mathbf{i}_{oCDQ}$  are selected as the outputs of the VSC model.  $\Delta\mathbf{X}_{VSC}$  represents state variables of the VSC, expressed as

$$[\Delta\mathbf{X}_{VSC}] = [\Delta\varphi_{CD} \quad \Delta\varphi_{CQ} \quad \Delta\gamma_{CD} \quad \Delta\gamma_{CQ} \quad \Delta i_{iCD} \quad \Delta i_{iCQ} \quad \Delta u_{oCD} \quad \Delta u_{oCQ} \quad \Delta i_{oCD} \quad \Delta i_{oCQ}]^T \quad (4-8)$$

### 3). Model of the AFE.

Similar to the VSC model, the AFE model can also be divided into the controller part and the circuit part. The structure of the AFE controller is illustrated in Fig. 4.5, including a PLL, a DC voltage controller, and a current controller.

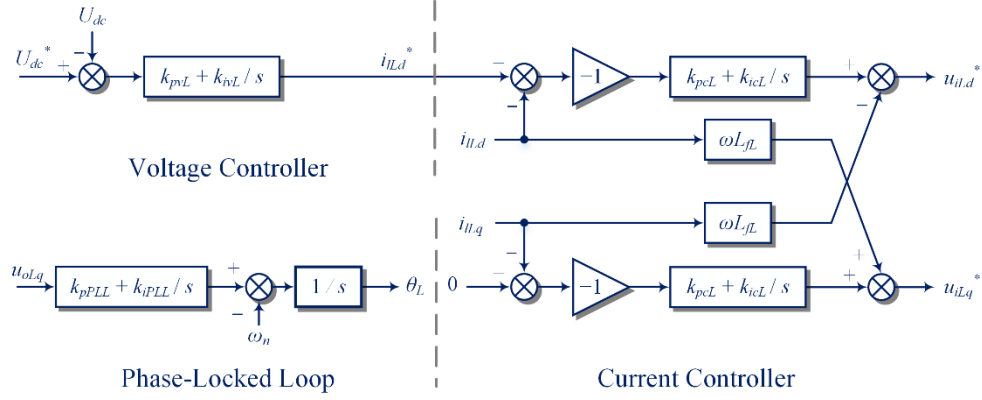


**Figure 4.5 :** Cascaded control structure of the AFE.

The PLL is employed in the AFE to keep synchronized with the VSC, with dynamics characterized by the following equations:

$$\begin{cases} s x_{pll} = u_{oLq} \\ s \theta_L = k_{ipll} x_{pll} + k_{ppll} u_{oLq} \end{cases} \quad (4-9)$$

where  $x_{pll}$  is the integral term of the PLL;  $k_{ipll}$  and  $k_{ppll}$  are the integral and proportional gains of the PLL, respectively.

The DC-link voltage of the AFE is regulated by the outer voltage controller, and its dynamics can be described with the following equations:

$$s \varphi_{dc} = U_{dc}^* - U_{dc} \quad (4-10)$$

$$\begin{cases} i_{LLd}^* = k_{ivL} \varphi_{dc} + k_{pvL} (U_{dc}^* - U_{dc}) \\ i_{LLq}^* = 0 \end{cases} \quad (4-11)$$

in which  $\varphi_{dc}$  is the integral term of the AFE voltage controller;  $k_{ivL}$  and  $k_{pvL}$  are the integral and proportional gains of the voltage controller, respectively.

For the current controller of the AFE, it takes the inductor current reference  $i_{LLdq}^*$  as inputs to generate the terminal voltage reference  $u_{iLLdq}^*$  for PWM. The dynamics of the current controller are expressed as

$$\begin{cases} s \gamma_{Ld} = i_{LLd}^* - i_{LLd} \\ s \gamma_{Lq} = i_{LLq}^* - i_{LLq} \end{cases} \quad (4-12)$$



$$\begin{cases} u_{iLd}^* = k_{icL}\gamma_{Ld} + k_{pcL}(i_{iLd}^* - i_{iLd}) \\ u_{iLq}^* = k_{icL}\gamma_{Lq} + k_{pcL}(i_{iLq}^* - i_{iLq}) \end{cases} \quad (4-13)$$

where  $\gamma_{Ldq}$  are the integral terms of the AFE current controller;  $k_{icL}$  and  $k_{pcL}$  are the integral and proportional gains of the current controller, respectively. The time delay associated with the PWM stage is neglected, and thus the terminal voltage  $u_{iLdq}$  are assumed to track their reference values immediately.

For the circuit part, similar to the VSC, on the AC side of the AFE, dynamics of the coupling inductor  $L_{cL}$  and filter inductor  $L_{fL}$  are also considered. Besides, on the DC side of the AFE, according to the power balance between the AC side and the DC side, the following equations are yielded, as

$$\begin{cases} U_{dc}I_{dc} = 3(u_{iLd}i_{iLd} + u_{iLq}i_{iLq}) \\ C_{dc} \frac{dU_{dc}}{dt} = I_{dc} - I_{CPL} \end{cases} \quad (4-14)$$

Since a CPL is supplied by the DC side of the AFE, the input current of the CPL, e.g.,  $I_{CPL}$ , is expressed as

$$I_{CPL} = \frac{P_{CPL}}{U_{dc}} \quad (4-15)$$

By taking the controller part and the circuit part into consideration, the small-signal state-space model of the AFE can be obtained by linearizing the above-mentioned equations around some steady-state operating point, expressed as

$$s[\Delta\mathbf{X}_{CPL}] = \mathbf{A}_{CPL}[\Delta\mathbf{X}_{CPL}] + \mathbf{B}_{CPL1}[\Delta u_{bLDQ}] \quad (4-16)$$

$$[\Delta i_{oLDQ}] = \mathbf{C}_{CPL}[\Delta\mathbf{X}_{CPL}] \quad (4-17)$$

in which  $\mathbf{A}_{CPL}$  is the characteristic matrix of the AFE,  $\mathbf{B}_{CPL1}$  and  $\mathbf{C}_{CPL}$  denote the input and output matrices of the AFE, respectively, with the input selected as the bus voltage  $\Delta u_{bLDQ}$ , and the outputs selected as  $\Delta i_{oLDQ}$ . It should be noted, while the control of the AFE is implemented on the AFE's  $dq$  frame, the inputs, and outputs of the AFE are expressed on the VSC's  $DQ$  frame, and thus the transformation given in (4-1) needs to be implemented

to realize the conversion between  $dq$  frame and  $DQ$  frame.  $\Delta\mathbf{X}_{CPL}$  signifies the state variables of the AFE model, expressed as

$$[\Delta\mathbf{X}_{CPL}] = [\Delta x_{pll} \quad \Delta\theta_{pll} \quad \Delta\varphi_{dc} \quad \Delta\gamma_{Ld} \quad \Delta\gamma_{Lq} \quad \Delta U_{dc} \quad \Delta i_{LLd} \quad \Delta i_{LLq} \quad \Delta i_{oLd} \quad \Delta i_{oLq}]^T \quad (4-18)$$

#### 4). State-space model of the interconnected system.

In this chapter, the modular modeling approach is adopted. The MEA electrical system is divided into different subsystems, and the state-space model of each subsystem is firstly established and then combined together to yield the complete state-space model of the whole MEA electrical system.

For the ease of modeling, the VSC and the AFE can be combined together to form a subsystem for the converter part in the MEA electrical system. By integrating (4-6) and (4-16), the state-space model of the converter subsystem is expressed as

$$s[\Delta\mathbf{X}_{CON}] = \mathbf{A}_{CON}[\Delta\mathbf{X}_{CON}] + \mathbf{B}_{1CON}[\Delta\mathbf{U}_{bDQ}] \quad (4-19)$$

$$[\Delta\mathbf{I}_{oDQ}] = \mathbf{C}_{CON}[\Delta\mathbf{X}_{CON}] \quad (4-20)$$

in which

$$[\Delta\mathbf{U}_{bDQ}] = \begin{bmatrix} \Delta u_{bCDQ} \\ \Delta u_{bLDQ} \end{bmatrix}, [\Delta\mathbf{X}_{CON}] = \begin{bmatrix} \Delta\mathbf{X}_{VSC} \\ \Delta\mathbf{X}_{CPL} \end{bmatrix}, [\Delta\mathbf{I}_{oDQ}] = \begin{bmatrix} \Delta i_{oCDQ} \\ \Delta i_{oLDQ} \end{bmatrix} \quad (4-21)$$

and the matrices  $\mathbf{A}_{CON}$ ,  $\mathbf{B}_{1CON}$  and  $\mathbf{C}_{CON}$  are respectively expressed as

$$\mathbf{A}_{CON} = \begin{bmatrix} \mathbf{A}_{VSC} & \mathbf{0} \\ \mathbf{0} & \mathbf{A}_{CPL} \end{bmatrix}, \mathbf{B}_{1CON} = \begin{bmatrix} \mathbf{B}_{VSC} & \mathbf{0} \\ \mathbf{0} & \mathbf{B}_{CPL} \end{bmatrix}, \mathbf{C}_{CON} = \begin{bmatrix} \mathbf{C}_{VSC} & \mathbf{0} \\ \mathbf{0} & \mathbf{C}_{CPL} \end{bmatrix} \quad (4-22)$$

To give a detailed microgrid model, dynamics of the connecting line are considered, and the dynamics of the connecting line are modelled as a separate subsystem, e.g., the network subsystem, on the reference  $DQ$  frame. The network subsystem can be written as

$$s[\Delta\mathbf{I}_{lineDQ}] = \mathbf{A}_{NET}[\Delta\mathbf{I}_{lineDQ}] + \mathbf{B}_{1NET}[\Delta\mathbf{u}_{bDQ}] \quad (4-23)$$

From (4-19) and (4-23), it is observed that the node voltages  $[\Delta\mathbf{U}_{bDQ}]$  are taken as the input

into both the converter and the network subsystems. A method is presented in [97] to define the node voltages with the virtual resistance  $r_N$ , as

$$[\Delta \mathbf{U}_{bDQ}] = \mathbf{R}_N \mathbf{M}_{CON} [\Delta \mathbf{I}_{oDQ}] + \mathbf{R}_N \mathbf{M}_{NET} [\Delta \mathbf{I}_{lineDQ}] \quad (4-24)$$

where  $\mathbf{R}_N$  is a diagonal matrix with elements being  $r_N$ ;  $\mathbf{M}_{CON}$  and  $\mathbf{M}_{NET}$  stand for the mapping matrices to assign the VSCs or lines to different node voltages, among which  $\mathbf{M}_{CON}$  is a unity matrix;  $\mathbf{M}_{NET}$  is a matrix filled with +1 or -1, depending on the direction of line current is entering or leaving the node.

With the node voltages defined in (4-24), the MEA electrical system demonstrated in Fig. 4.2 turns into an autonomous system, and thus a complete state-space model of the whole MEA electrical system can be derived by integrating the model of the converter subsystem, given by (4-19), and the network subsystem model, expressed in (4-23), as

$$s[\Delta \mathbf{X}_{MEA}] = \mathbf{A}_{MEA} [\Delta \mathbf{X}_{MEA}] \quad (4-25)$$

in which

$$[\Delta \mathbf{X}_{MEA}] = [\Delta \mathbf{X}_{CON}^T \quad \Delta \mathbf{I}_{lineDQ}^T]^T \quad (4-26)$$

and the characteristic matrix of the established MEA electrical system, e.g.,  $\mathbf{A}_{MEA}$ , is expressed as

$$\mathbf{A}_{MEA} = \left[ \begin{array}{c|c} \mathbf{A}_{CON} + \mathbf{B}_{1CON} \mathbf{R}_N \mathbf{M}_{CON} \mathbf{C}_{CON} & \mathbf{B}_{1CON} \mathbf{R}_N \mathbf{M}_{NET} \\ \hline \mathbf{B}_{1NET} \mathbf{R}_N \mathbf{M}_{CON} \mathbf{C}_{CON} & \mathbf{A}_{NET} + \mathbf{B}_{1NET} \mathbf{R}_N \mathbf{M}_{NET} \end{array} \right] \quad (4-27)$$

#### 4.2.2. CPL Induced Instability

##### 1). Stability of the MEA electrical system as impacted by the CPL.

With the state-space model established in (4-25), the stability of the MEA electrical system with the presence of the CPL can be examined by checking the eigenvalue distribution of the characteristic matrix  $\mathbf{A}_{MEA}$ , as expressed in (4-27). The circuit and control parameters of the MEA electrical system are specified in Table 4.1 and Table 4.2, respectively.

**Table 4.1** : Circuit parameters of the MEA electrical system.

Parameter	Value	Parameter	Value
$f_n$	400 Hz	$L_{cL}$	$6.0 \times 10^{-6}$ H
$L_{fC}$	$1.2 \times 10^{-3}$ H	$r_{cL}$	$550 \times 10^{-3}$ $\Omega$
$r_{fC}$	0.2 $\Omega$	$L_{fL}$	$500 \times 10^{-6}$ H
$C_{fC}$	$31.3 \times 10^{-6}$ F	$r_{fL}$	$100 \times 10^{-3}$ $\Omega$
$L_{cC}$	$3.0 \times 10^{-6}$ H	$C_{dc}$	$150 \times 10^{-6}$ F
$r_{cC}$	$25 \times 10^{-3}$ $\Omega$	$U_n$	57.5 V
$L_{line}$	$3.0 \times 10^{-6}$ H	$U_{dc}$	270 V
$r_{line}$	$25 \times 10^{-3}$ $\Omega$	$P_{CPL}$	400 W

**Table 4.2** : Control parameters of the MEA electrical system.

Parameter	Value	Parameter	Value
$k_{pvC}$	0.0592	$k_{ipL}$	35680
$k_{ivC}$	83.7758	$k_{pvL}$	0.1979
$k_{pcC}$	2.7646	$k_{ivL}$	14.6608
$k_{icC}$	9801.7560	$k_{pcL}$	3.2044
$k_{ppl}$	26.76	$k_{icL}$	691.1504

A 22<sup>nd</sup>-order linearized state-space model is established for the MEA electrical system, of which 6 modes are oscillation modes. The distribution of these oscillation modes on the complex plane is demonstrated in Fig. 4.6. Moreover, the damping ratio of each oscillation mode is calculated and given in Table 4.3. From Table 4.3, the oscillation modes with a pair of eigenvalues “ $\lambda_5 = -1.4505 \times 10^1 \pm j4.0437 \times 10^2$ ” is recognized as the critical mode, which is the least damped one with a damping ratio of only 3.58%, as signified by yellow circles in Fig. 4.6.

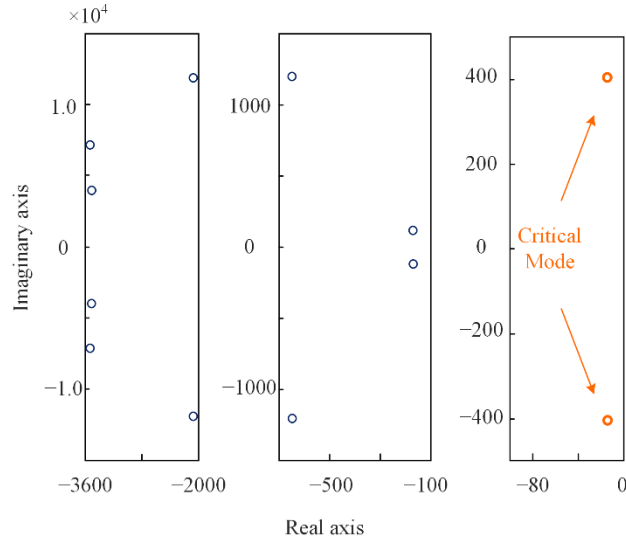


**Figure 4.6 :** Eigenvalue distribution of the MEA electrical system in presence of CPL.

**Table 4.3 :** Oscillation modes of the MEA electrical system.

NO.	Eigenvalues $\lambda_i$	Damping Ratio
1	$-2.0717 \times 10^3 \pm j1.1910 \times 10^4$	17.14%
2	$-3.5281 \times 10^3 \pm j7.1176 \times 10^3$	44.41%
3	$-3.5104 \times 10^3 \pm j3.9478 \times 10^3$	66.45%
4	$-6.5130 \times 10^2 \pm j1.1940 \times 10^3$	47.89%
<b>5</b>	<b><math>-1.4505 \times 10^1 \pm j4.0437 \times 10^2</math></b>	<b>3.58%</b>
6	$-1.7582 \times 10^2 \pm j1.1893 \times 10^2$	82.83%

## 2). Stability of the critical mode as impacted by the CPL.

To further verify the stability of the critical mode as impacted by CPL, the root locus of the critical mode with the growth of the CPL power level from 50 W to 450 W is demonstrated in Fig. 4.7. Besides, under the different situations with various CPL power levels, the damping ratio corresponding to the critical mode is also calculated, as illustrated in Fig. 4.8.

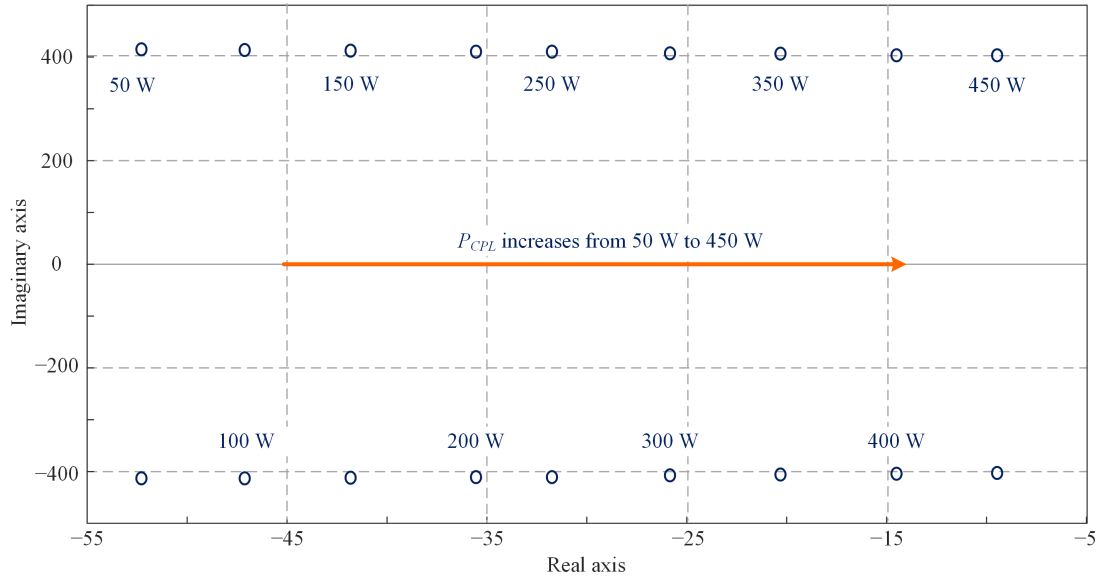


**Figure 4.7 :** Root locus of the critical mode with the change of CPL power level.

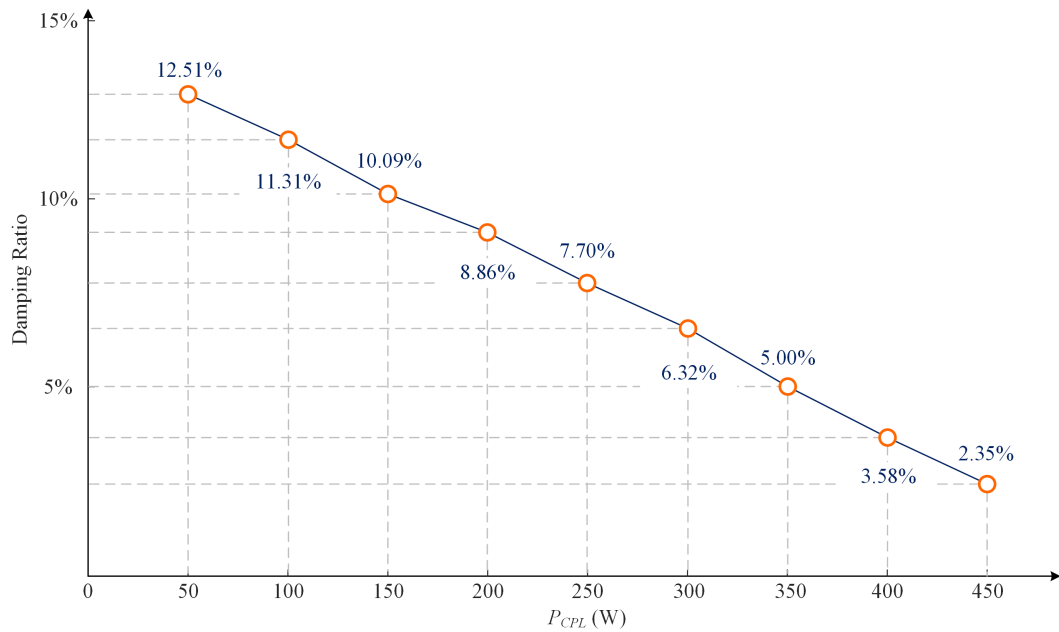


**Figure 4.8 :** Change of the critical mode damping ratio with the increase of CPL power level.

From Fig. 4.7, it is clearly obtained that with the increase of the CPL power level from 50 W to 450 W, the eigenvalues corresponding to the critical mode keep moving towards the imaginary axis, denoting a reduced stability with the CPL power leveling up. Therefore, it

is confirmed that the identified critical mode is sensitive to the CPL, and the CPL substantially deteriorates the stability of the critical mode, threatening the stable operating of the whole MEA electrical system. In addition, it is noticed that the higher the CPL power level is, the more adverse impacts are on the stability of the whole MEA electrical system. This conclusion is also confirmed from Fig. 4.8, in which the damping ratio of the critical mode is 12.51% with a 50 W CPL; with the increase of the CPL power level, the damping ratio of the critical mode keeps declining, and it finally declines to only 2.35% when the CPL power level grows to 450 W. Once a higher power level of the CPL is applied to the system, a negative damping ratio can be expected, and instability will occur consequently.

### 3). Participation factor analysis for the critical mode.

In order to identify the dominant state variables characterizing the dynamics of the critical mode, participation factor analysis is performed for the critical mode, with results exhibited in Fig. 4.9. It is concluded from Fig. 4.9 that the dynamics of the critical mode are principally dominated by the state variables associated with the VSC voltage controller, accounting for 39.8%, as well as the state variables regarding the AFE voltage controller, explaining 35.9% of the total participation in the critical mode dynamics.

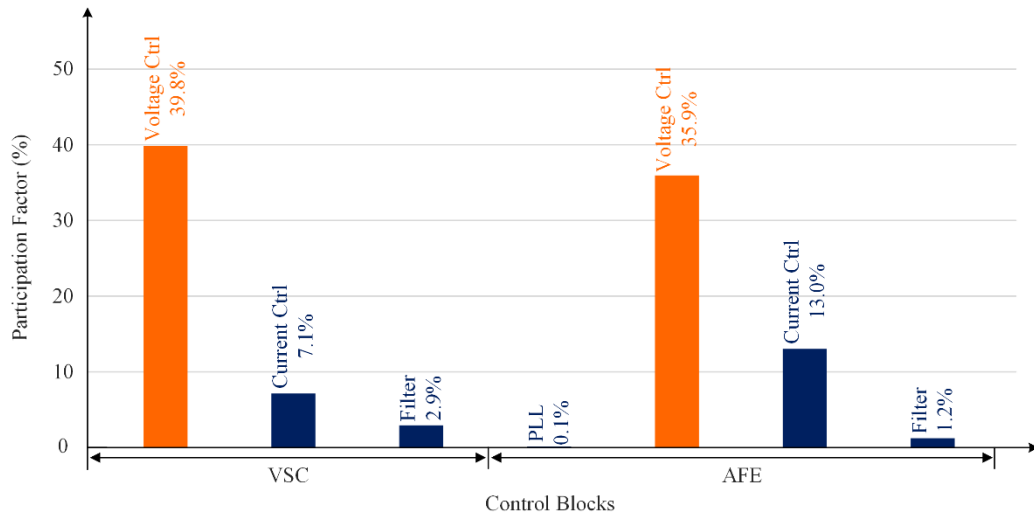


**Figure 4.9** : Participation factor analysis of the critical mode.

To further illustrate the impacts of the voltage controllers of the VSC as well as the AFE on the critical mode stability, the control parameters of the voltage controllers are modified for the VSC and the AFE, and the modification is realized by multiplying the voltage control PI parameters  $k_{ivC}$  and  $k_{pvC}$  for the VSC (or  $k_{ivL}$  and  $k_{pvL}$  for the AFE) with a gain  $K_C$  (or  $K_L$ ), explained as

$$k_{pvC} = K_C \cdot k_{pvC0}, k_{ivC} = K_C \cdot k_{ivC0} \quad (4-28)$$

$$k_{pvL} = K_L \cdot k_{pvL0}, k_{ivL} = K_L \cdot k_{ivL0} \quad (4-29)$$

in which the parameters with the subscript “0” signify initial values, which are taken from Table 4.2. It should be noted that, with the increase of the gains  $K_C$  and  $K_L$ , the bandwidths of the VSC and the AFE voltage controllers also increase, representing a higher response speed of the controller following control references.

Fig 4.10 demonstrates the change of the critical mode damping ratio with different  $K_C$  and  $K_L$ . It is observed that with the change of  $K_C$  and  $K_L$ , the damping ratio of the critical mode also varies significantly, indicating that the stability of the critical mode is impacted substantially by the interactions between the VSC and the AFE voltage controllers.

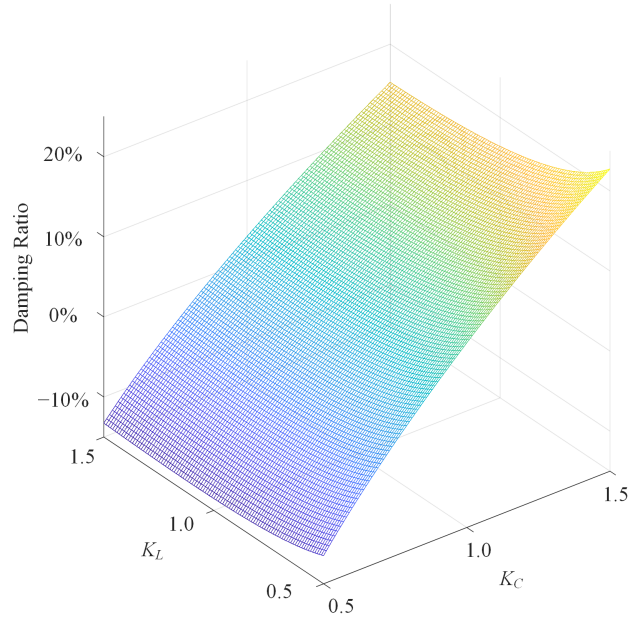


**Figure 4.10 :** Damping ratio of the critical mode as impacted by the voltage control parameters of the VSC and the AFE.



According to Fig. 4.10, the relationships between the damping ratio of the critical mode and the gains  $K_C$  as well as  $K_L$  are further illustrated in Fig. 4.11. From Fig. 4.11(a), with the increase of  $K_C$ , the damping ratio of the critical mode grows, showing that the stability of the system is improved by boosting the voltage control bandwidth of the VSC. Nonetheless, on the contrary of Fig. 4.11(a), as depicted in Fig. 4.11(b), the damping ratio of the critical mode declines continuously with the increase of  $K_L$ , indicating that the stability of the system is deteriorated with the increase of the voltage control bandwidth of the AFE. As a consequence, it can be concluded from Fig. 4.10 that the stability of the critical mode can be enhanced by either increasing the voltage control bandwidth of the source-side VSC or by reducing the load-side AFE voltage control bandwidth.

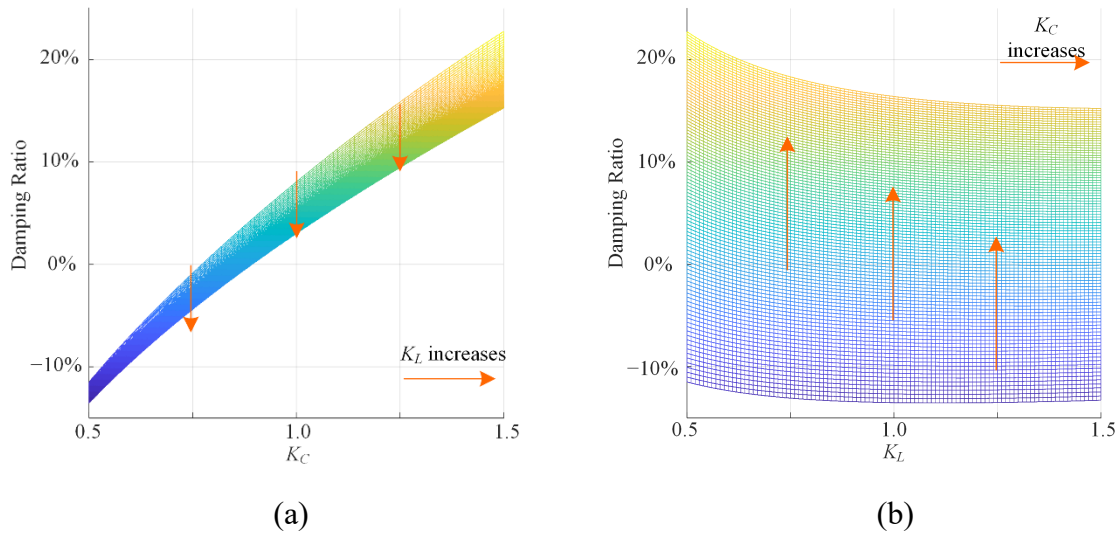


**Figure 4.11 :** The relationship between the damping ratio of the critical mode with the VSC control parameters and the AFE control parameters. (a) Damping ratio in relationship with  $K_C$ . (b) Damping ratio in relationship with  $K_L$ .

Therefore, it is concluded that CPLs do have substantial influence on the stability of MEA electrical system, and with the increase of the CPL power level, the eigenvalues of the critical mode move towards the imaginary axis, signifying a reduced stability for the MEA electrical system. Moreover, once the CPL power level grows beyond a certain level, instability will occur, threatening the safety and stability of the MEA electrical system.

---

When further analysis is conducted for the critical mode, it is found that the interactions between the voltage controllers of the VSC and the AFE dominate the dynamics of the critical mode, and the damping ratio of the critical mode can be enhanced by choosing different proportional and integral parameters for voltage controllers. Therefore, one possible method to alleviate the CPL-induced instability problem is the coordinated tuning of the voltage control parameters for the source-side VSC and the load-side AFE, so that the system stability with the presence of CPLs can be enhanced.

However, tuning control parameters does not provide a comprehensive solution to instability issues. Besides, since the voltage control parameters also closely relate with filter dynamics, and they are usually designed to suppress filter resonance peak. As a result, the proportional and integral parameters of voltage controllers cannot be adjusted arbitrarily, and the parameter setting of the voltage controllers, for the purpose of mitigating CPL-induced instability, may conflict with the objective of suppressing filter resonance. Therefore, additional control loops need to be developed to improve the system stability with the presence of CPLs.

### **4.3. Stability Enhancement Approaches for CPLs**

#### **4.3.1. Equivalence between Integral Control and Motion Equation**

As analyzed in the above sections, the critical mode, which is sensitive to the CPL power level, is characterized principally by the state variables associated with the voltage controllers of the VSC and the AFE. By looking into the structure of the PI control-based voltage controller, as depicted in Fig. 4.12, it can be observed that the integral part of the voltage controller shares a similar form with the well-known motion equation of synchronous generators, as shown in Fig. 4.13.

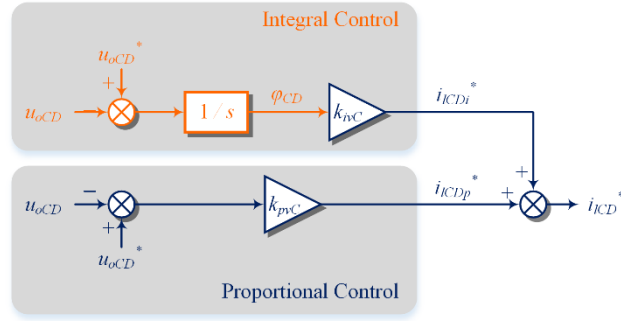


**Figure 4.12 :** Voltage control of the VSC.

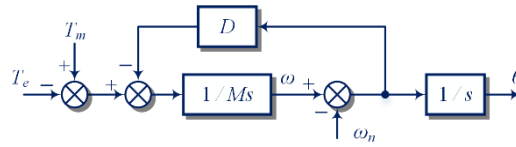


**Figure 4.13 :** Motion equation of synchronous generators.

The motion equation is of central importance in the stability analysis of conventional synchronous-generator-dominated power systems, and it describes the acceleration and deceleration of a synchronous generator rotor under unbalanced torques. In the motion equation, as illustrated in Fig. 4.13,  $T_e$  and  $T_m$  represent the electromagnetic torque and mechanical torque exerted on a rotor, respectively;  $\omega$  signifies the angular velocity of the rotor,  $\omega_n$  signifies the rated value of the angular velocity;  $\theta$  represents the angular position of the rotor in electrical radians with respect to a synchronous rotating reference, with its initial value set to 0;  $M$  denotes the moment of inertia, a quantity determined by the physical characteristic of the rotor;  $D$  is the damping factor. From Fig. 4.13, when the rotor angular velocity  $\omega$  deviates from its rated value  $\omega_n$ , a damping torque, which is in the opposite direction with the angular velocity deviation, will be synthesized by the damping factor  $D$ , and the rotor will be forced to go back to the rated angular velocity by the damping torque, thus helping maintain the stability of the rotor system.

For the integral part of the voltage controller, if the  $D$ -axis output voltage  $u_{oCD}$  is regarded as  $T_e$ , and the reference of the  $D$ -axis output voltage  $u_{oCD}^*$  is seen as  $T_m$ , then, the integral control of the voltage controller can be equivalently regarded as a synchronous generator with an equivalent moment of inertia equals to 1, and correspondingly the output of the

---

equivalent generator is  $\varphi_{CD}$ , which is the integral term generated by the integral part of the voltage controller. Besides, by comparing Fig. 4.12 and Fig. 4.13, one significant difference between the integral part of the voltage controller and the motion equation of synchronous generators is that no damping term exists in the integral part.

On the basis of the similarity between the integral part of the voltage controller and the motion equation of synchronous generators, the stability of the electrical system in the face of CPLs can be enhanced by generating an extra damping torque in the integral part of the voltage controller, so that the stabilizing effect of the damping factor  $D$  in rotor dynamics can be transplanted into the control architecture of power converters to improve the stability.

In the following sections, two control schemes are presented, e.g., a damper-based stability enhancement approach and a stabilizer-based stability improvement approach.

### **4.3.2. Approach 1: A Damper-Based Scheme to Improve the System Stability in the Face of CPL**

#### **1) Structure of the proposed damper.**

Based on the inherent similarity between the integral control and the motion equation, a damper-based stability enhancement scheme is developed in this section. The implementation of the proposed damper-based scheme is demonstrated in Fig. 4.14, in which an additional damper is imposed on the integral part of the voltage control, so that the stability of the system in the face of CPLs can be improved by mimicking the stabilizing effect of the damping factor in synchronous generators.

In order to avoid modification on the load characteristic of the CPL, the proposed damper is implemented on the source side, e.g., the voltage controller of the VSC. As shown in Fig. 4.14, the filter current reference  $i_{iCDi}^*$ , generated by the integral part of the VSC voltage

controller, is taken as the input to the proposed damper to produce a damping signal  $u_d$ , and the generated stabilizing signal  $u_d$  is in turn imposed on the integral part of the voltage controller of the VSC, so that the system stability with the presence of CPLs can be improved consequently.

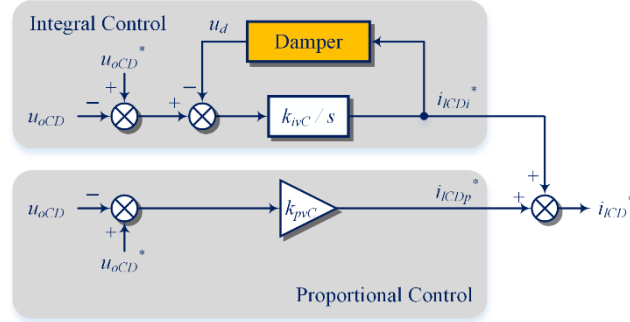


**Figure 4.14 :** A damper-based scheme to mitigate the CPL instability issue.

The structure of the proposed damper is shown in Fig. 4.15, in which a bandpass filter is cascaded with a washout filter. The washout filter is applied to avoid DC offset, so that the proposed damper is only activated during transients and has no impacts on steady states of the VSC. The transfer function of the washout filter model is described as

$$G_{wof}(s) = \frac{T_w s}{1 + T_w s} \quad (4-30)$$

where  $T_w$  is the time constant of the washout filter, and it is usually selected as 5 s in power system stability field.

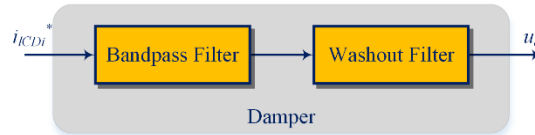


**Figure 4.15 :** Structure of the proposed damper.

The proposed damper also includes a bandpass filter to select out the components corresponding to the critical mode. As a result, only the dynamics of the critical mode is optimized without bringing any adverse impacts on other unconcerned modes. The transfer function of the bandpass filter model is expressed as

$$G_{bpf}(s) = \frac{\omega_o s}{s^2 + \omega_o s + \omega_o^2} \quad (4-31)$$

in which  $\omega_o$  is the central frequency of the bandpass filter.

Combining (4-30) and (4-31) gives the transfer function of the proposed damper, as

$$G_{Dmp}(s) = G_{wof}(s) \cdot G_{bpf}(s) \quad (4-32)$$

## 2) Parameter design for the proposed damper.

From (4-30) and (4-31), it is found that for the proposed damper, only one parameter needs to be set, e.g., the central frequency of the bandpass filter  $\omega_o$ , and it can be simply set to be equal to the oscillation frequency  $\omega_{CM}$  of the critical mode, as

$$\omega_o = \omega_{CM} \quad (4-33)$$

A flowchart is illustrated in Fig. 4.16 to summarize the procedures to design the proposed damper. From Fig. 4.16, it is observed that the developed damper features simple structure and easy parameter setting. Besides, since the proposed damper is only implemented on the source-side converter, it has no adverse impacts on the load characteristic.

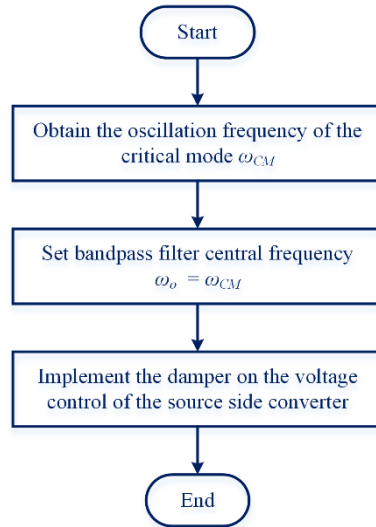


**Figure 4.16 :** Flowchart for designing the proposed damper.

### 4.3.3. Approach 2: A Stabilizer-Based Scheme to Enhance the System Stability in the Face of CPL

#### 1) Structure of the proposed stabilizer.

In order to enhance the stability of the system with the presence of CPLs, a stabilizer is presented in this section based on the similarity between the integral part of the voltage control and the motion equation of synchronous generators. Different from the presented damper in last section, which is implemented by directly adding a damping term in the integral part, the stabilizer presented in this section provides another approach to enhance the system stability with the presence of CPL, e.g., synthesizing an equivalent damping torque  $T_D$ , which is proportional to the integral term  $\varphi_{CD}$  of the voltage controller.

The scheme of the proposed stabilizer is illustrated in Fig. 4.17, and similar to the damper, the presented stabilizer is also installed on the source side converter, so that there is no modification on the control of the load side converter. From Fig. 4.17, the integral term  $\varphi_{CD}$  from the VSC voltage controller is taken as the input to the proposed stabilizer, and a stabilizing signal  $u_{stb}$  is generated by the stabilizer and imposed on the VSC voltage controller. Thus, the linearized form of the stabilizer can be written as

$$\Delta u_{stb} = G_{Stb}(s) \cdot \Delta \varphi_{CD} \quad (4-34)$$

where  $G_{Stb}(s)$  is the transfer function of the proposed stabilizer, which will be detailed in the following.

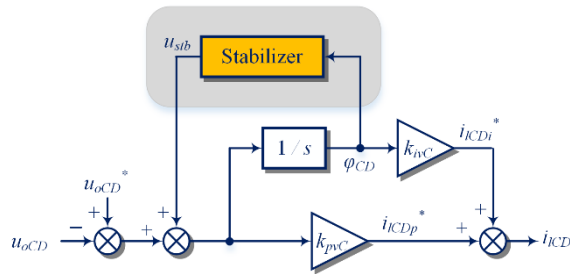


**Figure 4.17** : A stabilizer-based scheme to mitigate the CPL instability issue.

The structure of the proposed stabilizer is demonstrated in Fig. 4.18, including a filter block and a phase compensator. For the filter block, it is consisted of a washout filter, with its transfer function detailed in (4-30), a bandpass filter, with the transfer function given by (4-31), and a low-pass filter, the transfer function of which is expressed as

$$G_{lpf}(s) = \frac{\omega_{lp}}{s + \omega_{lp}} \quad (4-35)$$

in which  $\omega_{lp}$  is the cut-off frequency of the low-pass filter.

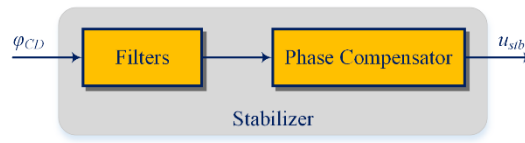


**Figure 4.18 :** Structure of the proposed stabilizer.

Besides, since the stabilizer signal  $u_{stb}$  is not imposed directly on the integral part of the voltage control, which is the manner of damper as shown in Fig. 4.17, phase lags may be incurred in the transfer loop from the output of the stabilizer  $u_{stb}$  to the synthesized torque  $T_D$ , denoted as  $G_{u \rightarrow T}(s)$ . In order to guarantee that the synthesized torque by the developed stabilizer is a pure damping torque, a phase compensator with the transfer function  $G_{PC}(s)$  is embedded in the proposed stabilizer, to compensate the phase lag regarding  $G_{u \rightarrow T}(s)$  as well as the phase lag associated with the filter block, as illustrated with the signal-flow graph given in Fig. 4.19.

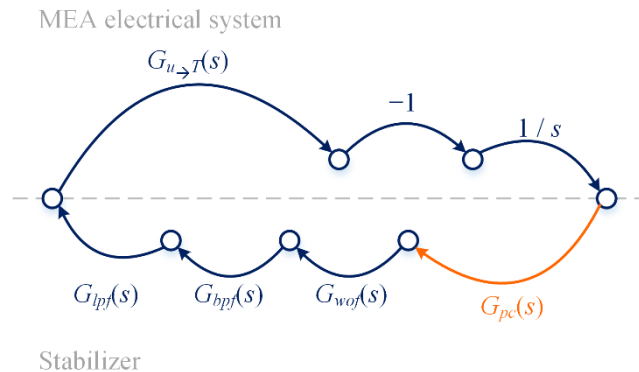


**Figure 4.19 :** Signal-flow graph of the system with the proposed stabilizer.



The phase compensator is realized by a set of cascaded lead-lag loops, expressed as

$$G_{PC}(s) = K_0 \cdot K_1 \frac{1+sT_2}{1+sT_1} \cdot K_2 \frac{1+sT_4}{1+sT_3} \cdot K_3 \frac{1+sT_6}{1+sT_5} \quad (4-36)$$

where  $K_0, K_1, K_2,$  and  $K_3$  are the gains of each lead-lag loop;  $T_1 \sim T_6$  are time constants of the lead-lag loops.

Combining (4-30), (4-31), (4-35), and (4-36) gives the transfer function of stabilizer, as

$$G_{Sib}(s) = G_{Filter}(s) \cdot G_{PC}(s) \quad (4-37)$$

in which  $G_{Filter}(s)$  signifies the transfer function of the filter block, written as

$$G_{Filter}(s) = G_{wof}(s) \cdot G_{bpf}(s) \cdot G_{lpf}(s) \quad (4-38)$$

## 2) Parameter design of the proposed stabilizer.

The key in determining the phase compensator parameters is the correct identification of the transfer function from the output of the stabilizer  $u_{stb}$  to the synthesized torque  $T_D$ , e.g.,  $G_{u \rightarrow T}(s)$ . With the transfer function  $G_{u \rightarrow T}(s)$  recognized, the phase lag of  $G_{u \rightarrow T}(s)$  at the frequency of the critical mode can be obtained, and thus the parameters of the phase compensator  $G_{PC}(s)$  can be designed accordingly to compensate the phase lag. As a result, a pure damping torque will be synthesized by the developed stabilizer to improve the stability of the critical mode.

Taking  $u_{stb}$ , the signal generated by the proposed stabilizer, as the input, the state-space model of the MEA electrical system shown in (4-25) turns into

$$s[\Delta \mathbf{X}_{MEA}] = \mathbf{A}_{MEA} [\Delta \mathbf{X}_{MEA}] + \mathbf{B}_{MEA} [\Delta u_{stb}] \quad (4-39)$$

in which  $\mathbf{B}_{MEA}$  denotes the input matrix corresponding to  $\Delta u_{stb}$  of the state-space model for the MEA electrical system.

By rearranging (4-39), it can be written as

$$s \begin{bmatrix} \Delta \varphi_{CD} \\ \Delta \mathbf{z} \end{bmatrix} = \begin{bmatrix} 0 & -\mathbf{A}_{12} \\ \mathbf{A}_{21} & \mathbf{A}_{22} \end{bmatrix} \begin{bmatrix} \Delta \varphi_{CD} \\ \Delta \mathbf{z} \end{bmatrix} + \begin{bmatrix} 1 \\ \mathbf{B}_2 \end{bmatrix} [\Delta u_{stb}] \quad (4-40)$$

where  $\Delta \mathbf{z}$  is the vector containing all the state variables in  $\Delta \mathbf{X}_{MEA}$ , except for  $\Delta \varphi_{CD}$ ; correspondingly, the characteristic matrix  $\mathbf{A}_{MEA}$  is also divided into different blocks corresponding to  $\Delta \varphi_{CD}$  and  $\Delta \mathbf{z}$ , as shown in (4-40).

Then, on the basis of (4-34) and (4-40), a closed-loop model of the MEA electrical system with the proposed stabilizer is illustrated in Fig. 4.20.

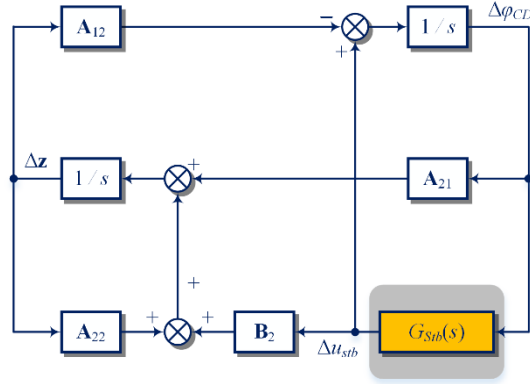


**Figure 4.20** : Closed loop model of the MEA electrical system with the stabilizer.

According to (4-40), it gives

$$s\Delta\varphi_{CD} = -\mathbf{A}_{12}\Delta\mathbf{z} + \Delta u_{stb} \quad (4-41)$$

$$s\Delta\mathbf{z} = \mathbf{A}_{21}\Delta\varphi_{CD} + \mathbf{A}_{22}\Delta\mathbf{z} + \mathbf{B}_2\Delta u_{stb} \quad (4-42)$$

Then, the following equation can be derived:

$$\begin{aligned} s\Delta\varphi_{CD} &= -\left[\mathbf{A}_{12}(s\mathbf{I} - \mathbf{A}_{22})^{-1}\mathbf{A}_{21}\right] \cdot \Delta\varphi_{CD} - \left[\mathbf{A}_{12}(s\mathbf{I} - \mathbf{A}_{22})^{-1}\mathbf{B}_2 - \mathbf{1}\right] \cdot \Delta u_{stb} \\ &= -\Delta T_{MEA} - \Delta T_D \end{aligned} \quad (4-43)$$

In (4-43), similar to the motion equation of synchronous generators, the dynamics of  $\Delta\varphi_{CD}$  can be regarded as the interaction result of two torques, e.g.,  $\Delta T_{MEA}$  and  $\Delta T_D$ .  $\Delta T_{MEA}$  is the equivalent torque contributed by the MEA electrical system itself, expressed as

$$\Delta T_{MEA} = \left[\mathbf{A}_{12}(s\mathbf{I} - \mathbf{A}_{22})^{-1}\mathbf{A}_{21}\right] \cdot \Delta\varphi_{CD} \quad (4-44)$$

and  $\Delta T_D$  is the equivalent torque contributed by the developed stabilizer, expressed as

$$\begin{aligned}\Delta T_D &= \left[ \mathbf{A}_{12} (s\mathbf{I} - \mathbf{A}_{22})^{-1} \mathbf{B}_2 - 1 \right] \cdot \Delta u_{stb} \\ &= G_{u \rightarrow T}(s) \cdot \Delta u_{stb}\end{aligned}\quad (4-45)$$

from which the expression of the transfer function from the output of the stabilizer  $u_{stb}$  to the synthesized torque  $T_D$ , e.g.,  $G_{u \rightarrow T}(s)$ , is derived as

$$G_{u \rightarrow T}(s) = \left[ \mathbf{A}_{12} (s\mathbf{I} - \mathbf{A}_{22})^{-1} \mathbf{B}_2 - 1 \right] \quad (4-46)$$

Substituting (4-34) and (4-37) into (4-45) gives

$$\Delta T_D = G_{u \rightarrow T}(s) \cdot G_{Filter}(s) \cdot G_{PC}(s) \cdot \Delta \varphi_{CD} \quad (4-47)$$

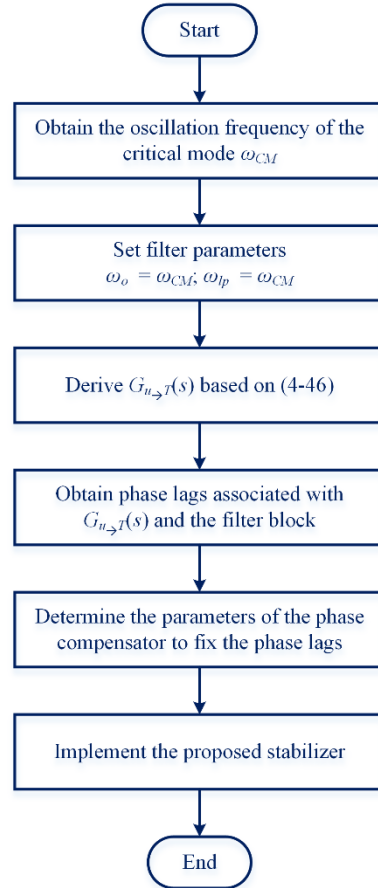


**Figure 4.21** : Flowchart for designing the proposed stabilizer.

---

In order to make the equivalent torque contributed by the stabilizer  $\Delta T_D$  be a damping torque, e.g., proportion to  $\Delta\phi_{CD}$ , the phase lags associated with the transfer functions  $G_{u \rightarrow T}(s)$  and  $G_{Filter}(s)$  need to be fully compensated by the phase compensator  $G_{PC}(s)$ . As a result, parameters of the phase compensator  $G_{PC}(s)$  can be selected accordingly. A flowchart is given in Fig. 4.21 to guide the structure design and parameter selection for the proposed stabilizer.

#### 4.4. Case Study

In the previous sections, the similarity between the integral part of voltage controllers and the motion equation of synchronous generators is illustrated. Based on the similarity, two stability enhancement schemes are developed, e.g., the damper-based method and the stabilizer-based approach. In this section, the system depicted in Fig. 4.2 is taken as an example to illustrate how the proposed damper and stabilizer are designed and implemented to improve the stability of the system in the face of CPL, and the effectiveness of the proposed damper and stabilizer is validated with modal analysis as well as time-domain simulations.

##### 4.4.1. Damper-Based Stability Improvement Scheme

###### 1). Illustration of the damper design.

According to the modal analysis results of the example system, as given in Table 4.3, the oscillation mode with a pair of eigenvalues “ $\lambda_5 = -1.4505 \times 10^1 \pm j4.0437 \times 10^2$ ” is recognized as the critical mode, with a damping ratio of only 3.58%. To enhance the stability of the critical mode, and following the damper design procedures given in Fig. 4.16, the time constant of the washout filter  $T_w$  is set to be 5 s, and the central frequency of the bandpass filter  $\omega_o$  is set to be identical to the oscillation frequency of the critical frequency, e.g., 404.37 rad/s.

## 2). Modal analysis.

With the damper installed on the voltage controller of the VSC, as demonstrated in Fig. 4.14, the distribution of eigenvalues of the MEA electrical system with the proposed damper is shown in Fig. 4.22. Besides, the damping ratio of each oscillation mode is also calculated and given in Table. 4.4.

On the basis of Fig. 4.22 and Table. 4.4, with the help of the designed damper, the eigenvalues corresponding to the critical mode are shifted leftward from “ $-1.4505 \times 10^1 \pm j4.0437 \times 10^2$ ” to “ $-6.6945 \times 10^1 \pm j3.7133 \times 10^2$ ”, and the damping ratio of the critical mode is also boosted from 3.58% to 17.74% accordingly, indicating a nearly 5 times improvement in term of damping ratios. In addition, comparing Fig. 4.6 and Fig. 4.22, only the eigenvalues associated with the critical mode are shifted to the left by the proposed damper, while other unconcerned oscillation modes remain unaffected. This fact verifies the function of the bandpass filter in the proposed damper, and it contributes to eliminating the undesired interactions between the designed damper with other unconcerned oscillation modes of the MEA electrical system. As a consequence, only the dynamics of the critical mode is improved by the proposed damper, preventing any potential adverse influence on other oscillation modes of the system.

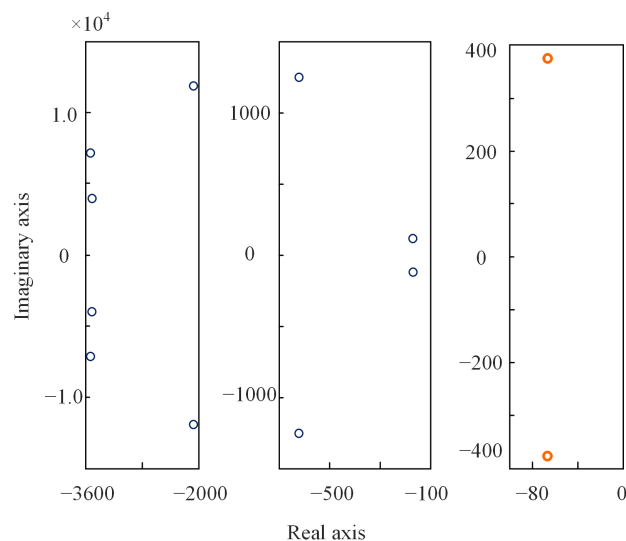


**Figure 4.22** : Eigenvalue distribution with the proposed damper.

---

**Table 4.4** : Oscillation modes of the MEA electrical system with the damper.

NO.	Eigenvalues $\lambda_i$	Damping Ratio
1	$-2.0717 \times 10^3 \pm j1.1910 \times 10^4$	17.14%
2	$-3.5285 \times 10^3 \pm j7.1177 \times 10^3$	44.42%
3	$-3.5104 \times 10^3 \pm j3.9478 \times 10^3$	66.45%
4	$-6.5130 \times 10^2 \pm j1.1940 \times 10^3$	47.89%
<b>5</b>	<b><math>-6.6945 \times 10^1 \pm j3.7133 \times 10^2</math></b>	<b>17.74%</b>
6	$-1.7582 \times 10^2 \pm j1.1893 \times 10^2$	82.83%

---

### 3). Time-domain simulation results.

The effectiveness of the proposed damper in improving the stability of the AC system with CPLs is illustrated through time-domain simulations. The system shown in Fig. 4.2 is established in Matlab/Simulink with detailed nonlinear models, and two different scenarios are considered in simulations to test the post-disturbance responses of the system with and without the proposed damper.

#### A. Scenario 1: response to DC-link voltage step change.

In this scenario, at  $t = 0.1$  s, the reference of the AFE DC-link voltage  $U_{dc}^*$  steps up from 270 V to 300 V. Post-disturbance curves of the system with and without the damper is shown in Fig. 4.23 and Fig. 4.24.

Since the proposed damper is imposed on the VSC voltage controller, one concern of the damper is the impacts on the steady state voltage regulation for the VSC. The waveforms of the three-phase VSC output voltage  $u_{oc}$ , with and without the proposed damper, are displayed in Fig. 4.23. From Fig. 4.23, in both cases with and without the damper, the output voltages of the VSC are regulated to the nominal value in steady states, proving that the proposed damper has no adverse impacts on the VSC output voltage regulation. In addition, during transients, compared with the case without the proposed damper,  $u_{oc}$  reaches its steady state in a faster way with less oscillation in the case with the damper

installed on the VSC, validating the effectiveness of the proposed damper in improving stability and dynamic responses of the system with CPLs.

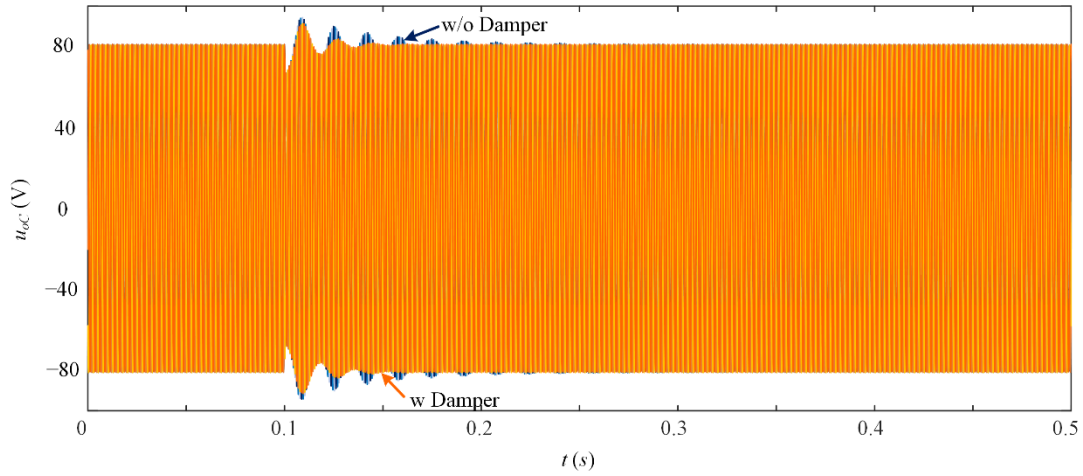
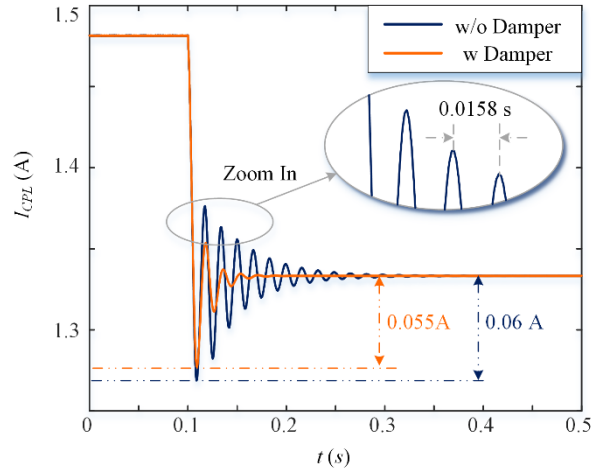


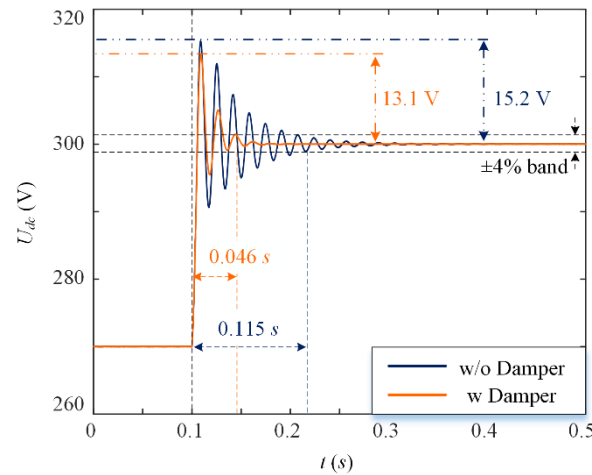
**Figure 4.23 :** Response to the DC-link voltage step up of the VSC three-phase output voltage  $u_{oC}$  with and without the damper.

For a clearer illustration, the AFE DC-side responses are taken as examples to show the effectiveness of the damper, as demonstrated in Fig. 4.24, including the input current of the CPL (e.g.,  $I_{CPL}$ ) and the DC-link voltage (e.g.,  $U_{dc}$ ). From Fig. 4.24(a), the oscillation cycle of the example system in time-domain simulations is 0.0158 s, which is very close to the oscillation cycle of the critical mode calculated from modal analysis in Table 4.3, e.g., “0.0156 s ( $2\pi / 404.37$  s)”. Thus, the accuracy and correctness of the derived state-space model is proved.

Besides, the post-disturbance dynamic responses are improved with the developed damper. As shown in Fig. 4.24(b), it is observed that in the case with the damper, the post-disturbance oscillations in  $U_{dc}$  are well suppressed: the settling time declines from 0.115 s to 0.046 s, indicating a 60% reduction, and the oscillation amplitude is also reduced from 15.2 V to 13.1 V, signifying a 13.8% reduction. Therefore, the effectiveness of the developed damper in enhancing the system stability with the presence of CPLs is validated, and a better post-disturbance dynamic response is witnessed in the time-domain simulations.



(a)



(b)

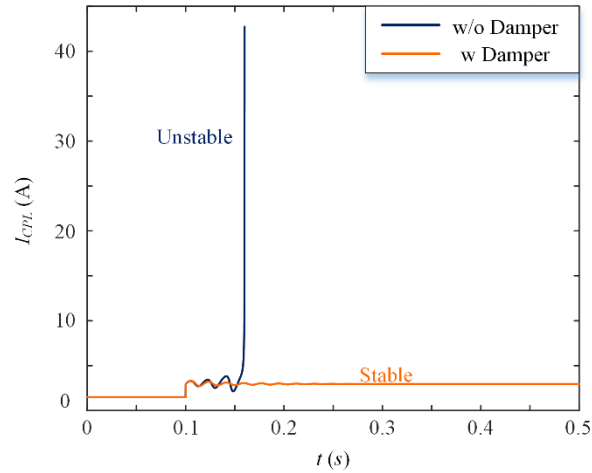
**Figure 4.24 :** Response to the DC-link voltage step up of the AFE DC side variables with and without the damper. (a) Input current of the CPL,  $I_{CPL}$ . (b) DC-link voltage of the AFE,  $U_{dc}$ .

B. Scenario 2: response to 100% CPL power step change.

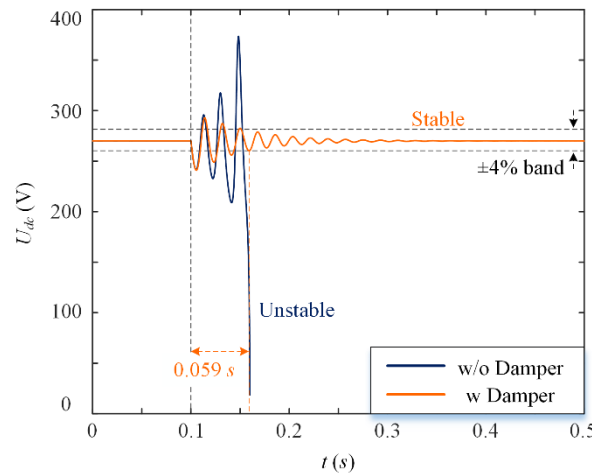
As demonstrated in Fig. 4.7 and Fig. 4.8, the power level of the CPL integrated in the power grid has substantial impacts on the system stability, and with the increase of CPL power level, the eigenvalues associated with the critical mode moves leftward, accompanied with a declined damping ratio. Thus, the adverse effect of the CPL on the system stability poses



an upper limit for the power level of the CPL that can be integrated into the power system, and once the upper limit of CPL power is exceeded, instability will occur as a consequence.



(a)



(b)

**Figure 4.25 :** Response to the CPL 100% power step up of the AFE DC side variables with and without the damper. (a) Input current of the CPL  $I_{CPL}$ . (b) DC-link voltage of the AFE  $U_{dc}$ .

In this scenario, a 100% step up in CPL power is set as the disturbance to test the effectiveness of the developed damper in expanding the stability margin of the system. At 0.1 s, the power level of CPL in the example system as shown in Fig. 4.2 is set to step up

---

from 400 W to 800 W. The post-disturbance responses of  $I_{CPL}$  as well as  $U_{dc}$  in the cases with and without the proposed damper are given in Fig. 4.25.

It is clearly demonstrated in Fig. 4.25, without the proposed damper, when the CPL power steps from 400 W to 800 W, the upper limit of CPL power is crossed, and the system loses stability: the DC-link voltage of the AFE  $U_{dc}$  cannot be regulated to its nominal value, and the input current to the CPL  $I_{CPL}$  also loses control, and it finally leads to the shunt down of the whole system. On the contrary, when the proposed damper is applied, the stability of the system is maintained in the face of the 100% CPL power step up, and the system goes back to its steady state with a settling time of only 0.059 s. Therefore, it is concluded that the proposed damper extends the stability margin of the system, and a higher level of CPL power can be integrated into the system with the help of the damper.

#### 4.4.2. Stabilizer-Based Stability Enhancement Scheme

In this section, case studies are given to illustrate the design and implementation of the proposed stabilizer-based stability enhancement scheme for AC systems integrated with CPL. The system shown in Fig. 4.2 with parameters specified in Table 4.1 and Table 4.2 is taken as the example for demonstration.

##### 1). Illustration of the stabilizer design

With the modal analysis results of the example system given in Table 4.3, the stabilizer will be designed to enhance the stability of the identified critical mode “ $\lambda_5 = -1.4505 \times 10^1 \pm j4.0437 \times 10^2$ ”. By substituting  $\lambda_5$  into (4-46), the frequency response of  $G_{u \rightarrow T}(s)$  corresponding to the critical mode is derived, as  $G_{u \rightarrow T}(\lambda_5) = 1.0302 \angle -163.90^\circ$ .

Thus, the phase angle of the proposed stabilizer at the critical mode, e.g.,  $G_{Stb}(\lambda_5)$ , should be designed as  $163.90^\circ$ , so that the phase lag in the transfer loop from the output of the stabilizer  $u_{stb}$  to the synthesized torque  $T_D$  can be fully fixed by the proposed stabilizer, and

consequently a pure damping torque will be synthesized to stabilize the critical mode. With the identified phase lag of  $G_{u \rightarrow T}(s)$  at the frequency of the critical mode and following the design procedures given in Fig. 4.21, the parameters of the proposed stabilizer are calculated and listed in Table 4.5.

**Table 4.5 :** Parameters of the proposed stabilizer.

Parameter	Description	Value
$\omega_o$	Bandpass filter central frequency	404.37 rad/s
$\omega_{lp}$	Low-pass filter cut-off frequency	404.37 rad/s
$T_w$	Washout filter time constant	5 s
$K_0$	Gain of the phase compensator	150
$K_1, K_2, K_3$	Gain of lead-lag loops	0.3409
$T_1, T_3, T_5$	Lead-lag loop time constants	0.0001 s
$T_2, T_4, T_6$	Lead-lag loop time constants	0.0069 s

## 2). Modal analysis

The eigenvalue distribution of the system with the proposed stabilizer is depicted in Fig. 4.26, and the damping ratios of oscillations modes with the proposed stabilizer are also calculated and listed in Table 4.6.

On the basis of Fig. 4.26 and Table 4.6, it is observed that with the help of the proposed stabilizer, the eigenvalues corresponding to the critical mode are shifted leftward from “ $-1.4505 \times 10^1 \pm j4.0437 \times 10^2$ ” to “ $-4.7572 \times 10^1 \pm j3.6225 \times 10^2$ ”, and the damping ratio of the critical mode is also enhanced from 3.58% to 13.02%, indicating a nearly 4 times improvement of stability in term of damping ratios.

Moreover, comparing Fig. 4.26 with Fig. 4.6, only the eigenvalues corresponding to the critical mode are shifted to the left by the designed stabilizer, while other unconcerned oscillation modes remain unchanged. This fact confirms the effectiveness of the bandpass filter in the stabilizer, and it contributes to eliminating any undesired interaction between

the designed stabilizer with other unconcerned modes, so that only the stability of the critical mode will be enhanced by the developed stabilizer, avoiding any possible adverse impacts on other unconcerned oscillation modes of the system.

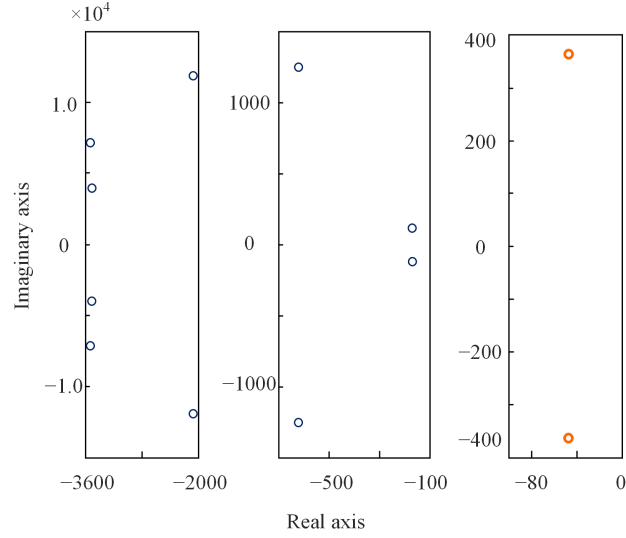


**Figure 4.26 :** Eigenvalue distribution with the proposed stabilizer.

**Table 4.6 :** Oscillation modes of the example system with the stabilizer.

NO.	Eigenvalues $\lambda_i$	Damping Ratio
1	$-2.0717 \times 10^3 \pm j1.1910 \times 10^4$	17.14%
2	$-3.5427 \times 10^3 \pm j7.1030 \times 10^3$	44.63%
3	$-3.5104 \times 10^3 \pm j3.9478 \times 10^3$	66.45%
4	$-6.5130 \times 10^2 \pm j1.1940 \times 10^3$	47.89%
<b>5</b>	<b><math>-4.7572 \times 10^1 \pm j3.6225 \times 10^2</math></b>	<b>13.02%</b>
6	$-1.7582 \times 10^2 \pm j1.1893 \times 10^2$	82.83%

### 3). Time-domain simulation results

The effectiveness of the proposed stabilizer in enhancing an AC system stability integrated with CPLs is validated through time-domain simulations. The example system shown in

Fig. 4.2 is established in Matlab/Simulink with detailed nonlinear models, and the parameters of the established system are taken from Table 4.1 and Table 4.2.

#### A. Scenario 1: response to DC-link voltage step change

In this scenario, at  $t = 0.1$  s, the DC-link voltage reference of the AFE  $U_{dc}^*$  steps from 270 V to 300 V. Post-disturbance waveforms of the system with and without the proposed stabilizer are shown in Fig. 4.27 and Fig. 4.28.

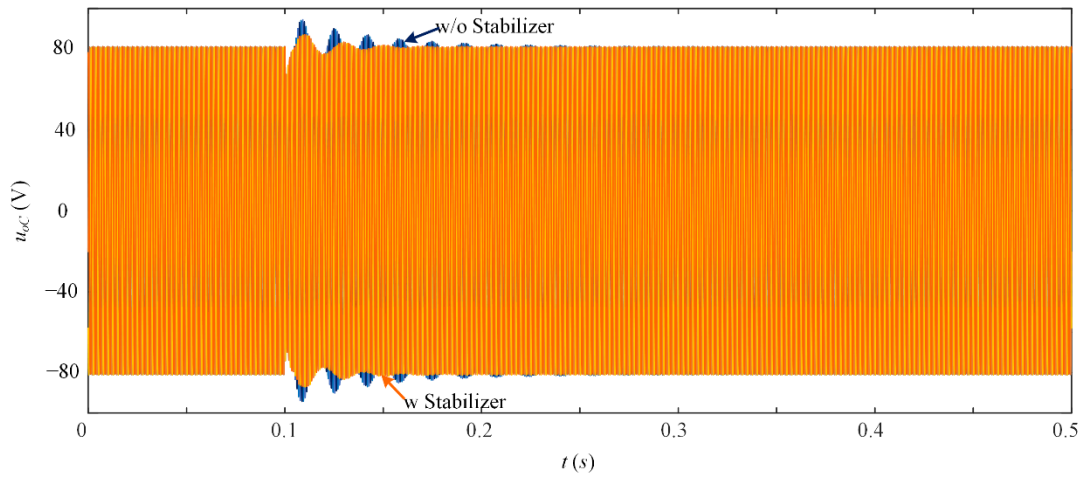
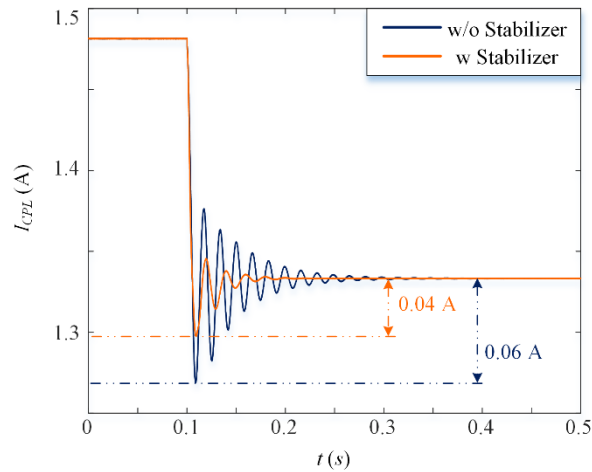


**Figure 4.27 :** Response to the DC-link voltage step up of the VSC three-phase output voltage  $u_{oC}$  with and without the stabilizer.

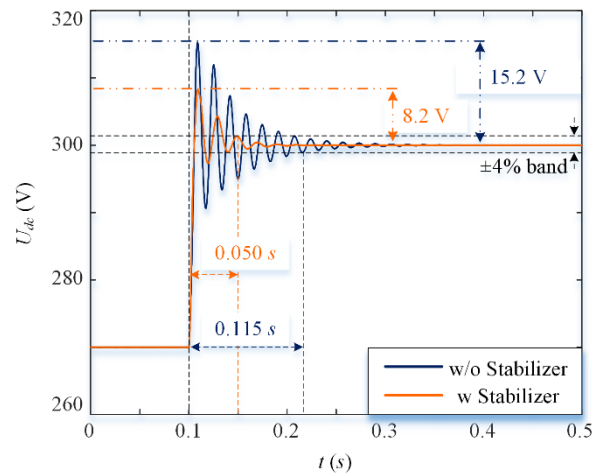
From Fig. 4.27, in both cases with and without the proposed stabilizer, the VSC outputs sinusoidal waveforms steadily, showing that the proposed stabilizer has no adverse influence on the VSC output voltage regulation. Moreover, during transients, compared with the case without the proposed stabilizer, the output voltage of the VSC  $u_{oC}$  reaches its steady state more quickly with the help of the stabilizer, validating the effectiveness of the proposed stabilizer in improving the dynamic response of the AC system with CPL integrated.

The DC-side post-disturbance responses of the AFE are shown in Fig. 4.28, including the input current of the CPL ( $I_{CPL}$ ) and the DC-link voltage ( $U_{dc}$ ). From Fig. 4.28(b), the

oscillations in  $U_{dc}$  are well suppressed: the settling time of  $U_{dc}$  declines from 0.115 s to 0.050 s, indicating a 56.5% reduction; the oscillation amplitude of  $U_{dc}$  is also reduced from 15.2 V to 8.2 V, signifying a 46.0% reduction. The improvement in post-disturbance dynamic responses can also be observed from  $I_{CPL}$ , as shown in Fig. 4.28(a). The overshoot of  $I_{CPL}$  falls from 0.06 A to 0.04 A with the help of the proposed stabilizer. Therefore, the effectiveness of the developed stabilizer in enhancing the stability of AC systems with CPLs integrated is validated.



(a)

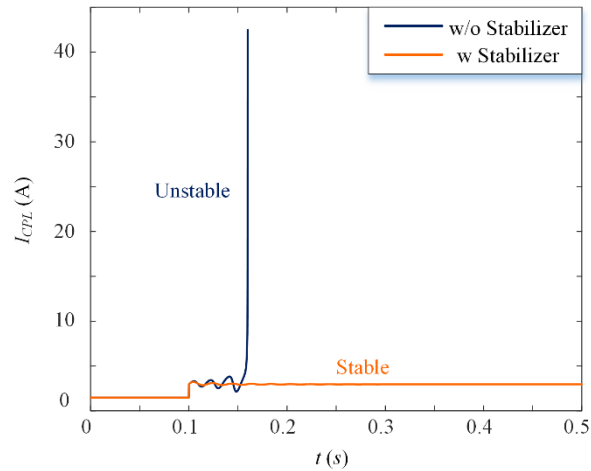


(b)

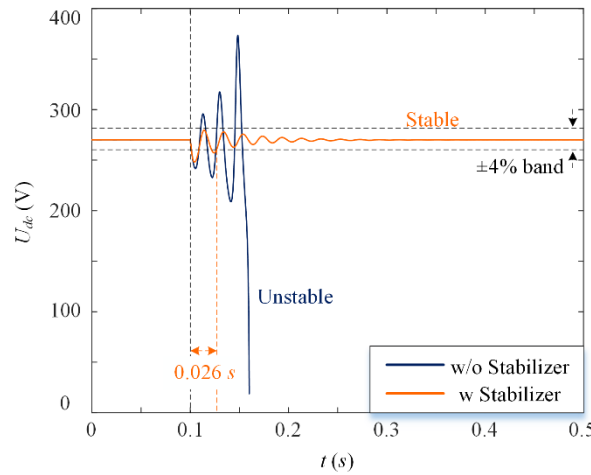
**Figure 4.28 :** Response to the DC-link voltage step up of the AFE DC side variables with and without the stabilizer. (a) Input current of the CPL  $I_{CPL}$ . (b) DC-link voltage of the AFE  $U_{dc}$ .

## B. Scenario 2: response to 100% CPL power step change

In this scenario, a 100% step up in CPL power is set as the disturbance. At  $t = 0.1$  s, the power level of CPL in the example system is set to step up from 400 W to 800 W. The post-disturbance responses of  $I_{CPL}$  as well as  $U_{dc}$  in the cases with and without the proposed damper are given in Fig. 4.29.



(a)



(b)

**Figure 4.29** : Response to the CPL 100% power step up of the AFE DC side variables with and without the stabilizer. (a) Input current of the CPL  $I_{CPL}$ . (b) DC-link voltage of the AFE  $U_{dc}$ .

---

It is clearly demonstrated in Fig. 4.29, without the proposed stabilizer, when the CPL power steps to 800 W, the upper limit of CPL power is crossed, and the system loses stability: the DC-link voltage of the AFE  $U_{dc}$  cannot be maintained to its nominal value, and the input current to the CPL  $I_{CPL}$  loses control, leading to the shunt down of the whole system.

On the contrary, with the help of the proposed stabilizer, the stability of the system is maintained in the face of the 100% CPL power step up, and the system quickly goes back to its steady state with a settling time of only 0.026 s. Therefore, it is concluded that the stability boundary of the system is enlarged with the developed stabilizer. As a consequence, a higher level of CPL can be integrated into the AC system with the stabilizing effect contributed by the designed stabilizer.

#### 4.5. Summary

In this chapter, the CPL-induced instability in AC systems is highlighted, and two different stability enhancement approaches are developed, e.g., the damper-based approach and the stabilizer-based approach. Both the damper and the stabilizer are designed based on the similarity between the integral part of the voltage controller and the motion equation of synchronous generators. With the help of the damper and the stabilizer, additional damping torques can be formed to boost the system stability in the face of CPLs.

Both the damper-based approach and the stabilizer-based approach demonstrate exemplary performance in enhancing the stability of AC systems with CPLs integrated. The system could reach its steady state much more quickly with the help of either the damper or stabilizer. Besides, the stability margin of AC systems is also enlarged with the developed damper and the stabilizer, and a higher level of CPL power can be integrated into AC systems without leading to instability problems.

The damper-based scheme features a simple structure, and only the center frequency of the bandpass filter needs to be tuned. Since the oscillation frequency of the critical mode can



---

be estimated from the post-disturbance waveforms, the central frequency just needs to be identical to the critical mode's angular frequency. Therefore, the damper-based approach can be applied to systems without the knowledge of detailed grid configuration and control parameters.

On the contrary, although demonstrating better performance in enhancing system stability and suppressing overshoot, the design of the stabilizer is more complicated compared with the proposed damper, and it requires the identification of the phase lags of transfer loops. Therefore, the stabilizer-based approach is preferred when the knowledge of the system parameters is known.



---

## **Chapter 5**

### **Conclusions and Future Work**

*This chapter concludes the whole thesis by summarizing its contents and highlighting major contributions. In addition, several future research perspectives are also discussed in this chapter for future studies, including the interaction between synchronous generators and power converters, and the cyber physical security problems.*

---

## 5.1. Conclusions

As the share of renewable energies keeps increasing in power grids, power electronic converters are widely deployed, serving as the interface between power grids and renewable generators. As a result, the traditional synchronous-generator-dominated power systems are evolving towards the power-electronic-dominated paradigms. In light of this background, several critical stability issues are studied in this thesis, including the frequency stability associated with the lack of inertia, the power interaction stability of islanded microgrids, and the stability issues regarding constant power loads. The stability issues covered in this thesis are dominated by different control stages of power converters, with their typical response times varying from seconds to dozens of milliseconds.

Chapter 2 focuses on the frequency stability of power-electronic-dominated systems. Firstly, it is illustrated how the lack of inertia translates into high RoCoF levels and large frequency deviations. Then, a grid-connected converter (GCC) based virtual inertia control scheme is introduced by utilizing the energy stored in DC-link capacitors to provide inertial supports during frequency events. However, due to the coupled relationship between grid frequency and DC-link voltage, the DC-link voltage cannot be restored even after providing inertial support, thus deteriorating DC-link capacitors' lifetime and losing the capability to offer multiple inertial support during cascading frequency events. A high-pass filter is designed in this chapter to settle this issue, which extracts out only high-frequency components from the grid frequency for inertial emulation during frequency events. As a result, the DC-link voltages of grid-connected converters can be restored autonomously after releasing their inertial power during each frequency event and thus avoid the abnormal working conditions of power converters.

Chapter 3 studies the stability issue in droop-controlled islanded microgrids. For islanded microgrids employing droop control to achieve power-sharing among multiple power generating units, a relatively large droop gain benefits the accurate power-sharing at the expense of sacrificed power interaction dynamic stability. Moreover, it is revealed that such stability issue is associated with the power control stages of power converters, and

---

simply tuning control parameters could not deal with this stability problem. Therefore, a converter-based power system stabilizer (CBPSS) is proposed in Chapter 3 to generate a damping torque to improve the stability of the islanded microgrid. Besides, an eigenvalue-mobility-based approach is also presented to guide selecting the optimal installation location for the proposed CBPSS in the islanded microgrid. The effectiveness of the designed CBPSS is verified with hardware experiments.

The instability caused by constant power loads (CPLs) for power-electronic-dominated power systems is highlighted in Chapter 4. The tightly regulated power converters behave as CPLs, featuring negative incremental impedance and introducing adverse impacts on the stability of power-electronic-dominated power systems. Moreover, with the increase of the power level of CPLs, such adverse effects also grow, and finally, it may trigger instability, threatening the security and reliability of the whole system. Then, participation factor analysis demonstrates that power converters' voltage controllers principally dominate such instability, with a typical response time of dozens of milliseconds. In light of such an instability problem, two control schemes, e.g., a damper-based scheme and a stabilizer-based scheme, are proposed to handle the instability issue associated with CPLs. The effectiveness of the proposed methods is verified with case studies.

## **5.2. Future Work**

Based on the studies mentioned above, some potential research perspectives are further proposed in this section, including the interaction studies between synchronous generators and power converters and the risk of cyber-attack in communication-based smart power grids, detailed as the following:

### **1) Interaction studies between synchronous generators and power converters.**

Modern power systems are increasingly integrated with renewable energies, heavily relying on power converters to interface with power grids, making power grids transferring

---

from synchronous-generator-dominated systems towards converter-dominated systems. During such transition, it can be expected that power converters will cohabit with conventional synchronous generators in power grids for a long time. However, traditional studies mainly focus on the stability of power converters themselves, with synchronous generators denoted as infinite buses to simplify the design and stability analysis for power converters. The infinite bus assumption holds when power converters' capacity is much smaller than synchronous generators in conventional centralized bulky power systems. However, with technological advances, the capacity of power converters proliferates, and it becomes comparable with that of synchronous generators, especially in scenarios such as microgrids. Consequently, the infinite bus assumption no more holds, and the dynamics of synchronous generators should be taken into consideration when analyzing the stability topics regarding power converters.

In this regard, the stability analysis of power converters considering dynamics of synchronous generators will be explored in future works, including the modeling of synchronous generators, interaction analysis between power converters and synchronous generators, and the corresponding stability enhancement schemes.

## **2) Cyber-physical system security.**

This thesis principally focuses on the control architectures in the primary control layer of power systems. However, as introduced in Chapter 1, despite the primary control, secondary control and tertiary control are also deployed in power grids to restore frequency and voltage deviations and set economic operating schemes.

Unlike primary control, communication channels are commonly required to exchange information in secondary and tertiary control. As a result, power grids transform towards cyber-physical systems (CPSs), consisting of electrical-coupled physical systems and communication-coupled cyber systems [152].

---

However, due to the open nature of communication channels, CPSs are also exposed to the risk of cyber-attacks. Thus, security issues are highlighted as a vital problem for CPSs. These cyber-attacks range from simple thefts and consumer load damage to high impacts that lead to shutdowns, cascading failures, and large blackouts. In addition, considering the fast response dynamics of power-electronic-dominated power systems, the time windows left to detect and defend cyber-attacks are very limited. As a result, the attacks in cyber layers could dramatically threaten the security of the whole power systems, leading to significant economic loss, with a real-world example of the Ukraine power grid in 2015 [153]. Typical cyber-attacks are characterized by the *DDD* model [154], including disclosure attacks, leading to unauthorized information release, deception attacks aiming to corrupt real data, and disruption attacks, resulting in the denial of service.

In light of this background, protecting power grids from cyber-attacks and guaranteeing operation security form another potential research perspective. It includes cyber-attack prevention, detection, and isolation from the point of power grids. In addition, the development of control schemes to enhance the resilience of power systems in the face of cyber-attacks also needs to be highlighted from the view of individual power converters.





---

## Author's Publications

### Journal Paper:

[1] **K. Guo**, Y. Qi, J. Yu, D. Frey, and Y. Tang. "A Converter Based Power System Stabilizer for Stability Enhancement of Droop Controlled Islanded Microgrids." *IEEE Transactions on Smart Grid* (2021). (DOI: 10.1109/TSG.2021.3096638)

### Conference Papers:

[2] **K. Guo**, Y. Tang, and J. Fang. "Exploration of the relationship between inertia enhancement and DC-link capacitance for grid-connected converters." In 2018 IEEE 4th Southern Power Electronics Conference (SPEC), pp. 1-7. IEEE, 2018.

[3] **K. Guo**, J. Fang, and Y. Tang. "Autonomous DC-link voltage restoration for grid-connected power converters providing virtual inertia." In 2018 IEEE Energy Conversion Congress and Exposition (ECCE), pp. 6387-6391. IEEE, 2018.



---

## Reference

- [1] IEA, "Net Zero by 2050: A Roadmap for the Global Energy Sector," International Energy Agency 2021.
- [2] R. A. Vaidya, D. J. Molden, A. B. Shrestha, N. Wagle, and C. Tortajada, "The role of hydropower in South Asia's energy future," *International Journal of Water Resources Development*, vol. 37, no. 3, pp. 367-391, 2021.
- [3] B. Truffer, C. Bratrich, J. Markard, A. Peter, A. Wüest, and B. Wehrli, "Green Hydropower: The contribution of aquatic science research to the promotion of sustainable electricity," *Aquatic Sciences*, vol. 65, no. 2, pp. 99-110, 2003.
- [4] REN21, "Renewables 2021 Global Status Report," REN21 Secretariat, Paris 2021.
- [5] A. Hoke, V. Gevorgian, S. Shah, P. Koralewicz, R. W. Kenyon, and B. Kroposki, "Island Power Systems With High Levels of Inverter-Based Resources: Stability and Reliability Challenges," *IEEE Electrification Magazine*, vol. 9, no. 1, pp. 74-91, 2021.
- [6] A. Khan, M. Hosseinzadehtaher, M. B. Shadmand, S. Bayhan, and H. Abu-Rub, "On the Stability of the Power Electronics-Dominated Grid: A New Energy Paradigm," *IEEE Industrial Electronics Magazine*, vol. 14, no. 4, pp. 65-78, 2020.
- [7] P. Denholm et al., "Bright Future: Solar Power as a Major Contributor to the U.S. Grid," *IEEE Power and Energy Magazine*, vol. 11, no. 2, pp. 22-32, 2013.
- [8] G. Spagnuolo et al., "Renewable Energy Operation and Conversion Schemes: A Summary of Discussions During the Seminar on Renewable Energy Systems," *IEEE Industrial Electronics Magazine*, vol. 4, no. 1, pp. 38-51, 2010.
- [9] B. Kroposki et al., "Achieving a 100% Renewable Grid: Operating Electric Power Systems with Extremely High Levels of Variable Renewable Energy," *IEEE Power and Energy Magazine*, vol. 15, no. 2, pp. 61-73, 2017.
- [10] A. Joseph and T. R. Chelliah, "A Review of Power Electronic Converters for Variable Speed Pumped Storage Plants: Configurations, Operational Challenges, and Future Scopes," *IEEE Journal of Emerging and Selected Topics in Power Electronics*, vol. 6, no. 1, pp. 103-119, 2018.
- [11] J. M. Guerrero, P. C. Loh, T.-L. Lee, and M. Chandorkar, "Advanced Control Architectures for Intelligent Microgrids—Part II: Power Quality, Energy Storage, and

- 
- AC/DC Microgrids," IEEE Transactions on Industrial Electronics, vol. 60, no. 4, pp. 1263-1270, 2013.
- [12] A. Farraj, E. Hammad, and D. Kundur, "On the Use of Energy Storage Systems and Linear Feedback Optimal Control for Transient Stability," IEEE Transactions on Industrial Informatics, vol. 13, no. 4, pp. 1575-1585, 2017.
- [13] M. Federico and D. o. Florian, "Foundations and Challenges of Low-Inertia Systems,"
- [14] D. Bukari, F. Kemausuor, D. A. Quansah, and M. S. Adaramola, "Towards accelerating the deployment of decentralised renewable energy mini-grids in Ghana: Review and analysis of barriers," Renewable and Sustainable Energy Reviews, vol. 135, p. 110408, 2021.
- [15] S. J. Plathottam, C. M. Ahmed, A. Nejadpak, and H. Salehfar, "Evaluating the Transient Stability Impact of Inertia Less Renewable Generation," 2016.
- [16] E. rum et al., "Future System Inertia," ENTSO-E Nordic Analysis Group 2015.
- [17] W. Du, X. Chen, and H. F. Wang, "Impact of Dynamic Interactions Introduced by the DFIGs on Power System Electromechanical Oscillation Modes," IEEE Transactions on Power Systems, vol. 32, no. 6, pp. 4954-4967, 2017.
- [18] W. He, X. Yuan, and J. Hu, "Inertia Provision and Estimation of PLL-Based DFIG Wind Turbines," IEEE Transactions on Power Systems, vol. 32, no. 1, pp. 510-521, 2017.
- [19] E. M. Authority, "Singapore Energy Statistics."
- [20] R. W. Erickson and D. Maksimovic, Fundamentals of Power Electronics. Springer Science & Business Media, 2007.
- [21] B. Singh, K. Al-Haddad, and A. Chandra, "A review of active filters for power quality improvement," IEEE transactions on industrial electronics, vol. 46, no. 5, pp. 960-971, 1999.
- [22] E. Muljadi and H. E. McKenna, "Power quality issues in a hybrid power system," IEEE Transactions on industry applications, vol. 38, no. 3, pp. 803-809, 2002.
- [23] D. Granados-Lieberman, R. Romero-Troncoso, R. Osornio-Rios, A. Garcia-Perez, and E. Cabal-Yepez, "Techniques and methodologies for power quality analysis and

- 
- disturbances classification in power systems: a review," *IET Generation, Transmission & Distribution*, vol. 5, no. 4, pp. 519-529, 2011.
- [24] Y. Tang, P. C. Loh, P. Wang, F. H. Choo, F. Gao, and F. Blaabjerg, "Generalized design of high performance shunt active power filter with output LCL filter," *IEEE Transactions on Industrial Electronics*, vol. 59, no. 3, pp. 1443-1452, 2011.
- [25] Y. Tang, P. C. Loh, P. Wang, F. H. Choo, and F. Gao, "Exploring inherent damping characteristic of LCL-filters for three-phase grid-connected voltage source inverters," *IEEE Transactions on Power Electronics*, vol. 27, no. 3, pp. 1433-1443, 2011.
- [26] F. Blaabjerg, *Control of Power Electronic Converters and Systems*. Academic Press, 2018.
- [27] Z. Chen, J. M. Guerrero, and F. Blaabjerg, "A Review of the State of the Art of Power Electronics for Wind Turbines," *IEEE Transactions on Power Electronics*, vol. 24, no. 8, pp. 1859-1875, 2009.
- [28] L. Fan, *Control and dynamics in power systems and microgrids*. CRC Press, 2017.
- [29] S. Anand, S. K. Gundlapalli, and B. G. Fernandes, "Transformer-less grid feeding current source inverter for solar photovoltaic system," *IEEE Transactions on Industrial Electronics*, vol. 61, no. 10, pp. 5334-5344, 2014.
- [30] S. Jain and V. Agarwal, "A single-stage grid connected inverter topology for solar PV systems with maximum power point tracking," *IEEE transactions on power electronics*, vol. 22, no. 5, pp. 1928-1940, 2007.
- [31] Y. Sun et al., "The Impact of PLL Dynamics on the Low Inertia Power Grid: A Case Study of Bonaire Island Power System," *Energies*, vol. 12, no. 7, 2019.
- [32] A. A. Nazib, D. G. Holmes, and B. P. McGrath, "Self-Synchronising Stationary Frame Inverter-Current-Feedback Control for LCL Grid-Connected Inverters," *IEEE Journal of Emerging and Selected Topics in Power Electronics*, 2021.
- [33] J. Rocabert, A. Luna, F. Blaabjerg, and P. Rodríguez, "Control of Power Converters in AC Microgrids," *IEEE Transactions on Power Electronics*, vol. 27, no. 11, pp. 4734-4749, 2012.
- [34] R. H. Lasseter, Z. Chen, and D. Pattabiraman, "Grid-forming inverters: A critical asset for the power grid," *IEEE Journal of Emerging and Selected Topics in Power Electronics*, vol. 8, no. 2, pp. 925-935, 2019.

- 
- [35] F. Blaabjerg, R. Teodorescu, M. Liserre, and A. V. Timbus, "Overview of Control and Grid Synchronization for Distributed Power Generation Systems," *IEEE Transactions on Industrial Electronics*, vol. 53, no. 5, pp. 1398-1409, 2006.
- [36] K. De Brabandere, B. Bolsens, J. Van den Keybus, A. Woyte, J. Driesen, and R. Belmans, "A voltage and frequency droop control method for parallel inverters," *IEEE Transactions on power electronics*, vol. 22, no. 4, pp. 1107-1115, 2007.
- [37] H. Han, Y. Liu, Y. Sun, M. Su, and J. M. Guerrero, "An improved droop control strategy for reactive power sharing in islanded microgrid," *IEEE Transactions on Power Electronics*, vol. 30, no. 6, pp. 3133-3141, 2014.
- [38] Q.-C. Zhong, "Virtual Synchronous Machines: A unified interface for grid integration," *IEEE Power Electronics Magazine*, vol. 3, no. 4, pp. 18-27, 2016.
- [39] Q.-C. Zhong and G. Weiss, "Synchronverters: Inverters That Mimic Synchronous Generators," *IEEE Transactions on Industrial Electronics*, vol. 58, no. 4, pp. 1259-1267, 2011.
- [40] B. B. Johnson, S. V. Dhople, A. O. Hamadeh, and P. T. Krein, "Synchronization of parallel single-phase inverters with virtual oscillator control," *IEEE Transactions on Power Electronics*, vol. 29, no. 11, pp. 6124-6138, 2013.
- [41] C. Maara, "Microgrids: Technologies and Global Markets," BCC Research 2018.
- [42] H. Xie, S. Zheng, and M. Ni, "Microgrid Development in China: A method for renewable energy and energy storage capacity configuration in a megawatt-level isolated microgrid," *IEEE Electrification Magazine*, vol. 5, no. 2, pp. 28-35, 2017.
- [43] D. E. Olivares et al., "Trends in microgrid control," *IEEE Transactions on smart grid*, vol. 5, no. 4, pp. 1905-1919, 2014.
- [44] B. Chen, J. Wang, X. Lu, C. Chen, and S. Zhao, "Networked Microgrids for Grid Resilience, Robustness, and Efficiency: A Review," *IEEE Transactions on Smart Grid*, vol. 12, no. 1, pp. 18-32, 2021.
- [45] J. M. Guerrero, J. C. Vasquez, J. Matas, L. G. De Vicuña, and M. Castilla, "Hierarchical control of droop-controlled AC and DC microgrids—A general approach toward standardization," *IEEE Transactions on industrial electronics*, vol. 58, no. 1, pp. 158-172, 2010.

- 
- [46] F. Shahnia, R. P. Chandrasena, S. Rajakaruna, and A. Ghosh, "Primary control level of parallel distributed energy resources converters in system of multiple interconnected autonomous microgrids within self-healing networks," *IET Generation, Transmission & Distribution*, vol. 8, no. 2, pp. 203-222, 2014.
- [47] N. L. Diaz, A. C. Luna, J. C. Vasquez, and J. M. Guerrero, "Centralized control architecture for coordination of distributed renewable generation and energy storage in islanded AC microgrids," *IEEE Transactions on Power Electronics*, vol. 32, no. 7, pp. 5202-5213, 2016.
- [48] K. T. Tan, X. Peng, P. L. So, Y. C. Chu, and M. Z. Chen, "Centralized control for parallel operation of distributed generation inverters in microgrids," *IEEE Transactions on Smart Grid*, vol. 3, no. 4, pp. 1977-1987, 2012.
- [49] H. Dagdougui and R. Sacile, "Decentralized control of the power flows in a network of smart microgrids modeled as a team of cooperative agents," *IEEE Transactions on Control Systems Technology*, vol. 22, no. 2, pp. 510-519, 2013.
- [50] A. Khorsandi, M. Ashourloo, and H. Mokhtari, "A decentralized control method for a low-voltage DC microgrid," *IEEE Transactions on Energy Conversion*, vol. 29, no. 4, pp. 793-801, 2014.
- [51] Q. Li, F. Chen, M. Chen, J. M. Guerrero, and D. Abbott, "Agent-based decentralized control method for islanded microgrids," *IEEE Transactions on Smart Grid*, vol. 7, no. 2, pp. 637-649, 2015.
- [52] H. Han, X. Hou, J. Yang, J. Wu, M. Su, and J. M. Guerrero, "Review of Power Sharing Control Strategies for Islanding Operation of AC Microgrids," *IEEE Transactions on Smart Grid*, vol. 7, no. 1, pp. 200-215, 2016.
- [53] L. Ding, Q.-L. Han, and E. Sindi, "Distributed cooperative optimal control of DC microgrids with communication delays," *IEEE Transactions on Industrial Informatics*, vol. 14, no. 9, pp. 3924-3935, 2018.
- [54] C. Dong et al., "Time-delay stability analysis for hybrid energy storage system with hierarchical control in DC microgrids," *IEEE Transactions on Smart Grid*, vol. 9, no. 6, pp. 6633-6645, 2017.
- [55] X. Meng, J. Liu, and Z. Liu, "A Generalized Droop Control for Grid-Supporting Inverter Based on Comparison Between Traditional Droop Control and Virtual

- 
- Synchronous Generator Control," IEEE Transactions on Power Electronics, vol. 34, no. 6, pp. 5416-5438, 2019.
- [56] S. Wang, Z. Liu, J. Liu, D. Boroyevich, and R. Burgos, "Small-Signal Modeling and Stability Prediction of Parallel Droop-Controlled Inverters Based on Terminal Characteristics of Individual Inverters," IEEE Transactions on Power Electronics, vol. 35, no. 1, pp. 1045-1063, 2020.
- [57] J. Liu, Y. Miura, and T. Ise, "Comparison of Dynamic Characteristics Between Virtual Synchronous Generator and Droop Control in Inverter-Based Distributed Generators," IEEE Transactions on Power Electronics, vol. 31, no. 5, pp. 3600-3611, 2016.
- [58] L. Guo, S. Zhang, X. Li, Y. W. Li, C. Wang, and Y. Feng, "Stability Analysis and Damping Enhancement Based on Frequency-Dependent Virtual Impedance for DC Microgrids," IEEE Journal of Emerging and Selected Topics in Power Electronics, vol. 5, no. 1, pp. 338-350, 2017.
- [59] J. He and Y. W. Li, "Analysis, design, and implementation of virtual impedance for power electronics interfaced distributed generation," IEEE Transactions on Industry Applications, vol. 47, no. 6, pp. 2525-2538, 2011.
- [60] X. Wang, Y. W. Li, F. Blaabjerg, and P. C. Loh, "Virtual-impedance-based control for voltage-source and current-source converters," IEEE Transactions on Power Electronics, vol. 30, no. 12, pp. 7019-7037, 2014.
- [61] Q. Shafiee, J. M. Guerrero, and J. C. Vasquez, "Distributed secondary control for islanded microgrids—A novel approach," IEEE Transactions on power electronics, vol. 29, no. 2, pp. 1018-1031, 2013.
- [62] Y. Du, X. Lu, J. Wang, and S. Lukic, "Distributed secondary control strategy for microgrid operation with dynamic boundaries," IEEE Transactions on Smart Grid, vol. 10, no. 5, pp. 5269-5282, 2018.
- [63] S. Moayedi and A. Davoudi, "Distributed tertiary control of DC microgrid clusters," IEEE Transactions on Power Electronics, vol. 31, no. 2, pp. 1717-1733, 2015.
- [64] AEMO, "Black System South Australia 28 September 2016," 2017.



- 
- [65] R. Yan, N. A. Masood, T. K. Saha, F. Bai, and H. Gu, "The Anatomy of the 2016 South Australia Blackout: A Catastrophic Event in a High Renewable Network," *IEEE Transactions on Power Systems*, pp. 1-1, 2018.
- [66] E. B. Ssekulima, M. S. El Moursi, A. Al Hinai, and M. B. Anwar, "Wind speed and solar irradiance forecasting techniques for enhanced renewable energy integration with the grid: a review," *IET Renewable Power Generation*, vol. 10, no. 7, pp. 885-989, 2016.
- [67] Y. Wang, V. Silva, and M. Lopez-Botet-Zulueta, "Impact of high penetration of variable renewable generation on frequency dynamics in the continental Europe interconnected system," *IET Renewable Power Generation*, vol. 10, no. 1, pp. 10-16, 2016.
- [68] A. E. M. Operator, "International Review of Frequency Control Adaptation," 2016, Available: [https://www.aemo.com.au/-/media/Files/Electricity/NEM/Security\\_and\\_Reliability/Reports/2016/FPSS---International-Review-of-Frequency-Control.pdf](https://www.aemo.com.au/-/media/Files/Electricity/NEM/Security_and_Reliability/Reports/2016/FPSS---International-Review-of-Frequency-Control.pdf).
- [69] A. E. M. Operator, "Integrated Final Report SA Black System 28 September 2016," Australia Energy Market Operator 2017, Available: [http://www.aemo.com.au/-/media/Files/Electricity/NEM/Market\\_Notices\\_and\\_Events/Power\\_System\\_Incident\\_Reports/2017/Integrated-Final-Report-SA-Black-System-28-September-2016.pdf](http://www.aemo.com.au/-/media/Files/Electricity/NEM/Market_Notices_and_Events/Power_System_Incident_Reports/2017/Integrated-Final-Report-SA-Black-System-28-September-2016.pdf).
- [70] S. Eftekharnjad, V. Vittal, G. T. Heydt, B. Keel, and J. Loehr, "Small Signal Stability Assessment of Power Systems With Increased Penetration of Photovoltaic Generation: A Case Study," *IEEE Transactions on Sustainable Energy*, vol. 4, no. 4, pp. 960-967, 2013.
- [71] G. Ramtharan, N. Jenkins, and J. B. Ekanayake, "Frequency support from doubly fed induction generator wind turbines," *IET Renewable Power Generation*, vol. 1, no. 1, 2007.
- [72] S. Wang, J. Hu, X. Yuan, and L. Sun, "On inertial dynamics of virtual-synchronous-controlled DFIG-based wind turbines," *IEEE Transactions on Energy Conversion*, vol. 30, no. 4, pp. 1691-1702, 2015.
- [73] Y. Fu, Y. Wang, and X. Zhang, "Integrated wind turbine controller with virtual inertia and primary frequency responses for grid dynamic frequency support," *IET Renewable Power Generation*, vol. 11, no. 8, pp. 1129-1137, 2017.

- 
- [74] F. M. Hughes, O. Anaya-Lara, N. Jenkins, and G. Strbac, "Control of DFIG-Based Wind Generation for Power Network Support," *IEEE Transactions on Power Systems*, vol. 20, no. 4, pp. 1958-1966, 2005.
- [75] J. Morren, S. W. H. de Haan, W. L. Kling, and J. A. Ferreira, "Wind Turbines Emulating Inertia and Supporting Primary Frequency Control," *IEEE Transactions on Power Systems*, vol. 21, no. 1, pp. 433-434, 2006.
- [76] Y. Li, Z. Xu, and K. P. Wong, "Advanced control strategies of PMSG-based wind turbines for system inertia support," *IEEE Transactions on Power Systems*, vol. 32, no. 4, pp. 3027-3037, 2017.
- [77] D. Jovcic, L. Lamont, and L. Xu, "VSC transmission model for analytical studies," in *Power Engineering Society General Meeting, 2003, IEEE, 2003*, vol. 3, pp. 1737-1742: IEEE.
- [78] S. Wang, J. Hu, and X. Yuan, "Virtual Synchronous Control for Grid-Connected DFIG-Based Wind Turbines," *IEEE Journal of Emerging and Selected Topics in Power Electronics*, vol. 3, no. 4, pp. 932-944, 2015.
- [79] L. Miao, J. Wen, H. Xie, C. Yue, and W.-J. Lee, "Coordinated control strategy of wind turbine generator and energy storage equipment for frequency support," *IEEE Transactions on Industry Applications*, vol. 51, no. 4, pp. 2732-2742, 2015.
- [80] F. Díaz-González, M. Hau, A. Sumper, and O. Gomis-Bellmunt, "Coordinated operation of wind turbines and flywheel storage for primary frequency control support," *International Journal of Electrical Power & Energy Systems*, vol. 68, pp. 313-326, 2015.
- [81] Y. Ma, W. Cao, L. Yang, F. F. Wang, and L. M. Tolbert, "Virtual Synchronous Generator Control of Full Converter Wind Turbines With Short-Term Energy Storage," *IEEE Transactions on Industrial Electronics*, vol. 64, no. 11, pp. 8821-8831, 2017.
- [82] J. Fang, X. Li, Y. Tang, and H. Li, "Power management of virtual synchronous generators through using hybrid energy storage systems," in *Applied Power Electronics Conference and Exposition (APEC), 2018 IEEE, 2018*, pp. 1407-1411: IEEE.
- [83] J. Fang, H. Li, Y. Tang, and F. Blaabjerg, "Distributed Power System Virtual Inertia Implemented by Grid-Connected Power Converters," *IEEE Transactions on Power Electronics*, 2017.

- 
- [84] L. Wook-Jin and S. Seung-Ki, "DC-Link Voltage Stabilization for Reduced DC-Link Capacitor Inverter," *IEEE Transactions on Industry Applications*, vol. 50, no. 1, pp. 404-414, 2014.
- [85] Y. Jun, L. Hui, L. Yong, and C. Zhe, "An Improved Control Strategy of Limiting the DC-Link Voltage Fluctuation for a Doubly Fed Induction Wind Generator," *IEEE Transactions on Power Electronics*, vol. 23, no. 3, pp. 1205-1213, 2008.
- [86] P. Kundur, N. J. Balu, and M. G. Lauby, *Power system stability and control*. McGraw-hill New York, 1994.
- [87] J. Machowski, J. Bialek, J. R. Bumby, and J. Bumby, *Power system dynamics and stability*. John Wiley & Sons, 1997.
- [88] P. M. Anderson and M. Mirheydar, "A Low-Order System Frequency Response Model," *IEEE Transactions on Power Systems*, vol. 5, no. 3, p. 10, 1990.
- [89] A. Semerow, T. Wolf, S. Wellhöfer, and M. Luther, "Power system model order reduction based on dominant modes in modal analysis," in *Power & Energy Society General Meeting, 2017 IEEE*, 2017, pp. 1-5: IEEE.
- [90] N. R. Subcommittee, "Balancing and Frequency Control," Princeton2011, Available:  
<https://www.nerc.com/docs/oc/rs/NERC%20Balancing%20and%20Frequency%20Control%20040520111.pdf>.
- [91] S. El Itani, U. D. Annakkage, and G. Joos, "Short-term frequency support utilizing inertial response of DFIG wind turbines," in *Power and Energy Society General Meeting, 2011 IEEE*, 2011, pp. 1-8: IEEE.
- [92] *Transmission Code of Singapore*, 2014.
- [93] G. Raman, J. C.-H. Peng, and H. H. Zeineldin, "Optimal Damping Recovery Scheme for Droop-Controlled Inverter-Based Microgrids," *IEEE Transactions on Smart Grid*, vol. 11, no. 4, pp. 2805-2815, 2020.
- [94] B. M. Eid, N. A. Rahim, J. Selvaraj, and A. H. El Khateb, "Control Methods and Objectives for Electronically Coupled Distributed Energy Resources in Microgrids: A Review," *IEEE Systems Journal*, vol. 10, no. 2, pp. 446-458, 2016.
- [95] J. M. Guerrero, M. Chandorkar, T.-L. Lee, and P. C. Loh, "Advanced Control Architectures for Intelligent Microgrids—Part I: Decentralized and Hierarchical

- 
- Control," IEEE Transactions on Industrial Electronics, vol. 60, no. 4, pp. 1254-1262, 2013.
- [96] Y. Geng, L. Zhu, X. Song, K. Wang, and X. Li, "A Modified Droop Control for Grid-Connected Inverters With Improved Stability in the Fluctuation of Grid Frequency and Voltage Magnitude," IEEE Access, vol. 7, pp. 75658-75669, 2019.
- [97] N. Pogaku, M. Prodanovic, and T. C. Green, "Modeling, Analysis and Testing of Autonomous Operation of an Inverter-Based Microgrid," IEEE Transactions on Power Electronics, vol. 22, no. 2, pp. 613-625, 2007.
- [98] A. Bolzoni, G. M. Foglia, L. Frosio, M. F. Iacchetti, and R. Perini, "Impact of Line and Control Parameters on Droop Stability in Inverters for Distributed Generation," IEEE Transactions on Smart Grid, vol. 9, no. 6, pp. 6656-6665, 2018.
- [99] K. Yu, Q. Ai, S. Wang, J. Ni, and T. Lv, "Analysis and Optimization of Droop Controller for Microgrid System Based on Small-Signal Dynamic Model," IEEE Transactions on Smart Grid, pp. 1-11, 2015.
- [100] Y. Pan, L. Chen, X. Lu, J. Wang, F. Liu, and S. Mei, "Stability Region of Droop-Controlled Distributed Generation in Autonomous Microgrids," IEEE Transactions on Smart Grid, vol. 10, no. 2, pp. 2288-2300, 2019.
- [101] J. Chen and J. Chen, "Stability Analysis and Parameters Optimization of Islanded Microgrid With Both Ideal and Dynamic Constant Power Loads," IEEE Transactions on Industrial Electronics, vol. 65, no. 4, pp. 3263-3274, 2018.
- [102] N. Bottrell, M. Prodanovic, and T. C. Green, "Dynamic Stability of a Microgrid With an Active Load," IEEE Transactions on Power Electronics, vol. 28, no. 11, pp. 5107-5119, 2013.
- [103] M. A. Hassan and M. A. Abido, "Optimal Design of Microgrids in Autonomous and Grid-Connected Modes Using Particle Swarm Optimization," IEEE Transactions on Power Electronics, vol. 26, no. 3, pp. 755-769, 2011.
- [104] M. B. Delghavi and A. Yazdani, "An Adaptive Feedforward Compensation for Stability Enhancement in Droop-Controlled Inverter-Based Microgrids," IEEE Transactions on Power Delivery, vol. 26, no. 3, pp. 1764-1773, 2011.
- [105] Y. Mohamed and E. F. El-Saadany, "Adaptive Decentralized Droop Controller to Preserve Power Sharing Stability of Paralleled Inverters in Distributed Generation

- 
- Microgrids," IEEE Transactions on Power Electronics, vol. 23, no. 6, pp. 2806-2816, 2008.
- [106] E. S. N. Raju P and T. Jain, "A Two-Level Hierarchical Controller to Enhance Stability and Dynamic Performance of Islanded Inverter-Based Microgrids With Static and Dynamic Loads," IEEE Transactions on Industrial Informatics, vol. 15, no. 5, pp. 2786-2797, 2019.
- [107] B. Keyvani-Boroujeni, G. Shahgholian, and B. Fani, "A Distributed Secondary Control Approach for Inverter-Dominated Microgrids with Application to Avoiding Bifurcation-Triggered Instabilities," IEEE Journal of Emerging and Selected Topics in Power Electronics, pp. 1-1, 2020.
- [108] F. P. Demello and C. Concordia, "Concepts of synchronous machine stability as affected by excitation control," IEEE Transactions on power apparatus and systems, vol. 88, no. 4, pp. 316-329, 1969.
- [109] E. Larsen and D. Swann, "Applying power system stabilizers part I: general concepts," IEEE Transactions on Power Apparatus and systems, no. 6, pp. 3017-3024, 1981.
- [110] D. Lam and H. Yee, "A study of frequency responses of generator electrical torques for power system stabilizer design," IEEE transactions on power systems, vol. 13, no. 3, pp. 1136-1142, 1998.
- [111] W. Du, W. Dong, Y. Wang, and H. Wang, "A Method to Design Power System Stabilizers in a Multi-Machine Power System Based on Single-Machine Infinite-Bus System Model," IEEE Transactions on Power Systems, 2020.
- [112] G. Gurrala and I. Sen, "Power system stabilizers design for interconnected power systems," IEEE Transactions on power systems, vol. 25, no. 2, pp. 1042-1051, 2010.
- [113] A. Kumar, "Power system stabilizers design for multimachine power systems using local measurements," IEEE Transactions on Power Systems, vol. 31, no. 3, pp. 2163-2171, 2015.
- [114] A. Kahrobaeian and Y. A.-R. I. Mohamed, "Suppression of interaction dynamics in DG converter-based microgrids via robust system-oriented control approach," IEEE Transactions on Smart Grid, vol. 3, no. 4, pp. 1800-1811, 2012.

- 
- [115] B. Wen, R. Burgos, D. Boroyevich, P. Mattavelli, and Z. Shen, "AC Stability Analysis and dq Frame Impedance Specifications in Power-Electronics-Based Distributed Power Systems," *IEEE Journal of Emerging and Selected Topics in Power Electronics*, vol. 5, no. 4, pp. 1455-1465, 2017.
- [116] A. Firdaus and S. Mishra, "Mitigation of Power and Frequency Instability to Improve Load Sharing Among Distributed Inverters in Microgrid Systems," *IEEE Systems Journal*, vol. 14, no. 1, pp. 1024-1033, 2020.
- [117] N. Bottrell, "Small-signal analysis of active loads and large-signal analysis of faults in inverter interfaced microgrid applications," Imperial College London, 2013.
- [118] D. K. Dheer, V. A.S, O. V. Kulkarni, and S. Doolla, "Improvement of Stability Margin of Droop-Based Islanded Microgrids by Cascading of Lead Compensators," *IEEE Transactions on Industry Applications*, vol. 55, no. 3, pp. 3241-3251, 2019.
- [119] R. Majumder, B. Chaudhuri, A. Ghosh, R. Majumder, G. Ledwich, and F. Zare, "Improvement of Stability and Load Sharing in an Autonomous Microgrid Using Supplementary Droop Control Loop," *IEEE Transactions on Power Systems*, vol. 25, no. 2, pp. 796-808, 2010.
- [120] L. M. Antonio and C. A. C. Coello, "Coevolutionary multiobjective evolutionary algorithms: Survey of the state-of-the-art," *IEEE Transactions on Evolutionary Computation*, vol. 22, no. 6, pp. 851-865, 2017.
- [121] I. Nikolakakos, I. Al-Zyoud, H. Zeineldin, M. El-Moursi, and A. Al-Hinai, "Enhancement of islanded droop-controlled microgrid performance via power filter design," in *2014 IEEE PES General Meeting| Conference & Exposition, 2014*, pp. 1-5: IEEE.
- [122] R. An, J. Liu, T. Wu, S. Wang, and B. Liu, "Analysis and design of cutoff frequency for power calculation low-pass filters in droop control," in *2017 IEEE 3rd International Future Energy Electronics Conference and ECCE Asia (IFEEC 2017-ECCE Asia), 2017*, pp. 1596-1600: IEEE.
- [123] M. Tarokh, "Measures for controllability and eigenvalue mobility," in *29th IEEE Conference on Decision and Control, 1990*, pp. 1143-1148: IEEE.
- [124] J. H. Wilkinson, *The algebraic eigenvalue problem*. Clarendon press Oxford, 1965.

- 
- [125] F. Dussaud, "An application of modal analysis in electric power systems to study inter-area oscillations," ed, 2015.
- [126] C.-T. Chen and B. Shafai, *Linear system theory and design*. Oxford university press New York, 1999.
- [127] L. Zadeh and C. Desoer, *Linear system theory: the state space approach*. Courier Dover Publications, 2008.
- [128] B. Sarlioglu and C. T. Morris, "More Electric Aircraft: Review, Challenges, and Opportunities for Commercial Transport Aircraft," *IEEE Transactions on Transportation Electrification*, vol. 1, no. 1, pp. 54-64, 2015.
- [129] Y. Wang, S. Nuzzo, H. Zhang, W. Zhao, C. Gerada, and M. Galea, "Challenges and Opportunities for Wound Field Synchronous Generators in Future More Electric Aircraft," *IEEE Transactions on Transportation Electrification*, vol. 6, no. 4, pp. 1466-1477, 2020.
- [130] L. Dorn-Gomba, J. Ramoul, J. Reimers, and A. Emadi, "Power Electronic Converters in Electric Aircraft: Current Status, Challenges, and Emerging Technologies," *IEEE Transactions on Transportation Electrification*, vol. 6, no. 4, pp. 1648-1664, 2020.
- [131] A. Emadi, B. Fahimi, and M. Ehsani, "On the concept of negative impedance instability in the more electric aircraft power systems with constant power loads," *SAE transactions*, pp. 689-699, 1999.
- [132] P. Wheeler and S. Bozhko, "The More Electric Aircraft: Technology and challenges," *IEEE Electrification Magazine*, vol. 2, no. 4, pp. 6-12, 2014.
- [133] L. Benadero, R. Cristiano, D. J. Pagano, and E. Ponce, "Nonlinear Analysis of Interconnected Power Converters: A Case Study," *IEEE Journal on Emerging and Selected Topics in Circuits and Systems*, vol. 5, no. 3, pp. 326-335, 2015.
- [134] M. Su, Z. Liu, Y. Sun, H. Han, and X. Hou, "Stability Analysis and Stabilization Methods of DC Microgrid With Multiple Parallel-Connected DC-DC Converters Loaded by CPLs," *IEEE Transactions on Smart Grid*, vol. 9, no. 1, pp. 132-142, 2018.
- [135] N. Vafamand, M. H. Khooban, T. Dragicevic, and F. Blaabjerg, "Networked Fuzzy Predictive Control of Power Buffers for Dynamic Stabilization of DC Microgrids," *IEEE Transactions on Industrial Electronics*, vol. 66, no. 2, pp. 1356-1362, 2019.

- 
- [136] Q. Xu, C. Zhang, C. Wen, and P. Wang, "A Novel Composite Nonlinear Controller for Stabilization of Constant Power Load in DC Microgrid," *IEEE Transactions on Smart Grid*, vol. 10, no. 1, pp. 752-761, 2019.
- [137] M. Cespedes and S. Jian, "Impedance Modeling and Analysis of Grid-Connected Voltage-Source Converters," *IEEE Transactions on Power Electronics*, vol. 29, no. 3, pp. 1254-1261, 2014.
- [138] M. Cespedes and J. Sun, "Adaptive Control of Grid-Connected Inverters Based on Online Grid Impedance Measurements," *IEEE Transactions on Sustainable Energy*, vol. 5, no. 2, pp. 516-523, 2014.
- [139] B. Wen, D. Boroyevich, R. Burgos, P. Mattavelli, and Z. Shen, "Analysis of D-Q Small-Signal Impedance of Grid-Tied Inverters," *IEEE Transactions on Power Electronics*, vol. 31, no. 1, pp. 675-687, 2016.
- [140] B. Wen, D. Boroyevich, R. Burgos, P. Mattavelli, and Z. Shen, "Small-Signal Stability Analysis of Three-Phase AC Systems in the Presence of Constant Power Loads Based on Measured d-q Frame Impedances," *IEEE Transactions on Power Electronics*, vol. 30, no. 10, pp. 5952-5963, 2015.
- [141] B. Wen, D. Boroyevich, P. Mattavelli, Z. Shen, and R. Burgos, "Experimental verification of the Generalized Nyquist stability criterion for balanced three-phase ac systems in the presence of constant power loads," in *2012 IEEE Energy Conversion Congress and Exposition (ECCE)*, 2012, pp. 3926-3933: IEEE.
- [142] M. Cespedes, L. Xing, and J. Sun, "Constant-Power Load System Stabilization by Passive Damping," *IEEE Transactions on Power Electronics*, vol. 26, no. 7, pp. 1832-1836, 2011.
- [143] X. Wang, F. Blaabjerg, M. Liserre, Z. Chen, J. He, and Y. Li, "An Active Damper for Stabilizing Power-Electronics-Based AC Systems," *IEEE Transactions on Power Electronics*, vol. 29, no. 7, pp. 3318-3329, 2014.
- [144] X. Zhang, D. M. Vilathgamuwa, K.-J. Tseng, B. S. Bhangu, and C. J. Gajanayake, "Power Buffer With Model Predictive Control for Stability of Vehicular Power Systems With Constant Power Loads," *IEEE Transactions on Power Electronics*, vol. 28, no. 12, pp. 5804-5812, 2013.



- 
- [145] Z. Ma, S. Saeidi, and R. Kennel, "FPGA Implementation of Model Predictive Control With Constant Switching Frequency for PMSM Drives," *IEEE Transactions on Industrial Informatics*, vol. 10, no. 4, pp. 2055-2063, 2014.
- [146] Z. Ma, X. Zhang, J. Huang, and B. Zhao, "Stability-Constraining-Dichotomy-Solution-Based Model Predictive Control to Improve the Stability of Power Conversion System in the MEA," *IEEE Transactions on Industrial Electronics*, vol. 66, no. 7, pp. 5696-5706, 2019.
- [147] J. He, C. Wen, and X. Zhang, "Composite-Bisection Predictive Control to Stabilize and Indirectly Regulate Downstream Load Inverters Cascaded with LC Input Filters in the SPS," *IEEE Journal of Emerging and Selected Topics in Power Electronics*, pp. 1-1, 2021.
- [148] M. F. Elmorshedy, W. Xu, F. F. M. El-Sousy, M. R. Islam, and A. A. Ahmed, "Recent Achievements in Model Predictive Control Techniques for Industrial Motor: A Comprehensive State-of-the-Art," *IEEE Access*, pp. 1-1, 2021.
- [149] A. A. A. Radwan and Y. A. R. I. Mohamed, "Analysis and Active-Impedance-Based Stabilization of Voltage-Source-Rectifier Loads in Grid-Connected and Isolated Microgrid Applications," *IEEE Transactions on Sustainable Energy*, vol. 4, no. 3, pp. 563-576, 2013.
- [150] A. A. A. Radwan and Y. A.-R. I. Mohamed, "Modeling, Analysis, and Stabilization of Converter-Fed AC Microgrids With High Penetration of Converter-Interfaced Loads," *IEEE Transactions on Smart Grid*, vol. 3, no. 3, pp. 1213-1225, 2012.
- [151] A. Suyapan, K. Areerak, S. Bozhko, S. S. Yeoh, and K. Areerak, "Adaptive Stabilization of a Permanent Magnet Synchronous Generator-Based DC Electrical Power System in More Electric Aircraft," *IEEE Transactions on Transportation Electrification*, pp. 1-1, 2021.
- [152] J. Liu, X. Lu, and J. Wang, "Resilience analysis of DC microgrids under denial of service threats," *IEEE Transactions on Power Systems*, vol. 34, no. 4, pp. 3199-3208, 2019.
- [153] M. J. A. R. M. Lee, T. Conway, "Analysis of the cyber attack on the Ukrainian power grid," *Electricity Information Sharing Annual Center* 2016.

- 
- [154] C. Deng, Y. Wang, C. Wen, Y. Xu, and P. Lin, "Distributed Resilient Control for Energy Storage Systems in Cyber-Physical Microgrids," *IEEE Transactions on Industrial Informatics*, vol. 17, no. 2, pp. 1331-1341, 2021.